THREE-DIMENSIONAL CLOUD VOLUME RECONSTRUCTION FROM THE MULTI-ANGLE IMAGING SPECTRORADIOMETER

BY

BYUNGSUK LEE

THESIS

Submitted in partial fulfillment of the requirements
for the degree of Master of Science in Atmospheric Sciences
in the Graduate College of the
University of Illinois at Urbana-Champaign, 2017

Urbana, Illinois

Adviser:

Professor Larry Di Girolamo

Abstract

Clouds continue to contribute the largest uncertainty to estimates and interpretations of the Earth's energy budget, and their representation in climate models has been recognized for decades as a dominant source of uncertainty in climate change projections. It has been suggested that understanding the 3-D structure of cloud would lead to better understanding of the Earth's radiative and latent fluxes. Indeed, knowing cloud 3-D geometry could lead to: 1) improving our understanding of cloud microphysical properties and processes, and 2) improving our knowledge of the radiative effects of cloud on the Earth's energy budget.

The Multi-angle Imaging SpectroRadiometer (MISR) is on board the Terra satellite, in its 17th year of operation as of 2017. MISR provides nine views of the same scene that allow scientists to visualize the 3-D structure of observed clouds to a certain extent. Taking advantage of such multi-angle characteristic, this project aims to reconstruct cloud volumes from MISR data.

The reconstruction domain is defined such that it takes into account the curvature of the Earth’s ellipsoidal surface. The input satellite images used are the Radiometric Camera-by-camera Cloud Masks at 1.1 km resolution developed by the MISR science team, and custom cloud masks at 275 m resolution developed from MISR RGB images in this project. Due to the time difference between each camera view angle, wind correction is performed on the input cloud masks. For the reconstruction method, “ray casting” algorithms that fully account for the instrument's geometric properties are developed. The reconstruction results are presented for three hand-picked MISR cloud scenes. Strengths and limitations of the reconstruction method are explored, and the outlook for the use of the reconstruction results are discussed.

Acknowledgements

This project has been largely guided by my advisor, Prof. Larry Di Girolamo. His scientific insight has been integral in setting the direction at each step throughout the project. His patience and encouragement have also been invaluable in my graduate study.

This project has been greatly aided by Dr. Guangyu Zhao. His technical expertise in satellite remote sensing and computer coding has been critical in moving this project forward.

This project has been funded by the National Aeronautics and Space Administration (NASA) through contract number NNX13AL96G, and by the Jet Propulsion Laboratory (JPL) through contract number 147871.

I give special thanks to my parents who, with their loving support, have helped me before and throughout my graduate study and therefore this thesis project. 나의 부모님께 감사드립니다.

Table of Contents

Chapter 1. Introduction

1.1. Cloud

In the Fifth Assessment Report by the Intergovernmental Panel on Climate Change (IPCC), in Chapter 2. Observations: Atmosphere and Surface, it is stated that "the radiation budget of the Earth is a central element of the climate system" (Hartmann et al., 2013). It goes on to explain that "on average, radiative processes warm the surface and cool the atmosphere, which is balanced by the hydrological cycle and sensible heating. Spatial and temporal energy imbalances due to radiation and latent heating produce the general circulation of the atmosphere and oceans." Moreover, "anthropogenic influence on climate occurs primarily through perturbations of the components of the Earth radiation budget."

In the same IPCC assessment report, in Chapter 7. Cloud and Aerosols, it is stated that "clouds and aerosols continue to contribute the largest uncertainty to estimates and interpretations of the Earth's changing energy budget" (Boucher et al., 2013). The report goes on to say that "by enhancing the planetary albedo, cloudy conditions exert a global and annual shortwave cloud radiative effect (SWCRE) of approximately –50 Wm^{-2} and, by contributing to the greenhouse effect, exert a mean longwave effect (LWCRE) of approximately +30 Wm^{-2} with a range of 10% or less between published satellite estimates (Loeb et al., 2009)." Hence, "owing to the large magnitudes of the SWCRE and LWCRE, clouds have the potential to cause significant climate feedback."

There is a whole book written about cloud's impact on the Earth's radiative transfer, titled "3-D Radiative Transfer in Cloudy Atmospheres", edited by A. Marshak and A. Davis in 2005. In the book, we learn that understanding 3-D structure of cloud would lead to better understanding of the Earth's radiative flux and latent flux. Figure 1.1 shows simple diagrams from the book depicting SWCRE and LWCRE. The radiative transfer in real world involves all directions within the 3-D space, and therefore the cloud structure, which affects this 3-D distribution of radiation, should be studied.

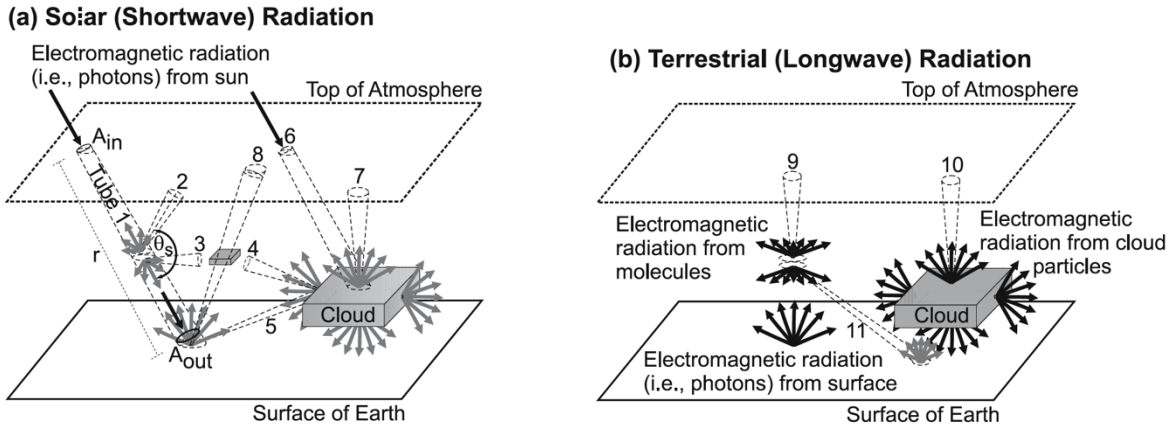

Figure 1.1. Cartoon illustration of radiances passing through the atmosphere of the Earth for (a) radiation originating from the sun (i.e., shortwave radiation) and (b) radiation originating from the Earth (i.e., longwave radiation). The dashed-line tubes represent radiances originating from a variety of sources and propagating through atmospheric molecules and cloud particles. The black arrows represent radiances from the source, while the gray arrows represent scattered radiation. The areas associated with tube 1 on the left side of (a) are used to provide an approximate definition for radiance. The angle θ_s in (a) is the scattering angle, while its associated azimuth angle ϕ_s, which represents the angle about the central axis of tube 1 at which the photon is scattered, is not drawn. (Clothiaux et al., 2005)

The book also contains an example study of how 3-D cloud structure results in different cloud transmittance in comparison to the plane parallel approximation (PPA) and the independent pixel approximation (IPA) commonly used in climate models. Our current climate models and satellite retrievals involving cloud use either PPA or IPA. Here, PPA means that the

radiative transfer is treated only one dimensionally (vertically), with the entire horizontal layer of the atmosphere sharing the same optical and microphysical properties. IPA means that the radiative transfer is treated again one dimensionally, while the horizontal layer of the atmosphere is divided into pixels that have distinct optical and microphysical properties from their neighboring pixels.

Figure 1.2 shows this extreme case study with a 3-D synthetic cloud, which is termed "popcorn cumulus cloud", consisting of cubic clouds in checkerboard configuration, in comparison to the plane parallel and the independent pixel approximations. The overall difference in the cloud transmittance among the three is vivid, and the two different approximations that the climate models use exhibit large difference. The point labeled 3D exhibits a value that is particular to the sun angle used, but for other sun angle values the point could lie above the IPA point or below the PPA point (Wiscombe, 2005).

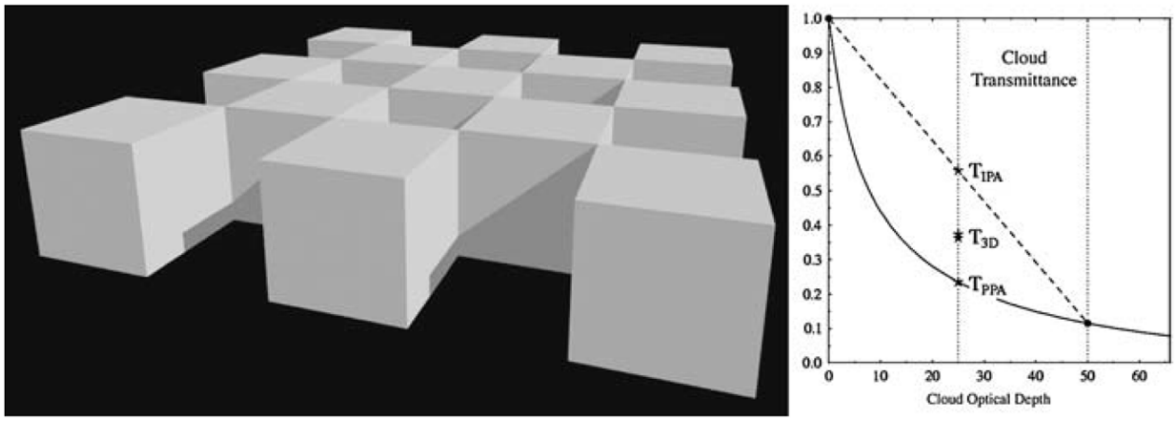

Figure 1.2. (Left) A regular array of cloud cubes, each with optical depth 50, asymmetry factor 0.85 and single-scattering albedo 0.999, embedded in a vacuum. Solar zenith angle is 50 degrees and cloud fraction is 50%. (Right) Transmittance versus optical depth: solid curve is for a 1D slab cloud and the three labeled points refer to the cloud array on the left, infinitely repeated. The point labeled PPA (Plane Parallel Approximation) simply uses the mean optical depth of the array (25) in 1D slab theory. The point labeled IPA (Independent Pixel Approximation) averages the transmissions of each column separately. The ordering shown, IPA above PPA, always holds because the curve of transmission versus optical depth is concave. (Adapted from a presentation by Bernhard Mayer at the 2004 International Radiation Symposium in Korea.) (Wiscombe, 2005)

The book also contains a study on the effect of the cloud geometry on the longwave radiative flux. The study is based on two simple assumptions, that 1) "the molecular atmosphere is plane-parallel and horizontally homogeneous", and that 2) "the cloud field for a given area is statistically homogeneous and isotropic" (Ellingson & Takara, 2005). The study compares the downwelling flux at the surface between the conventional plane parallel approximation with its absolute cloud fraction, A_c, and a simple 3-D cloud geometry which gives rise to the effective cloud fraction, A_{ce}. A simple diagram of this comparison is shown in Figure 1.3. The clouds are assumed to emit radiation like a black body, "a good assumption for cumulus clouds with optical thickness greater than 3 – a few hundred meters thick", (Ellingson & Takara, 2005) and to have a right-circle cylindrical shape with the aspect ratio, β, of the height to the radius.

Figure 1.4 shows $A_{ce} - A_c$ as a function of A_c for isothermal cylindrical clouds for different aspect ratios. The larger β leads to the larger cloud side area relative to the base area. The error in the plane parallel approximation which neglects cloud geometry can be estimated by combining this result of $A_{ce} - A_c$ with the longwave black cloud forcing which is calculated by multiplying the cloud fraction with the radiative flux by black clouds. If it is assumed that cumulus cloud depths are approximately the same as their widths, i.e. $\beta \approx 2$, the error peaks at $A_c \approx 0.35$, and hence $A_{ce} - A_c \approx 0.275$. According to a calculation of downward radiative forcing by black cloud in the book, "the overcast cloud forcing (CF) at the surface for cloud altitude 0.5 km is approximately 70 Wm^{-2}", (Ellingson & Takara, 2005) and this leads to the error $(A_{ce} - A_c) \cdot CF = 20\ Wm^{-2}$. In other words, neglecting cloud geometry could underestimate the downward flux at the surface by 20 Wm^{-2}. This leads to the general conclusion that, under

the same optical depth and other radiative properties, simple vertical stretching of the cloud, or taking the vertical length of clouds into account, could give rise to significant difference in the radiative flux in comparison to the plane parallel approximation.

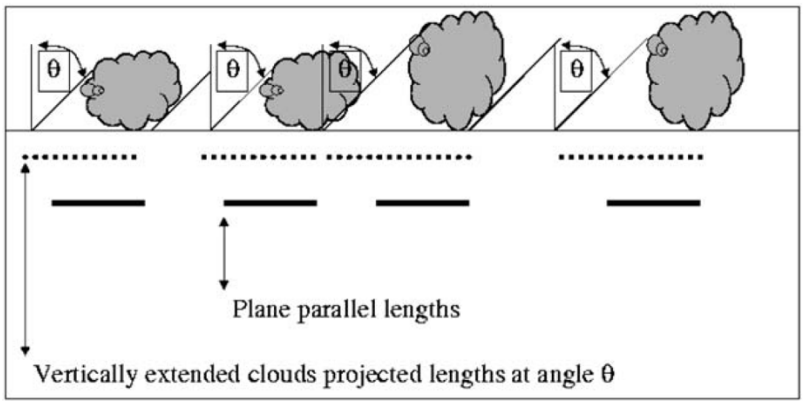

Figure 1.3. Two-dimensional view of an array of vertically extended clouds each with the same width. When viewed at angle θ, the clouds project as the dotted lines. When projected vertically downward, the clouds project as the solid horizontal lines (displaced here to coincide with the start of the dashed lines). The plane-parallel cloud assumption, the solid lines, underestimates cloud cover at all view angles greater than 0. (Ellingson & Takara, 2005)

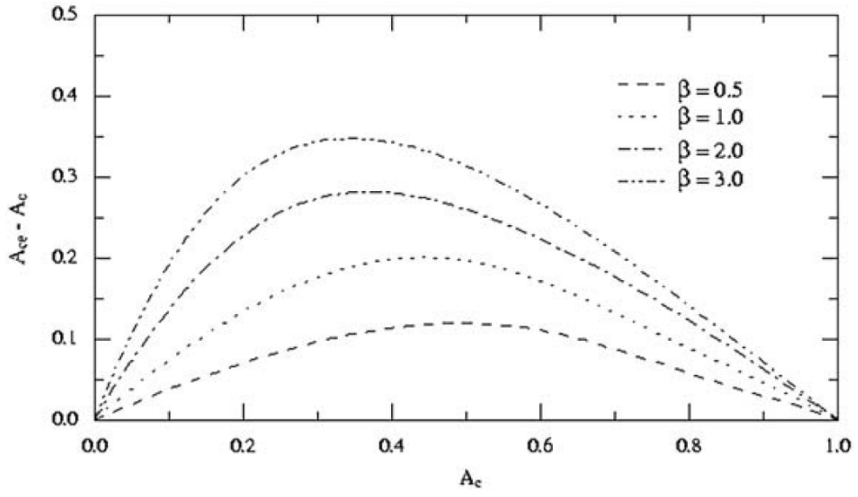

Figure 1.4. $A_{ce} - A_c$ as a function of A_c and β on A_{ce} for isothermal cylindrical clouds. (Ellingson & Takara, 2005)

A study by Hinkelman et al. (2007) showed the effect of 3-D cloud geometry on the radiation. The paper mentions that "both tilt and horizontal anisotropy (stretching) were found to significantly affect instantaneous domain-averaged solar fluxes, but tilt had more radiative impact than horizontal anisotropy" (Hinkelman et al., 2007). In short, for example, tilt leads to greater albedo. As seen in Figure 1.5, multiple cloud fields stochastically generated with different tilt values and matching liquid water content were examined using Monte Carlo radiative transfer calculations. The results in Figure 1.6 show the change in the transmission, reflection, absorption, and diffusion of the radiation at different tilt values, and at different solar zenith angles. This leads to the conclusion similar to that from the study by Ellingson & Takara, that with all other cloud properties held constant, the geometric structure of cloud yields difference in the radiative transfer of the atmosphere.

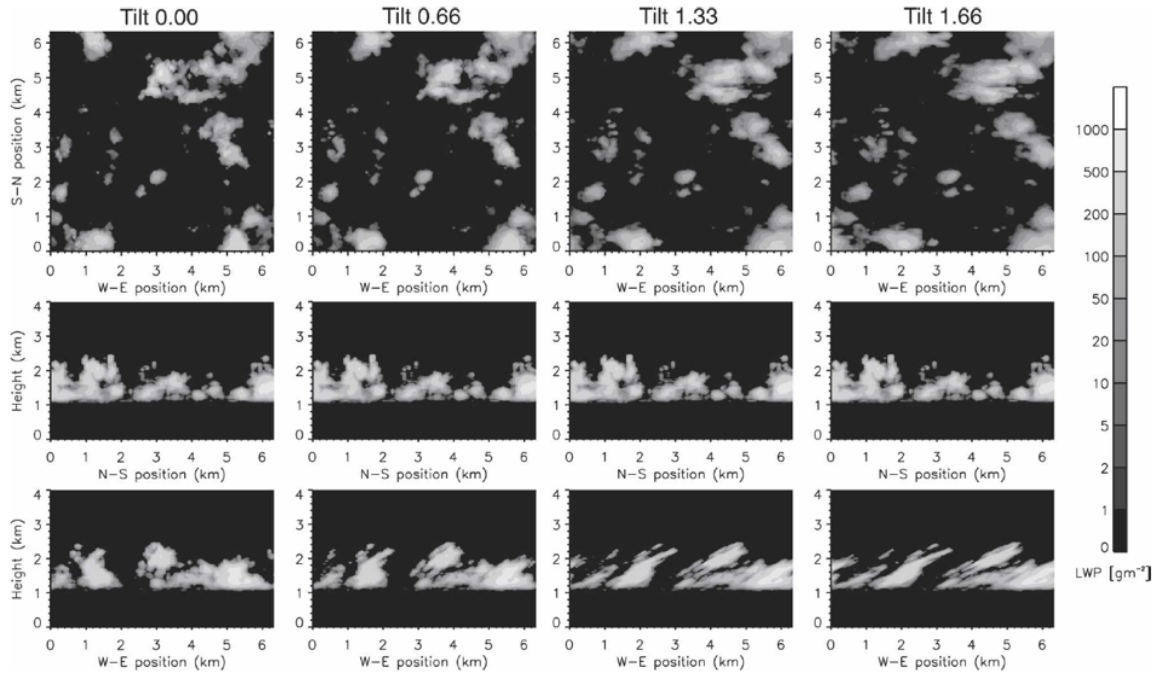

Figure 1.5. Example set of stochastic cloud fields with increasing vertical tilt. For each scene, integrated liquid water path is shown for views in three directions. (Hinkelman et al., 2007)

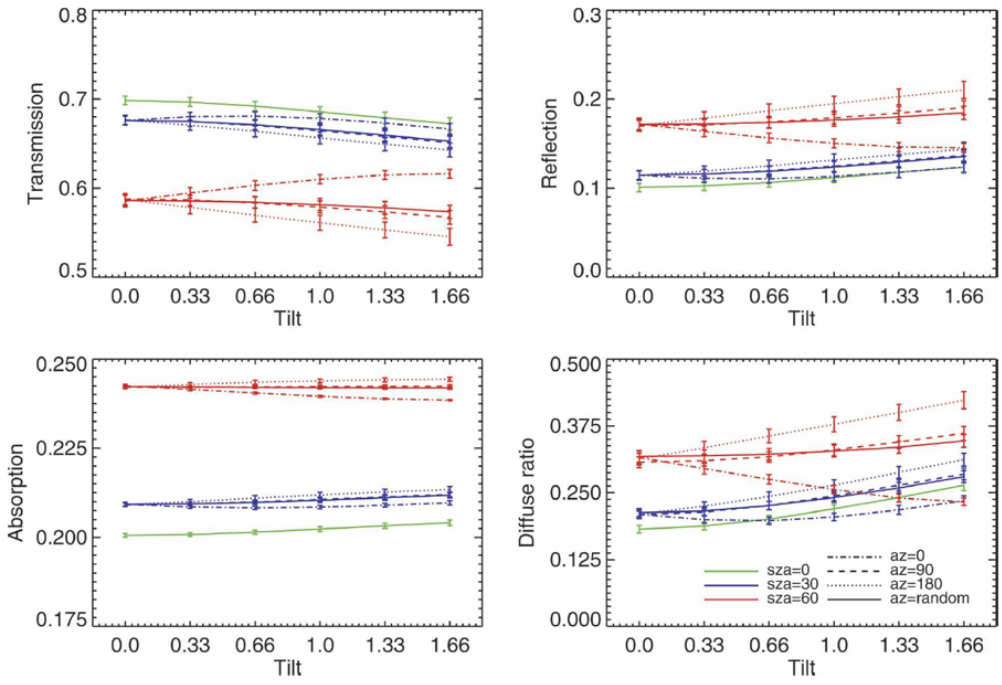

Figure 1.6. Domain-averaged (top left) transmission, (top right) reflection, (bottom left) absorption, and (bottom right) diffuse flux ratio for cloud scenes with increasing vertical tilt. Error bars indicate the standard error of the mean over the 20-scene ensembles. (Hinkelman et al., 2007)

The effect of 3-D cloud heterogeneity on remote sensing has been studied in many papers, one notable by Marshak et al. (2006). The study demonstrated through simulations that the passive retrieval of cloud droplet size, or effective radius (r_e), is heavily impacted by the 3-D radiative effects, especially through illumination and shadowing. Some of the key results are as follows.

- "With respect to the plane-parallel approximation, shadowing tends to increase r_e more than illumination decreases it; this results in an overall bias toward larger r_e".
- "Ignoring shadowing in 1-D retrievals results in substantial overestimation of r_e that often goes in pair with underestimation of τ. This effect is much more pronounced for broken Cu than for Sc clouds" (Marshak et al., 2006).

For example, Figure 1.7 shows how widespread the distribution of the retrieved effective radius could be, depending on its condition as shadowed or illuminated, compared to the true effective radius which is shown in the dashed line.

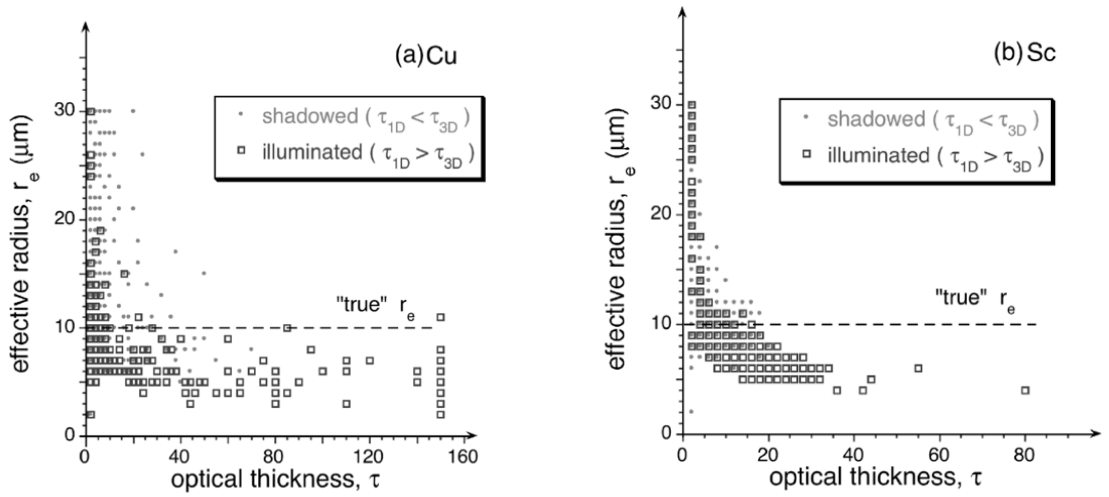

Figure 1.7. Correlation between retrieved τ and r_e for illuminated and shadowed areas. The horizontal dashed line indicates the true $r_e = 10\ \mu m$. Note that the maximal allowable retrieval value was set to 150 for optical thickness τ and to 30 μm for effective radius r_e. (a) Cumulus cloud field for an averaging scale $134 \times 134\ m$. (b) Stratocumulus cloud field for an averaging scale $110 \times 110\ m$. (Marshak et al., 2006)

Another study by Zhang et al. (2012) investigated the similar effects of 3-D cloud horizontal inhomogeneity on satellite retrievals of cloud droplet effective radius. The paper conducted a series of simulations involving large-eddy simulation (LES) cloud fields and radiative transfer models, to investigate the aforementioned effects at different spectral channels and satellite instrument resolutions. The study, based on the simulations of one of the current, Earth-observing satellite instruments, namely the Moderate Resolution Imaging Spectroradiometer (MODIS), concluded that the current satellite retrievals of effective radius based on reflectance at 2.1 μm and 3.7 μm may contain substantial errors due to 3-D radiative

transfer effects such as illumination and shadowing (Zhang et al., 2012). Figure 1.8 shows the results in the difference between the 3-D and 1-D radiative transfer retrievals for the LES resolution and the MODIS resolution at two different spectral channels.

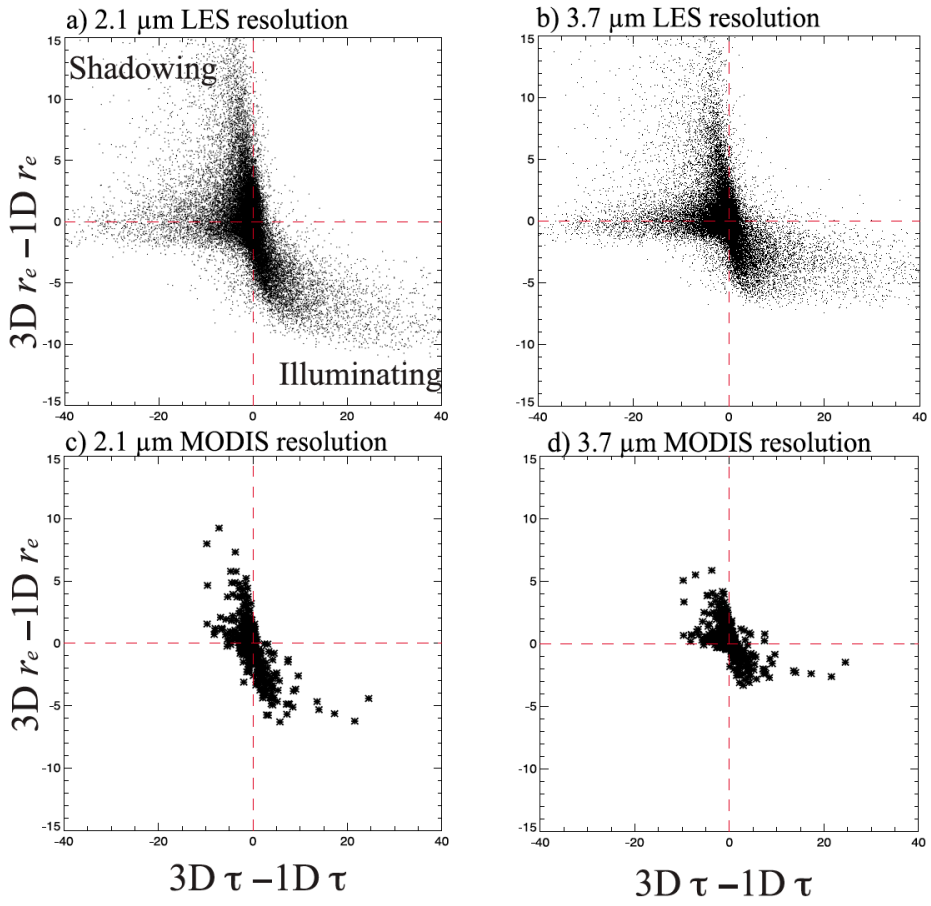

Figure 1.8. The difference between 3-D and 1-D τ retrieval versus the difference between (a) 3-D $r_{e,2.1}$ and 1-D $r_{e,2.1}$ at LES resolution, (b) 3-D $r_{e,3.7}$ and 1-D $r_{e,3.7}$ at LES resolution, (c) 3-D $r_{e,2.1}$ and 1-D $r_{e,2.1}$ at MODIS resolution, and (d) 3-D $r_{e,3.7}$ and 1-D $r_{e,3.7}$ at MODIS resolution. (Zhang et al., 2012)

Overall, studying 3-D cloud geometry has two implications: 1) it could lead to improving our understanding of cloud microphysical properties and processes by improving our remote sensing, and 2) it could help better understand the radiative effects of cloud on the Earth's radiation budget, which could then improve our climate models and therefore the climate

projection for the future. As Roger Davies, the Ph.D. advisor of Prof. Di Girolamo, put it in his dissertation in 1976, “these results indicate that a three-dimensional description of cloud geometry is a necessary prerequisite to the accurate determination of the emerging radiation field” (Davies, 1976). Therefore, it is important to characterize the 3-D structure of cloud, which has substantial effects on the Earth’s radiation budget, the key driver of weather and climate, and on our current remote sensing retrievals.

1.2. Past Studies on 3-D Cloud Structure from Observation Data

This section reviews up-to-date studies on 3-D cloud structure reconstruction from existing cloud observation data.

Ewald et al. (2015) studied methods for cloud geometry reconstruction from a ground-based scanning cloud radar. They used effective radar reflectivity values retrieved at multiple scan azimuth angles, and various methods of interpolations to a regular grid, to come up with the cloud volume. Quality measures with simulated cloud side images derived from a Monte Carlo radiative transfer model showed that the reconstruction results from simulated cloud fields overall exhibited positive bias (Ewald et al., 2015). They then applied the reconstruction methods to radar scans of convective cloud cases by a ground-based cloud scanning radar known as miraMACS, based in Munich, Germany. Figure 1.9 shows an example result of the reconstruction in color pictures.

Figure 1.9. (Left) Picture of a convective cloud taken during a miraMACS S-RHI scan (30 July 2013, 09:19 UTC. (Right) Reconstruction result for the scan from figure on the left. The picture was simulated using the MYSTIC Monte Carlo model (Mayer, 2009). Smaller clouds in the background are caused by the periodic boundary conditions which were used in the Monte Carlo simulation. (Ewald et al., 2015)

There are a few limitations associated with cloud volume reconstruction from ground based radar observations such as what this study shows. The cloud volume sometimes has radar reflectivity below the radar sensitivity threshold and therefore is left undetected; the radio waves experience attenuations; and the ground based observations are limited to the local area, with no meaningful measurements of cloud reflectivity values beyond a certain distance.

Another study by Zinner et al. (2006) showed the retrieval of 3-D stratocumulus structures from high-spatial-resolution radiance fields observed by the Compact Airborne Spectrographic Imager (CASI, 15 m resolution). First, “using a single wavelength, cloud optical thickness and via the adiabatic assumption,” “geometrical thickness as well as effective droplet size are retrieved for each pixel under the independent pixel and plane-parallel assumptions (IPA retrieval).” Then, “a point spread function is determined by calculating the spread of a

laser beam in a plane parallel cloud generated by horizontally averaging the derived cloud properties over the domain." Then, "an established iterative method, the Richardson-Lucy algorithm," is "used for the stepwise deconvolution of the observed radiance field to obtain several versions of the initial observation with increasing roughness. For each of these, the full cloud structure is retrieved using the described IPA procedure, including an adiabatic assumption of the vertical structure." Lastly, for each of these structures, "the radiance for the Sun and sensor geometry of the related observation is simulated" through a 3-D radiative transfer model, and criteria is "found to select the 3-D cloud structure best matching the CASI observation." In short, "a first guess cloud structure is determined from the observation and subsequently adjusted until the 3-D radiation field calculated for the cloud structure resembles the original CASI observation" (Zinner et al., 2006). The method was tested for an a priori defined cloud structure, by a visual comparison of the power spectrum between the iteration results from the synthetic observation featuring all characteristics of a real CASI instrument and the synthetic truth for the 3-D distribution of liquid water content and droplet radius. Figure 1.10 shows one example scene with the reconstruction result.

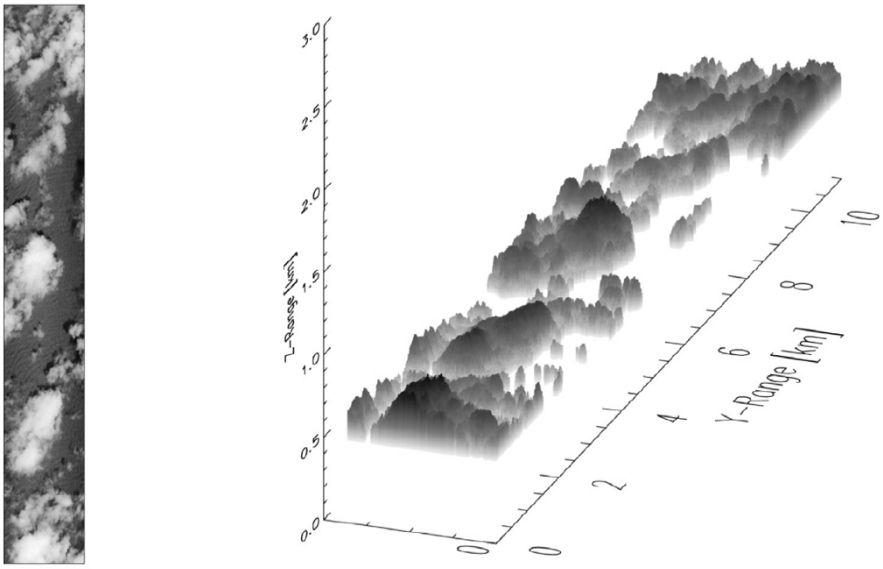

Figure 1.10. (Left) An example of CASI observations. Radiance at 753 nm, horizontal resolution 15 m x 15 m, scene size approximately 1.3 km x 10 km, boundary layer clouds over ocean, north of the Canary Islands, June/July 1997. The resolution is high enough to observe waves at the ocean surface. (Right) 3-D cloud structure for the same CASI case. The gray scale clarifies the adiabatic vertical structure of the clouds (increasing liquid water content and droplet radius with height are indicated by darkening gray) (Zinner et al., 2006)

While the study showed the reconstructions of the cloud geometry at the cloud tops, no geometry was reconstructed at the cloud bottoms. The results were thus rather ambiguous, and could greatly improve if the instrument had more view angles than just the nadir view, to retrieve information about the bottom of the observed clouds.

In a study by Barker et al. (2011), an algorithm for constructing 3-D distributions of clouds from "passive satellite imagery and collocated 2D nadir profiles of cloud properties inferred synergistically from lidar, cloud radar, and imager data" was developed and assessed (Barker et al., 2011). The algorithm used as input nadir active-passive retrieved cross-section (RXS) data, which are 2-D vertical cross-section profiles of cloud and aerosol properties over the satellite ground track retrieved from the combination of the active and passive remote sensors, and conventional passive imagery whose retrieval swath extends across the RXS. Within the

supposed cloud reconstruction domain, the vertical column of the non-RXS pixel was filled with the vertical column profile of an RXS pixel algorithmically chosen based on the similarity in the passive radiance retrievals and the Euclidean distance between the two pixels. The input data used for the assessment of the algorithm were derived from A-train satellite instruments, namely CloudSat, CALIPSO, and MODIS on board Aqua. Once the 3-D cloud profiles were reconstructed, 1-D radiative transfer models were used to calculate and compare the top-of-atmosphere (TOA) radiative fluxes with the radiance retrievals from Clouds and the Earth's Radiant Energy System (CERES). The differences between the modelled and the CERES measured reflected shortwave fluxes were within ±10 Wm^{-2} for around 35% of the several hundred domains constructed for eight orbits, and correspondingly, around 65% were within ±10 Wm^{-2} for outgoing longwave radiation (Barker et al., 2011).

Fielding et al. (2014) made use of retrievals from scanning cloud radars and downwelling zenith radiances from narrow field of view radiometers (2NFOV), instruments involved in the U.S. Department of Energy's Atmospheric Radiation Measurement program. First, they put the two different sets of observations onto a common 3-D grid. Then, within the common field of view of the zenith radiance and the radar retrievals, a group of vertical columns, dubbed "supercolumns", were selected, to which a series of algorithmic analyses were conducted in iterations to assign liquid water content (LWC), effective radius, and mean droplet number concentration, whose radiance and radar simulations best match the observations. Once the supercolumns were defined, a similar method as in the paper by Barker et al. (2011) was used to fill the non-supercolumns within the 3-D grid with the supercolumns, based on their radar reflectivity factors. For synthetic measurements from LES cloud fields, over the entire domain,

LWC and effective radius were retrieved with average error 0.05 to 0.08 gm^{-3} and around 2 μm, respectively, depending on the number of radiance channels used (Fielding et al., 2014).

In both studies discussed above, the 3-D cloud distribution outside the region of radiance retrievals were simply replaced with vertical columns inside the region. This means that the reconstructed 3-D cloud geometries of the observed clouds may be unrealistic and far from the actual truths.

In a study by Alexandrov et al. (2016), an airborne instrument named the Research Scanning Polarimeter was used to derive the geometric shape, dimensions, and height above the ground for the observed clouds. Using the cloud masks at multiple angular scans, their algorithm retrieved a 2-D cross-section of the observed cloud, along the flight track and the altitude, in the form of a geometric polygon whose boundaries were defined by the cloud mask boundaries. Then, the resultant cloud geometry was derived by constructing cloudy shapes with overlapping circles tangent to the polygon edges (Alexandrov et al., 2016). The error analyses were done by visual comparisons of the LES cloud fields and the reconstruction results from their synthetic observations. Figure 1.11 shows a reconstruction result from a real case study.

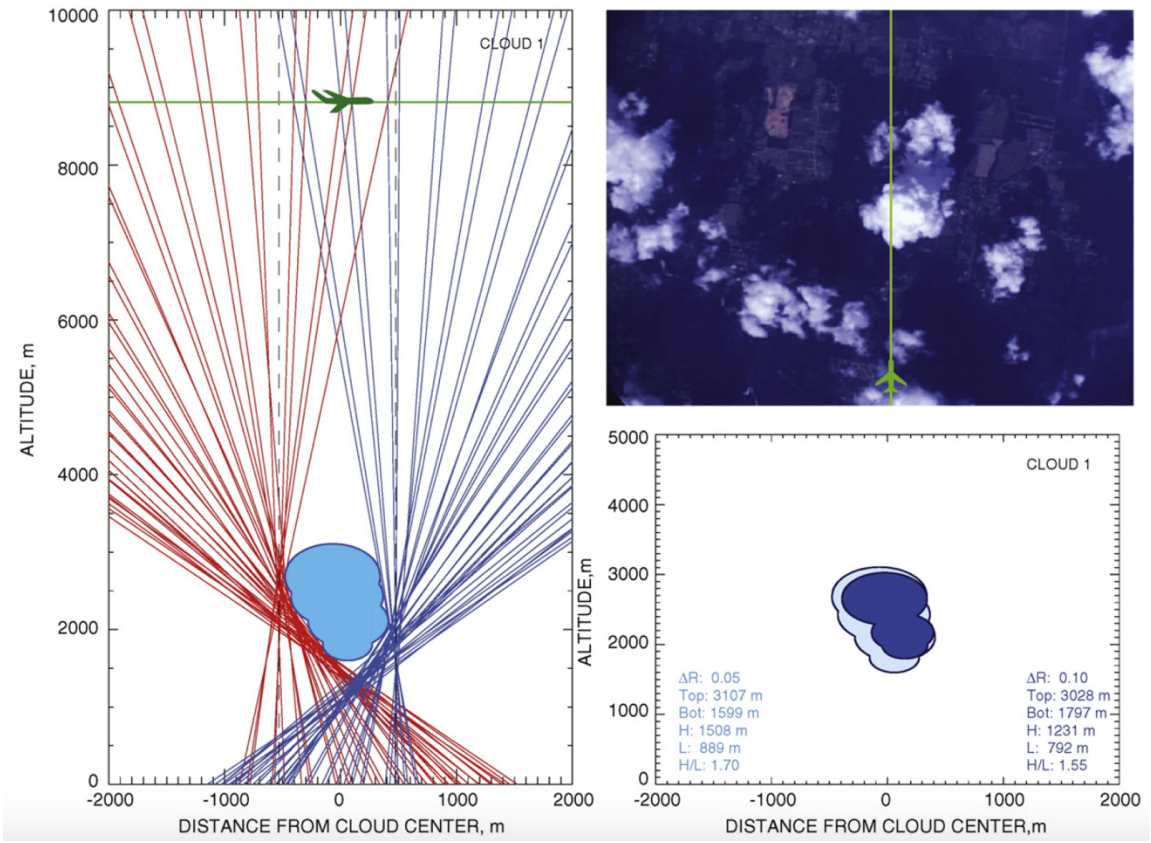

Figure 1.11. Analysis of the shape and dimensions of an example cloud. Left: Tangent lines derived from RSP cloud masks for bright (red) and shadowy (blue) sides of the cloud. Black dashed lines represent interpolated nadir views. The flight track is depicted by horizontal green line with airplane icon indicating the flight direction. The Sun was directly behind the aircraft. The cloud shape (light blue) corresponds to brightness threshold ΔR = 0.05. Top right: Image taken by down-looking cloud camera onboard UC-12 aircraft. Approximate flight track and flight direction are depicted by green line with airplane icon. The scale of this image at cloud top is approximately 6 by 4.5 km. Bottom-right: Cloud shapes and dimensions derived using ΔR = 0.05 (light blue) and ΔR = 0.1 (dark blue). (Alexandrov et al., 2016)

While the study showed multi-angle derivation of the cloud geometry that takes into account the vertical profiles and bottom of the observed clouds, the results were limited to 2-D cross-sections with no information in the cross-track distribution of the clouds. Besides, the limitations that this simple geometric reconstruction carries, such as the lack of firm definition of cloud boundaries or the usefulness of the technique only in the spatially isolated clouds, remain challenging issues, and will also be discussed later in this thesis.

1.3. The Multi-angle Imaging SpectroRadiometer

Bearing in mind the constraints discussed in the previous section, here we explore cloud volume reconstruction from the Multi-angle Imaging SpectroRadiometer (MISR). MISR is a passive remote sensor, on board the Terra satellite together with four other instruments. It was launched in December 1999, and is in the 17th year of operation as of 2017. MISR has global coverage in 233 orbits in the period of sixteen days, and the lasting operation period of 17 years and ongoing presents an opportunity to study 3-D distribution of clouds around the globe over a near-climatological period of time. More detailed information on MISR and its mission can be found in the MISR Experiment Overview (Diner, 1999). Figure 1.12 shows the diagram of MISR with its instrument specifications.

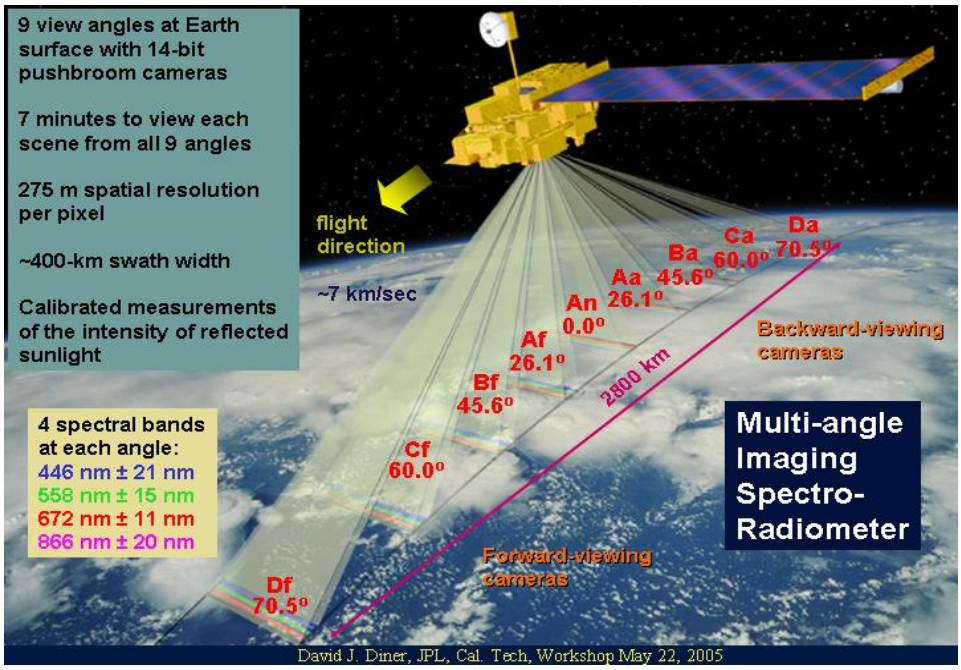

Figure 1.12. Diagram of MISR over the Earth, with basic instrument specifications such as view angles, spectral channels, resolution, and swath.

MISR views the Earth in a sun-synchronous orbit at nine widely spaced view angles, from the most forward view of DF to the nadir view of AN and then to the most aft-ward (backward) view of DA, with the along-track angle values as $\pm 70.5°$, $\pm 60.0°$, $\pm 45.6°$, $\pm 26.1°$, and $0°$, as depicted in Figure 1.12. It takes about 7 minutes to look at the same scene on the Earth from the DF camera to the DA camera. It has four spectral channels as specified in Figure 1.12, representing blue, green, red, and near infrared. Its retrievals are stored with the spatial resolution of 275 m per pixel, and have the cross-track swath of around 400 km. For geo-registration and storage, the MISR data are broken into a series of predefined, uniformly-sized boxes along the ground track called blocks. Each orbital path is divided into 180 blocks measuring 563.2 km (cross-track) x 140.8 km (along-track). Because of seasonal variations in the portion of the Earth that is in daylight, only up to about 142 blocks further away from the Poles will contain valid data at any particular time (https://eosweb.larc.nasa.gov/content/what-misr-block, accessed December 9, 2017). Looking at the same scene of cloud at the different angles reveals the vertical profile of the cloud to a certain extent, as shown in Figure 1.13.

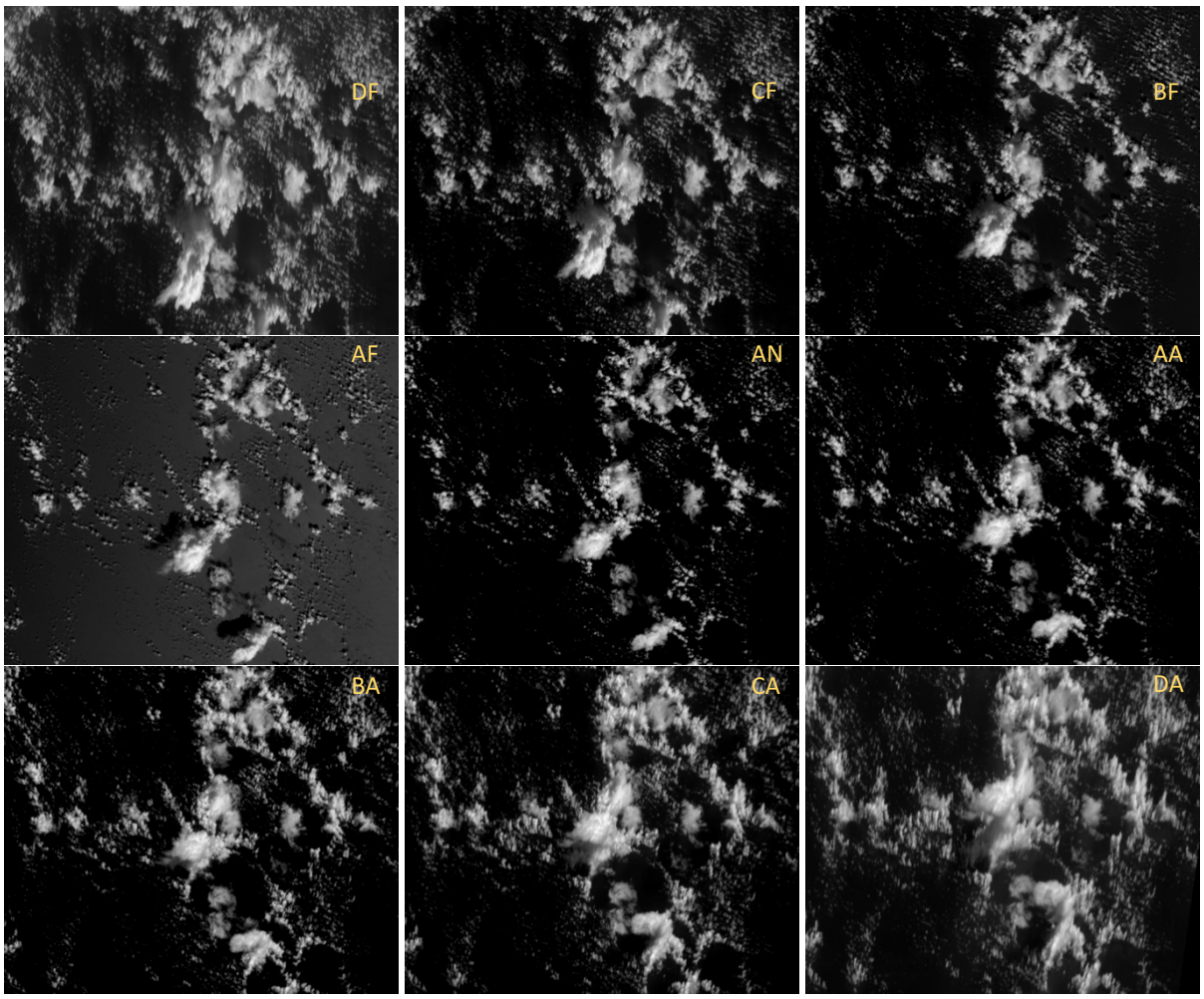

Figure 1.13. An example scene of cloud for all view angles of MISR. From left to right and then down, DF, CF, BF, AF, AN, AA, BA, CA, and DA. The vertical distribution of the cloud is more visible at oblique angles.

MISR's multi-angle characteristic provides the visual information about the vertical distribution of clouds in the along-track direction, the profile of cloud's side in the cross-track direction, and, depending on cases, the top and bottom of cloud. All these are useful information in retrieving the 3-D distribution of cloud geometry.

1.4. Past Studies on Retrieving Cloud Geometry through MISR

A study by Seiz & Davies (2006) attempted at making use of MISR's multi-angle data for the reconstruction of cloud geometry. Nine viewing angles were combined to give eight stereo pairs, which were then analyzed through stereo-photogrammetric methods to measure the geometry of a convective cloud system. Both cloud-top heights and cloud sides were retrieved with a precision of about 200 to 300 m (Seiz & Davies, 2006).

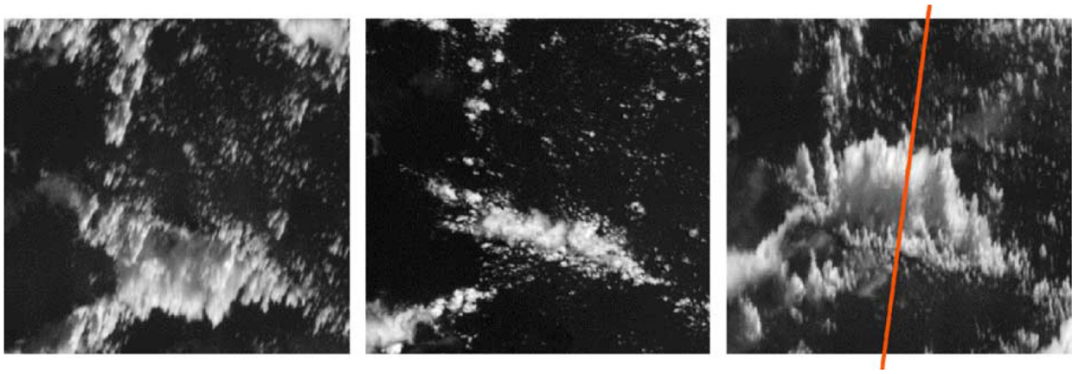

Figure 1.14. Deep convective cloud over ocean, MISR scene on 2 Sep 2003, Path 78, Orbit 19726, blocks 83–86. Df view (Left), An view (center), and Da view (right). Red: cross-section line through the convective cloud. (Seiz & Davies, 2006)

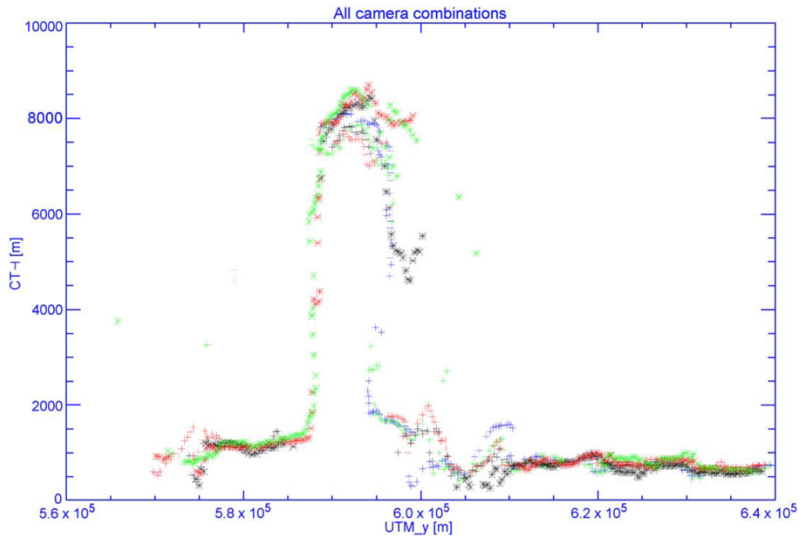

Figure 1.15. Combined plot of all view combinations, Cf-Df, Bf-Cf, Af-Bf, An-Af, An-Aa, Aa-Ba, and Ba-Ca (except Ca-Da), showing the consistent height results of the cloud points along both visible cloud sides as well as at the cloud top. (Seiz & Davies, 2006)

As seen in Figures 1.14 and 1.15, the results were focused on retrieving the cloud top and side heights throughout a 2-D along-track cross-section. The results also assumed that there was negligible cloud motion due to wind throughout the retrieval period from DF to DA. Cornet & Davies (2008) later evaluated the above results by comparing their 3-D radiative transfer simulations with real MISR radiance measurements. In their study, a "good agreement was obtained by making reasonable assumptions regarding the vertical and horizontal distribution of the volume extinction coefficient" (Cornet & Davies, 2008).

Another study by Kassianov et al. (2003) made use of a marine cumulus cloud scene from MISR data to demonstrate a technique for deriving 3-D cloud geometry. They generated their own cloud masks for all the nine view angles, and then applied an algorithm that gives the geometrical thickness for each cloudy pixel from its retrieved radiance at the nadir (AN) view. Then, the values of geometrical thickness were "forced" to agree with the multi-angle

observations (Kassianov et al., 2003). The results were evaluated by comparison with ground-based radar measurements and by using LES simulations coupled with a Monte Carlo method.

There was also a work done by Bill Chapman, one of Prof. Di Girolamo's past staff members. He worked on geometric reconstruction using LES cumulus clouds, under the plane ground assumption and no swath, meaning straight and parallel radiance paths. Figure 1.16 shows his results. The resemblance between the reconstructed cloud volumes and the original LES cloud shows that, in a vertically well-developed and scattered cumulus cloud field, the multi-angle geometric reconstruction could yield convincing results.

Figure 1.16. Comparison between original cloud, reconstructed cloud using 29 view angles, and using 9 view angles. Great resemblance is seen between all three cases.

There have been voices in the scientific community that suggest making use of a technique known as tomography to retrieve cloud properties from passive remote sensing. Tomography involves solving the inverse problem of the radiative transfer equation from the retrievals of radiance at multiple angles, to gain multi-section imaging of the cloud extinction coefficients. The principle is similar to that of CT scan to see bone structures of a human body, but in this case applied to cloud in the atmosphere. One notable study by Levis et al. (2015)

used this technique to retrieve cloud optical depths from MISR-simulated data. Figure 1.17 shows a result and its error from the truth.

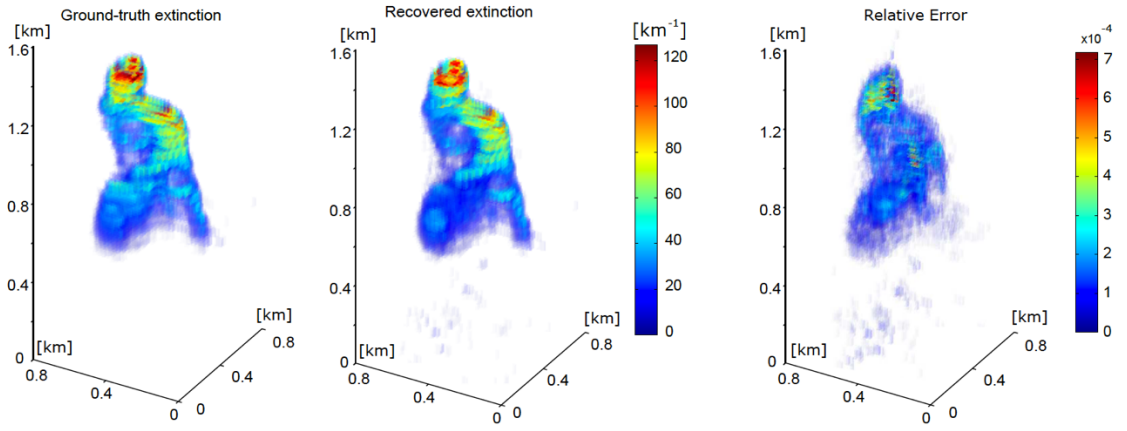

Figure 1.17. Comparison of original extinction field and the tomographically reconstructed extinction field. The unknown extinction field is discretized to a 36 x 36 x 36 grid (46,656 unknowns). A volumetric comparison between the true LES-generated cloud and the recovered cloud, based on initialization that assumed no cloud at all. It is evident from the relative error map that the error is larger in the more opaque regions of the cloud. (Levis et al., 2015)

While the study showed reasonable results and the potential to use the tomographic approach to real MISR data, one limitation has been pointed out, that the problem to be solved in such tomography is non-convex with no convergent point, and that a good initial guess such as where the cloud's outer boundary lies, that is, the cloud geometry, would improve getting to the solution with much less computational demand.

1.5. Statement of the Project

Bearing in mind the necessity of improving our understanding of the real-world 3-D cloud structure and the availability of the extensive MISR data with multi-angle characteristics, this project aims at the binary geometric reconstruction of 3-D cloud volume for several selected MISR scenes. This project aims at visualizing the real-world cloud distribution at select locations and times, by making use of the cloud masks of the selected scene plus the geometric and geographical parameters provided by the MISR science team (Jovanovic et al., 2012) and utilizing simple geometric tricks collectively known as the ray casting. It is my hope that the results from this project are useful in improving our understanding of the impact of cloud structures in the Earth's radiation budget and, at the same time, providing the possibility for the initial guess in the future tomographic research involving real MISR data.

Chapter 2. Procedure and Technical Details

2.1. General Principle

The general principle behind the cloud volume reconstruction in this project is as follows. MISR travels along its orbit above the cloud and captures an image for each different view angle, from DF to AN and then to DA. Then, the captured images, or the pixels with retrieved radiance, are geo-registered on a surface projection, either ellipsoidal or terrain (Jovanovic et al., 1999). The reconstruction simply rewinds this process of MISR's data retrieval and storage. Through a pre-determined cloud domain, rays representing radiance paths from the cloud to the satellite are cast from the cloudy pixels of the image geo-registered on the surface, according to the reported geolocations of the pixels and the satellite's viewing zenith and azimuth angles. Then, the overlapping space at every view angle is taken to be the cloudy parts of the domain, represented by the red hexagon in Figure 2.1.

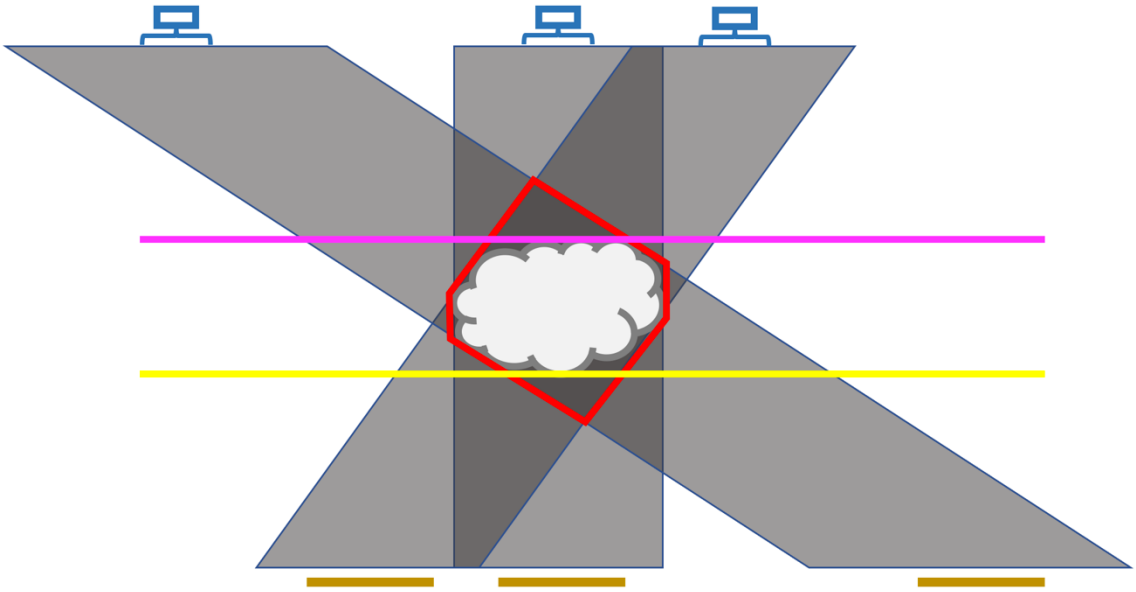

Figure 2.1. A schematic diagram representing the general principle of the reconstruction. The blue sensors at the top represent the satellite retrieving radiance at different view angles. The gray area represents the area occupied by the cloud in the atmosphere from which the radiance is retrieved. The brown at the bottom represents the geo-registered images of the cloud for different view angles. The red represents the overlapping part of the potential cloud locations in the atmosphere at all view angles. The purple represents application of retrieved cloud top height, and the yellow represents potential application of retrieved cloud base height (not included in this project's results).

This reconstruction method already conveys certain level of errors, as seen in the area difference between the initial cloud and the red hexagon in Figure 2.1, especially at the top and the bottom of the cloud. For the excessive overestimation at the top of the cloud, the cloud top height products derived via a stereo-photogrammetric technique by the MISR science team (Moroney et al., 2002; Muller et al., 2002) is applied, and for the overestimation at the bottom, the lifting condensation level from re-analyses data or ground-based observations could be applied as the cloud base height. In this project, the results do not include the application of the cloud bottom height, strictly focusing on the use of MISR data only.

The ray casting method, which traces rays from only the cloudy pixels at each view angle, presumes that any significant parcel of cloud in the atmosphere must be visible at all

view angles. In other words, any parcel of cloud that does not appear in all view angles is considered to have size and optical depth that are negligible for the purpose of volume reconstruction. This assumption also helps evade the pixels that are falsely determined cloudy in the cloud masks due to sun glint, which predominantly appears in only one or few view angles.

2.2. Simulations for Concept Validation

In order to understand the expected outcomes, errors/uncertainties, and limitations of the reconstruction method, simulations were run on a few samples of simple synthetic clouds. Synthetic satellite images were derived from these "synthetic-truth" clouds through the process of image formation, and then were used as inputs in the simulations for cloud volume reconstruction. Then, the reconstructed cloud volumes were compared with the original cloud volumes. All simulations were run with the geometrically straight satellite path as opposed to MISR's orbital (elliptic) path, and under the plane-ground assumption, where the synthetic satellite images are geo-registered to the ground-level plane instead of a terrain or an ellipsoid as in MISR data.

The image formation was conducted as follows. First, from one of the geometrically simple cloud field, a set of synthetic satellite images, which are binary cloud masks in these simulations, were formed in a way that imitates MISR's multi-angle retrievals with its nine along-track view angles of $\pm 70.5°$, $\pm 60.0°$, $\pm 45.6°$, $\pm 26.1°$, and $0°$ (nadir), the orbital height of

705 km, and the consequent swath. The ray casting method of voxel boundary intersections was used, where, if the ray, cast from a pixel placed at its geo-registered location to the supposed location of the synthetic satellite instrument, passed through the boundary of any cloudy voxel within the synthetic cloud field, the pixel was determined cloudy. The voxel boundaries were determined in terms of geometric planes that are either perpendicular to the ground and stretching in either cross-track or along-track direction (along x or y axis), or parallel to the plane ground (along z axis). The image resolution was determined such that for all view angles and all pixels, the ground instantaneous field of view (GIFOV, the ground distance covered by a single pixel), is equal to the ground sampling interval (GSI, the distance between the centers of two adjacent pixels). All view-angle images have their pixels geo-registered to the same locations on the plane ground, with their image centers looking at the same ground point, as shown in Figure 2.2. The satellite locations for the cast rays were determined to imitate the push-broom retrieval technique of MISR, such that for different pixels, the satellite locations change in the along-track axis according to the changes in the pixel locations on the ground, as shown in Figure 2.3, but remain the same in the cross-track axis, giving rise to the angular swath in the synthetic retrievals, as shown in Figure 2.4. Figure 2.5 depicts how each pixel, starting from clear, was determined cloudy based on the how its ray interacts with a boundary plane.

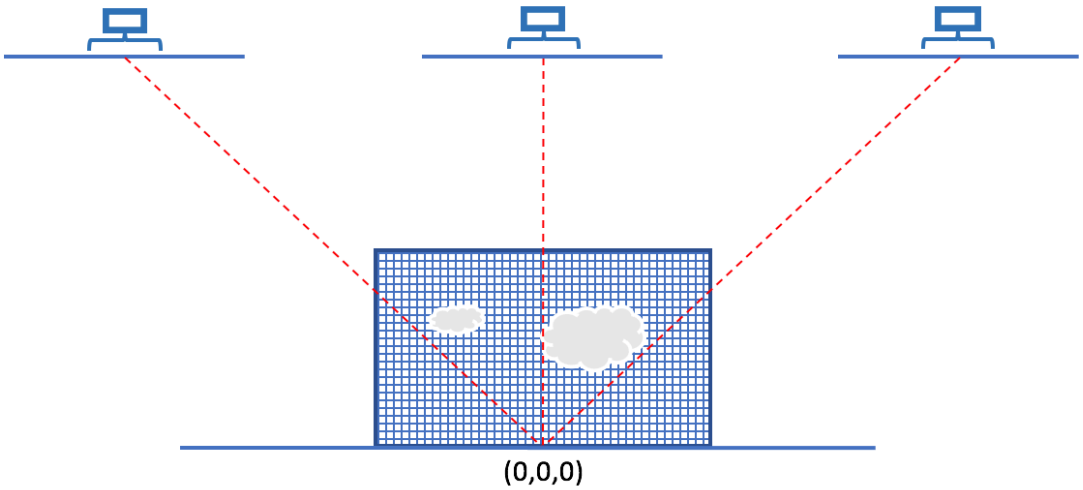

Figure 2.2. For all along-track view angles, the center of the image is looking at the same point on the ground in the original cloud domain, marked (0,0,0).

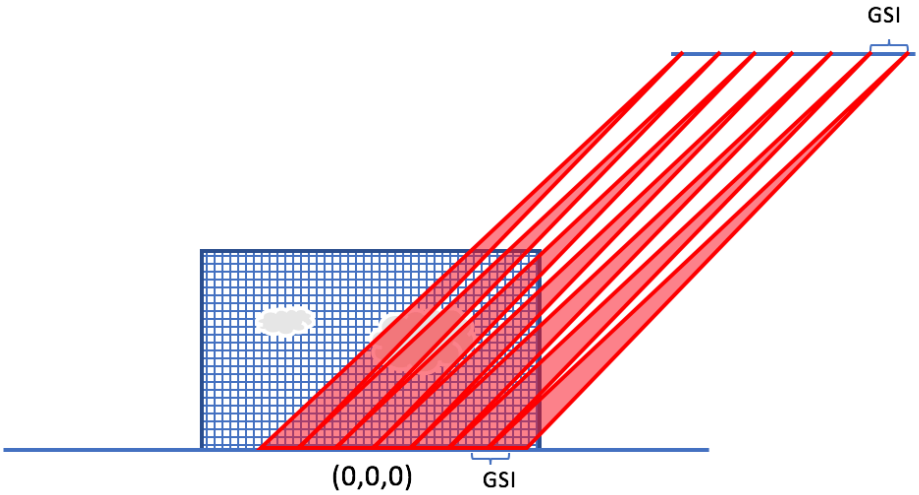

Figure 2.3. The along-track cross-section of the image formation depicting the field of view for each pixel. The synthetic satellite's location changes from pixel to pixel, GSI by GSI.

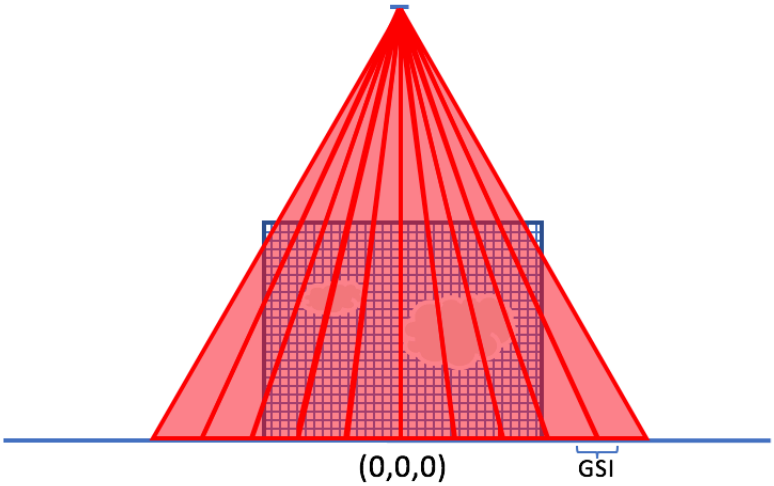

Figure 2.4. The cross-track cross-section of the image formation depicting the field of view for each pixel. The synthetic satellite's location does not change and remain the same from pixel to pixel.

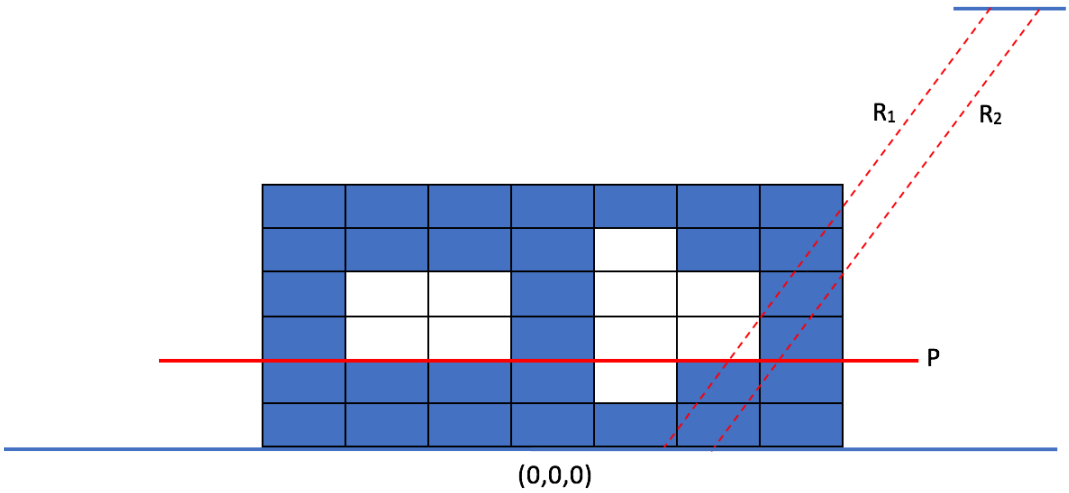

Figure 2.5. A cross-section of the original cloud domain in rectangular voxels, with white representing cloud and blue representing clear. Two rays from different pixels are intersecting with voxel boundary plane P. For R_1, P is the boundary of a cloudy voxel it passes through, so its pixel is determined cloudy. For R_2, P is not the boundary of a cloudy voxel, so nothing is done for its pixel.

Once the synthetic cloud masks were obtained from the image formation, the reconstruction was performed. The procedure for the reconstruction was the reverse of the image formation, where under the same geometric parameters, the rays were cast from cloudy pixels placed at their own geo-registered locations to the satellite's location, and every voxel

whose boundary was intersected by the rays was determined to be cloudy. Figure 2.6 shows this process.

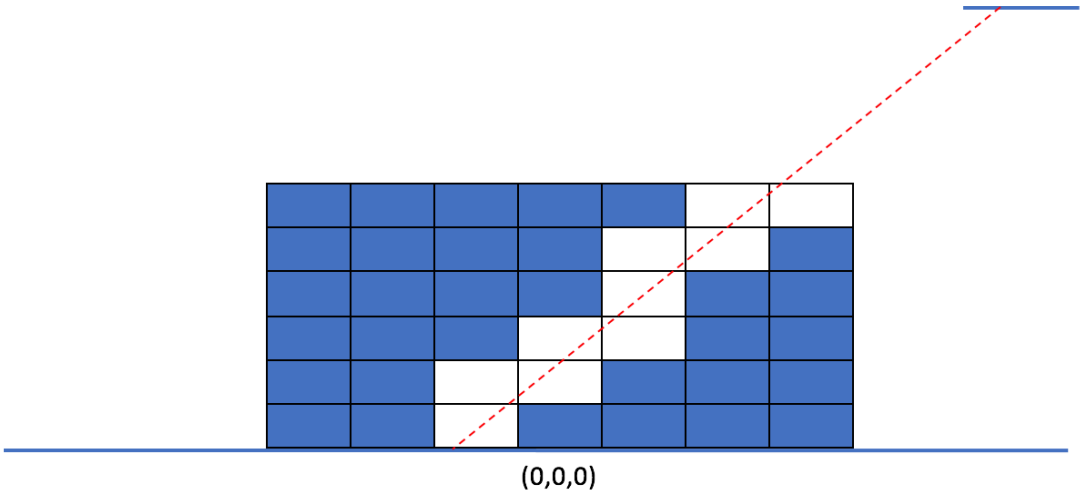

Figure 2.6. A cross-section for the reconstruction for one view angle and one ray from a cloudy pixel. All voxels the ray passes through is determined cloudy.

After repeating this process for all nine view angles, only the voxels that have been determined cloudy by all angles were eventually determined to be cloudy. The number of rays cast per pixel in each axis, cross-track or along-track, was determined based on the ratio of the pixel size to the voxel size, such that $N_{ray} = round_{down}\left(\frac{S_p}{S_{v\_min}}\right) + 2$, where N_{ray} is the number of rays per pixel in either axis, S_p the pixel size in the same axis, and S_{v_min} the smallest voxel size among all three axes. The starting points of all the rays per pixel were evenly distributed, starting from the corners, within the rectangular sampling interval of the pixel's corresponding geolocation.

In order to investigate the effect of cloud shape on the reconstruction, the following synthetic case simulations were run with four geometrically simple clouds: single cubic cloud,

cross-track row cloud, along-track row cloud, and vertical column cloud. The initial voxel size of the original cloud was set as 1375 x 1375 x 1375 m, and the cloud bottom was placed at the altitude of 5.5 km. The row or column clouds were all set to each consist of 7 voxels in line and to be located at the horizontal center of the image domain. The pixel size in the image formation was set as 275 x 275 m, and the reconstruction domain's voxel size was set as 275 x 275 x 275 m. Figure 2.7 shows the synthetic binary cloud masks derived from the image formation for each of the four clouds. Figures 2.8 to 2.11 show the reconstruction results of the simulations. Figure 2.8 shows how overestimation is found all around the reconstructed cloud, which is due to the nature of the algorithm that casts the rays to the corners of the pixel's rectangular GIFOV and determines to be also cloudy any voxel whose corner is passed through by any of the cast rays. Besides, as seen especially more vividly in Figure 2.10, the reconstruction under MISR's nine view angles always produces prism-like shape in the along-track direction at the top and the bottom of the cloud, which is the result of the geometry of the satellite view angles.

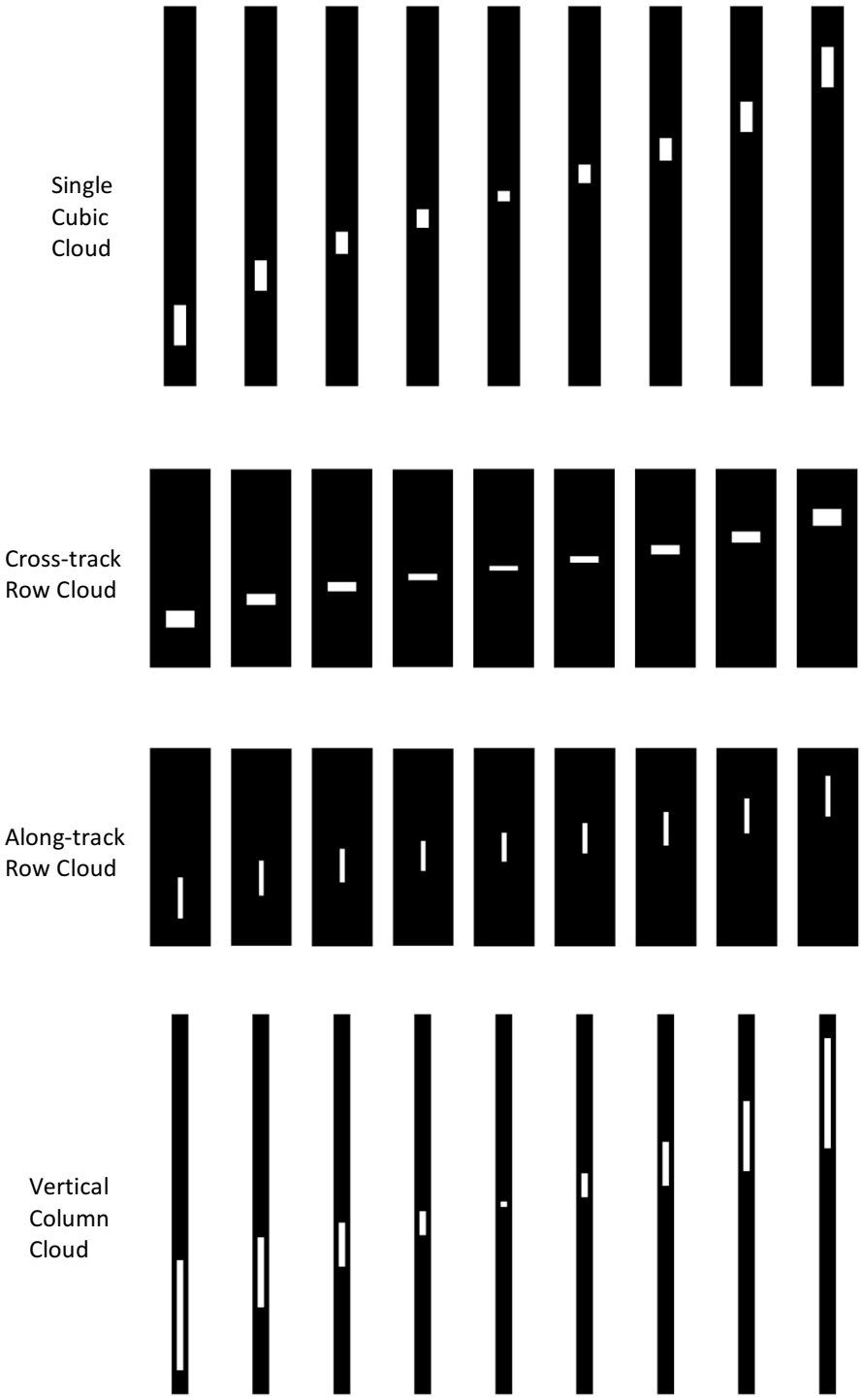

Figure 2.7. Nine view-angle images for each of the four synthetic clouds. From left to right, DF, CF, BF, AF, AN, AA, BA, CA, and DA. Along-track in top-bottom direction, and cross-track in left-right direction. The cross-track swath remains the same for all along-track view angles. All images are looking at the center of each cloud domain. The image sets between different clouds are <u>not</u> in the same scale. Notice how the level of along-track oblique extension differs for each type of cloud.

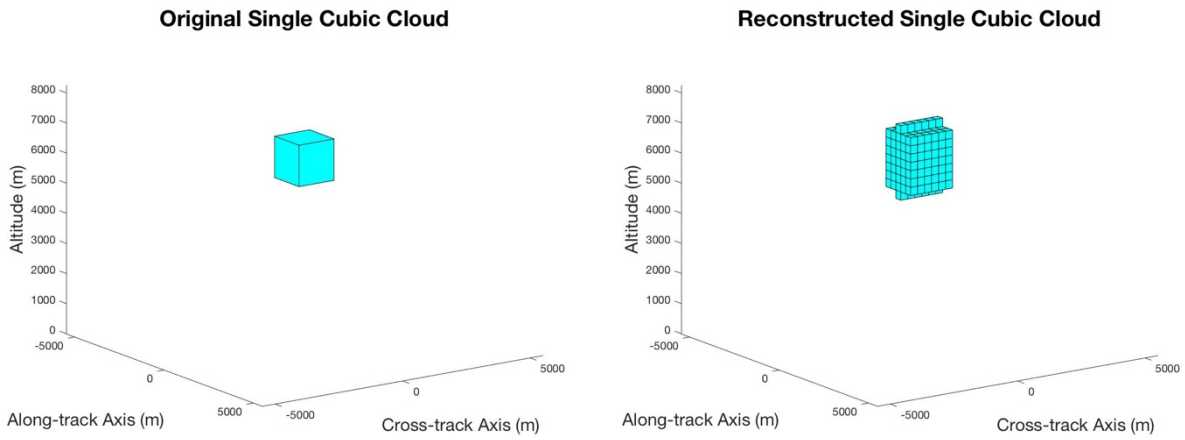

Figure 2.8. Comparison between the original single cubic cloud and the reconstructed single cubic cloud. Overestimation is found all around the reconstructed cloud.

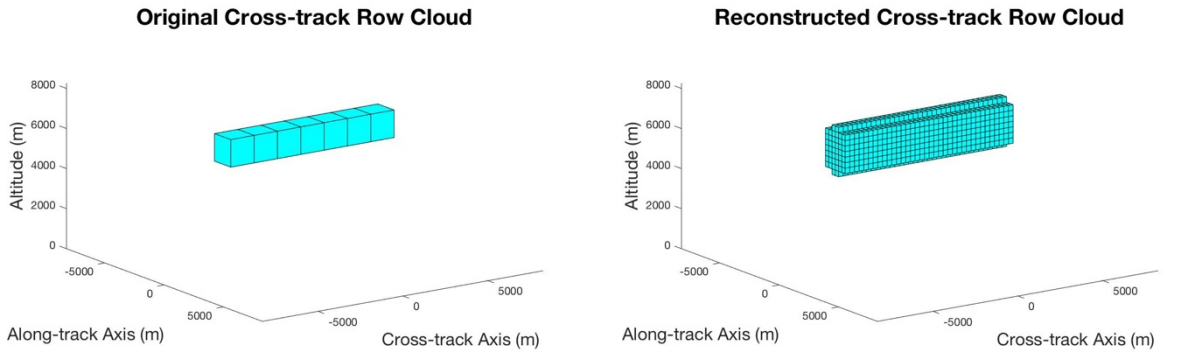

Figure 2.9. Comparison between the original cross-track row cloud and the reconstructed cross-track row cloud.

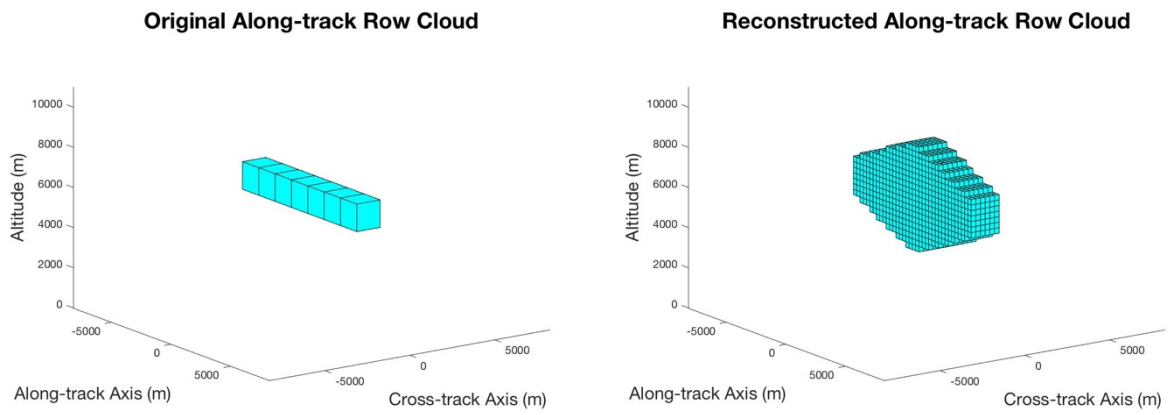

Figure 2.10. Comparison between the original along-track row cloud and the reconstructed along-track row cloud. Overestimation is particularly great in this case, due to the building of prism in the along-track direction.

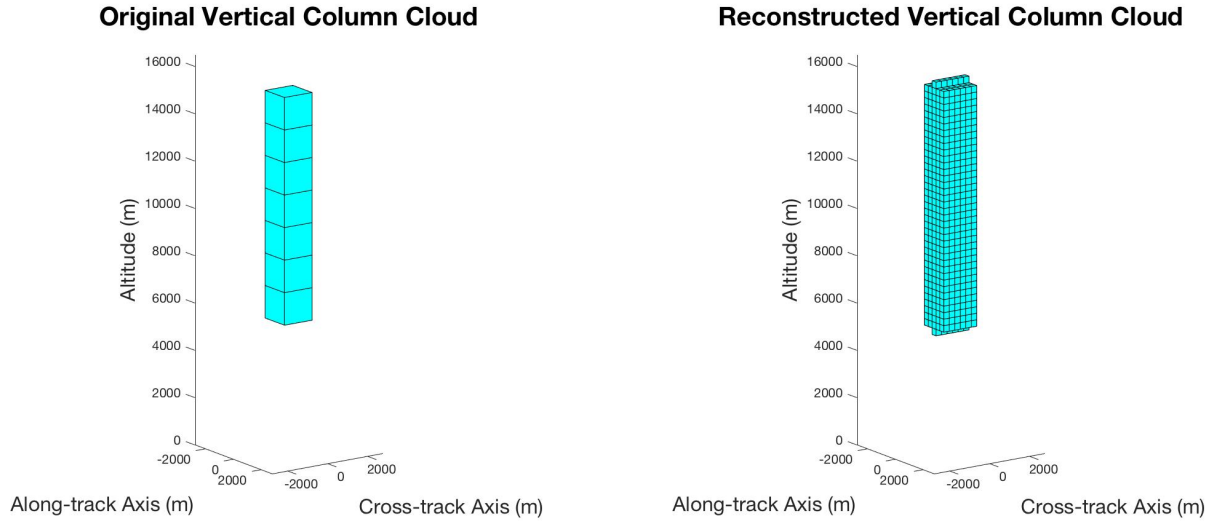

Figure 2.11. Comparison between the original vertical column cloud and the reconstructed vertical column cloud.

In the case of the single cubic voxel cloud, the reconstruction overestimated in volume by a factor of 1.78. In the case of the cross-track row cloud, 1.89. In the case of the along-track row cloud, 3.22, which is more substantial than other cases. And lastly, in the case of the vertical column cloud, 1.28, which is less substantial than other cases. We see overestimation in

all cases because of the fundamental limitation in the reconstruction method, as explained in Section 2.1.

Overall, we see the general trend in the overestimation values, that the less horizontally spread out in the along-track direction and the more vertically developed the cloud is, the less the overestimation would be. Hence, this reconstruction method would yield the best results when applied to regions with vertically well-developed and horizontally narrow cumulus clouds. Moreover, intuitively, we see that having more oblique view angles would lead to better results by providing additional information on the cloud top and bottom, especially in the cases of cloud spread out in along-track direction (as in Figure 2.10).

The actual values of overestimation depend on numerous factors other than the cloud shape. One is the resolution effect between the initial cloud size and the image formation's pixel size. The coarser resolution of the satellite images will lead to the greater effect of the mismatching resolution, and therefore greater overestimation (Di Girolamo & Davies, 1997). The smaller cloud size in comparison to the pixel size leads to the greater overestimation of the cloudiness, because the pixel is still determined cloudy by the smaller presence of the cloud. Other factors include the location of clouds with respect to the satellite location within the camera swath, and the view angle values used.

In order to investigate the effect of satellite instrument's resolution on the accuracy of the reconstructed cloud volume, a series of simulations were run with differing values of synthetic satellite image resolutions. A total of 15 different pixel sizes were tested, on the initial single cubic cloud with the arbitrarily chosen voxel size of 1375 x 1375 x 1375 m and the bottom placed at the altitude of 5.5 km. The reconstruction voxel size was set as 27.5 x 27.5 x 27.5 m

for all 15 cases, which was small enough to see the differences between the reconstruction results and reasonable for the code's runtime. The view angles remained the same as the MISR view angles. After the reconstruction was performed, a graph was derived to examine the relationship between the reconstruction overestimation and the satellite image's pixel size. Table 2.1 shows the factor of overestimation for each input pixel size. Figure 2.12 visualizes four example reconstruction results.

Table 2.1. Table showing each input pixel size and the corresponding ratio of the pixel size to the initial voxel size, the number of cloudy pixels in the synthetic satellite cloud mask, the consequent cloudy area calculated by multiplying the number of pixels to the pixel area, and the factor of overestimation by the reconstructed volume. Notice how the cloudy area in the cloud mask decreases in general as the pixel size decreases.

Pixel Size (m)	Ratio of Initial Voxel Size to Pixel Size	Number of Cloudy Pixels in Synthetic Cloud Mask		Area of Cloudy Pixels in Synthetic Cloud Mask (m^2)		Factor of Overestimation
		DF	AN	DF	AN	
1375	1	10	4	18906250	7562500	4.684800
687.5	2	24	9	11343750	4253906	2.631600
343.75	4	80	20	9453125	2363281	1.621872
275	5	120	30	9075000	2268750	1.519680
171.875	8	288	81	8507813	2392822	1.604208
137.5	10	440	110	8318750	2079688	1.391280
125	11	516	132	8062500	2062500	1.380280
85.9375	16	1054	272	7784058	2008789	1.342656
68.75	20	1617	441	7642852	2084414	1.372064
62.5	22	1955	506	7636719	1976563	1.312704
55	25	2522	676	7629050	2044900	1.317056
42.96875	32	4216	1122	7784058	2071564	1.365120
34.375	40	6468	1722	7642852	2034785	1.350016
31.25	44	7774	2070	7591797	2021484	1.325424
27.5	50	9984	2652	7550400	2005575	1.280448

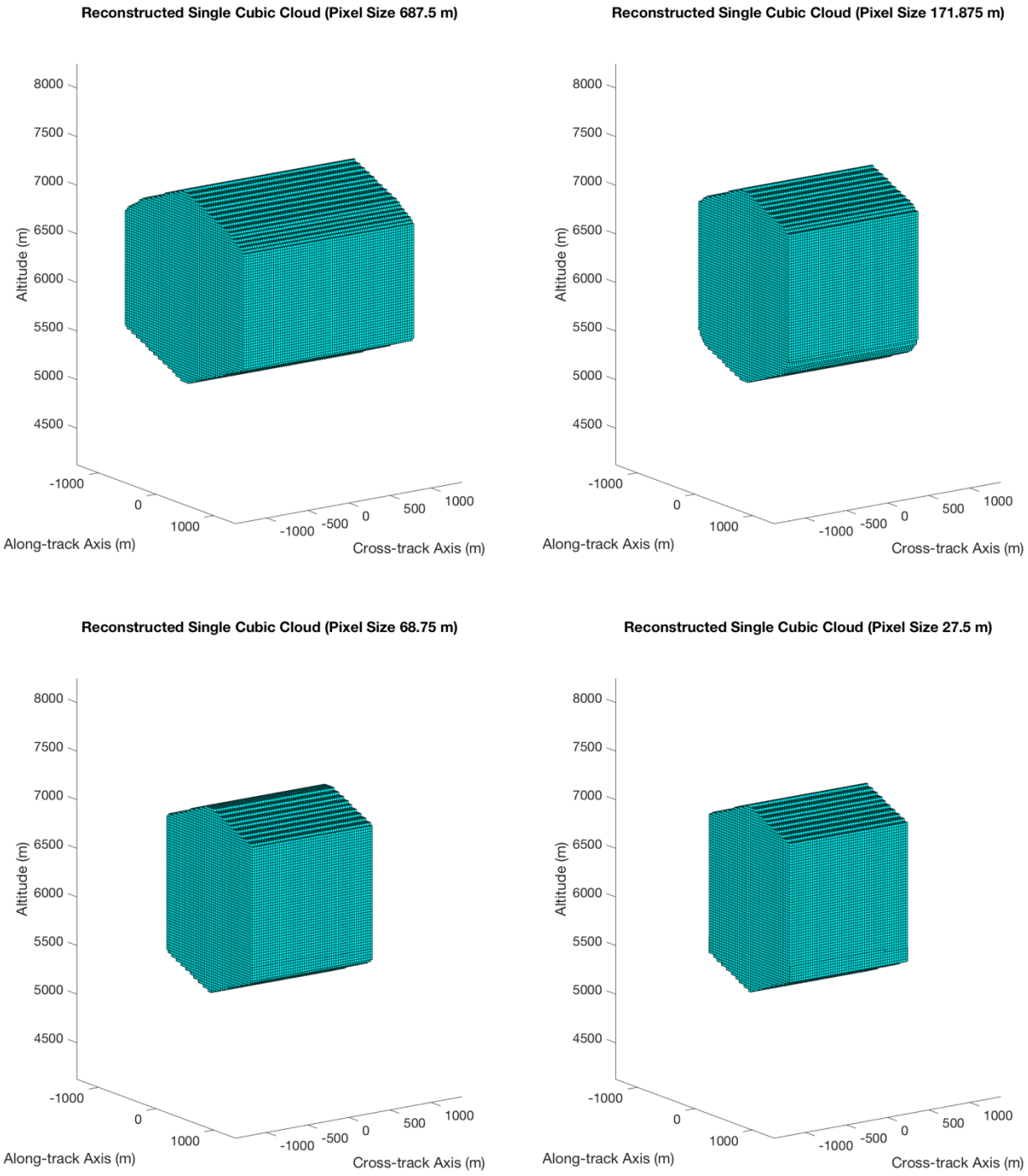

Figure 2.12. Reconstructions of the single cubic cloud at four different pixel resolutions of the synthetic satellite image, namely 687.5 m, 171.875 m, 68.75 m, and 27.5 m. All plots are in the same scale. As seen in this figure and in Table 2.1, the overestimation decreases as the pixel size decreases.

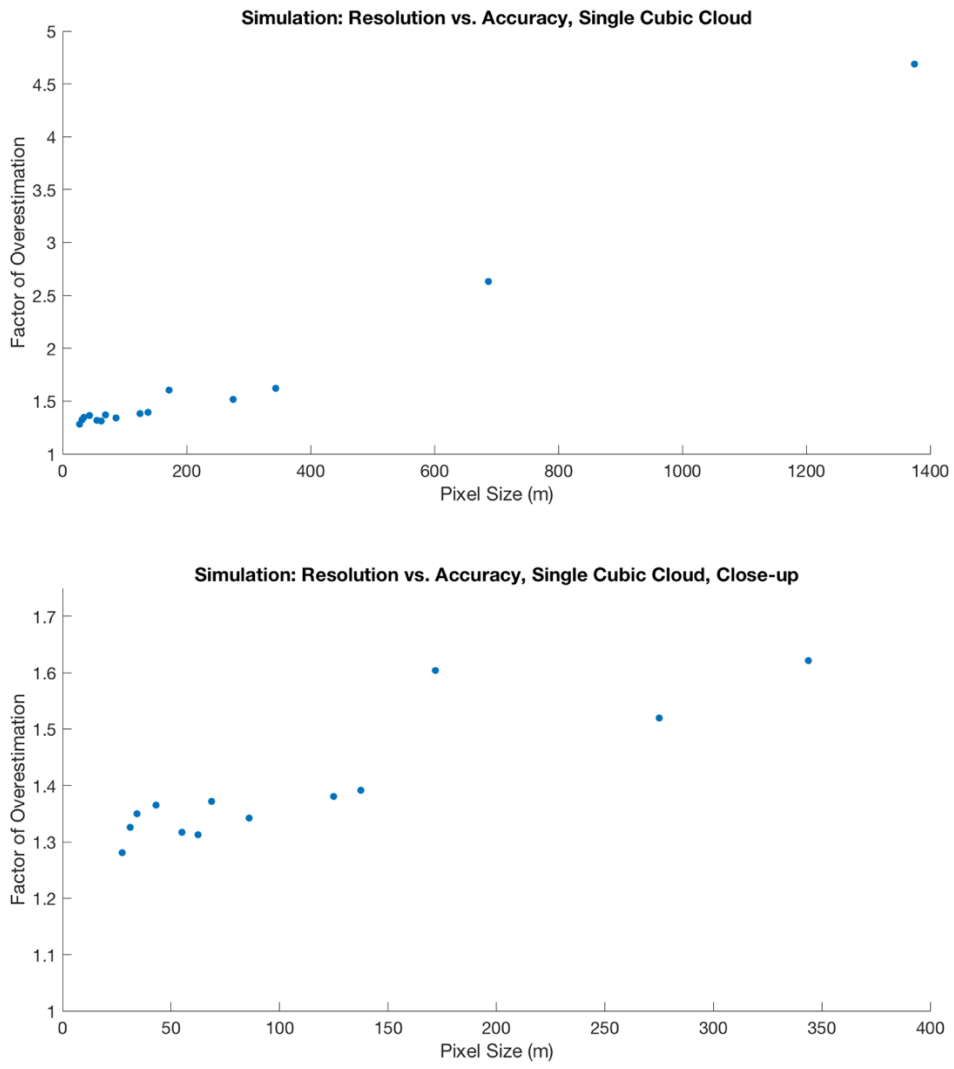

Figure 2.13. Upper: a graph showing the correlation between the factor of overestimation and the satellite image pixel size. Bottom: the close-up of the upper graph on the 13 points with the smallest pixel size. All reconstructions were performed under the same reconstruction voxel size of 27.5 x 27.5 x 27.5 m. Overall, a positive correlation is seen.

Figure 2.13 shows the correlation between the reconstruction overestimation and the pixel size of the synthetic satellite images. While the plots are not monotonic due to the mismatching between the satellite image grid and the reconstruction domain grid, overall the smaller resolution of the satellite image leads to more accurate reconstruction, and therefore the factor of overestimation decreases and approaches the value of 1. The value of 1 cannot be

reached, however, due to the nature of the reconstruction method which always carries certain level of error at the top and the bottom of the cloud, as explained in Section 2.1. This issue can be mitigated if the instrument has more oblique view angles.

In order to investigate whether it is as meaningful to have reconstructions at coarser resolution with respect to the resolution of input satellite images and reduce the computation cost, simulations were run that resemble the previous simulations with differing input pixel sizes, except that the reconstructions were performed with the reconstruction voxel size matching the corresponding input pixel size. In other words, if the pixel size was C x C m for some constant C, then the resultant voxel size was set as C x C x C m. The simulations were run for a total of 18 different pixel sizes, with the first 15 being the same as the previous simulations' inputs. The initial cloud volume and all other geometric parameters remained the same. Table 2.2 and Figure 2.14 show the results.

Table 2.2. Table showing the same variables as in Table 2.1, for the simulations with the resultant voxel size matching the pixel size of the synthetic cloud masks.

Pixel Size or Resultant Voxel Size (m)	Ratio of Initial Voxel Size to Pixel Size	Number of Cloudy Pixels in Synthetic Cloud Mask		Area of Cloudy Pixels in Synthetic Cloud Mask (m^2)		Factor of Overestimation
		DF	AN	DF	AN	
1375	1	10	4	18906250	7562500	12.000000000000
687.5	2	24	9	11343750	4253906	4.500000000000
343.75	4	80	20	9453125	2363281	1.875000000000
275	5	120	30	9075000	2268750	1.776000000000
171.875	8	288	81	8507813	2392822	1.757812500000
137.5	10	440	110	8318750	2079688	1.518000000000
125	11	516	132	8062500	2062500	1.451540195342
85.9375	16	1054	272	7784058	2008789	1.361328125000
68.75	20	1617	441	7642852	2084414	1.375500000000
62.5	22	1955	506	7636719	1976563	1.308978211871
55	25	2522	676	7629050	2044900	1.344512000000
42.96875	32	4216	1122	7784058	2071564	1.348876953125
34.375	40	6468	1722	7642852	2034785	1.308562500000
31.25	44	7774	2070	7591797	2021484	1.293858001503
27.5	50	9984	2652	7550400	2005575	1.280448000000
25	55	12027	3135	7516875	1959375	1.249460555973
21.484375	64	15990	4225	7380638	1950169	1.240272521972
17.1875	80	24867	6480	7345964	1914258	1.213734375000

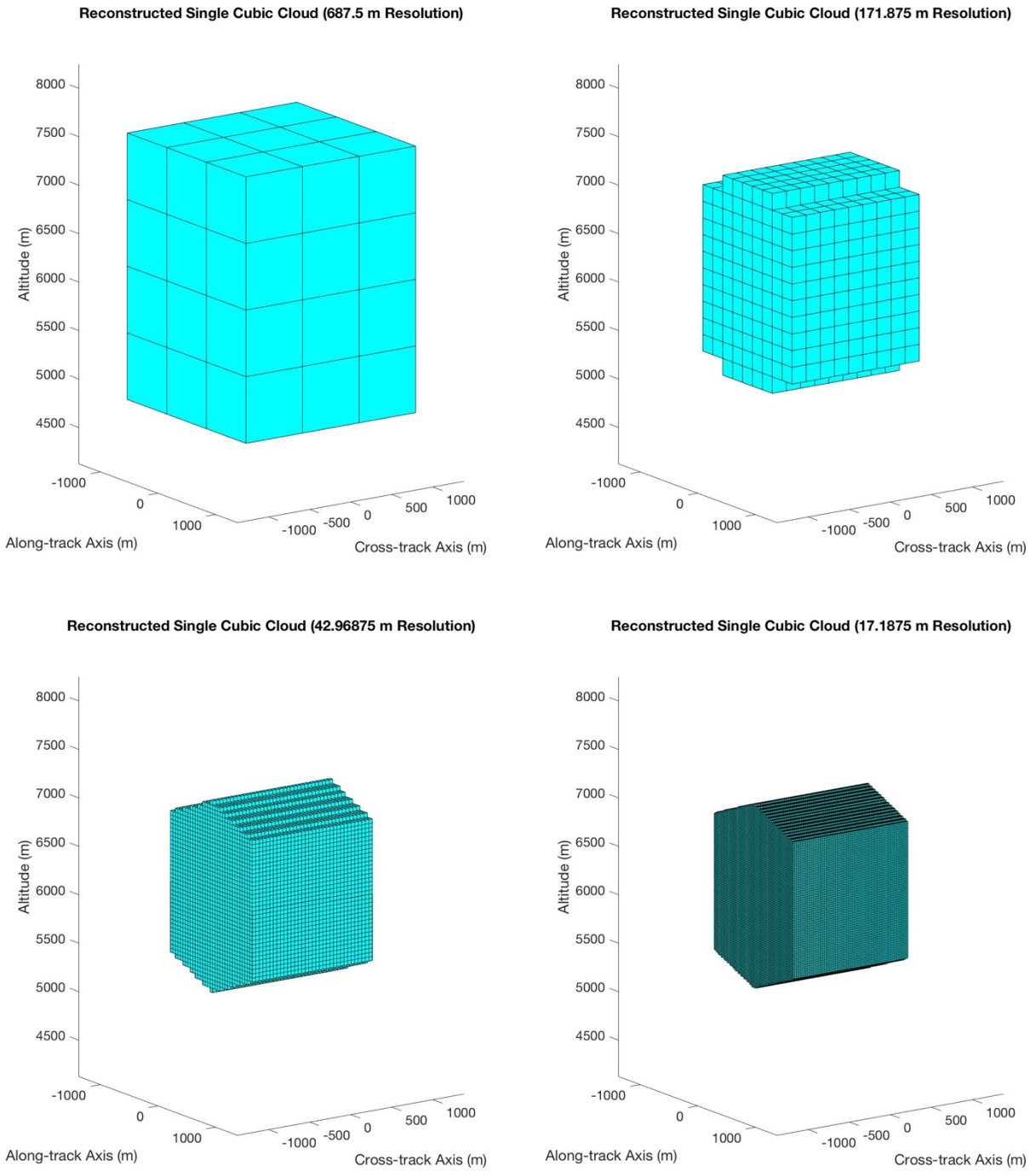

Figure 2.14. Reconstructions of the single cubic cloud at four different resolutions of 687.5 m, 171.875 m, 42.96875 m, and 17.1875 m. The reconstruction voxel size matches each pixel size. All plots are in the same scale. The reduction in the reconstructed cloud volume is evident as the pixel size decreases.

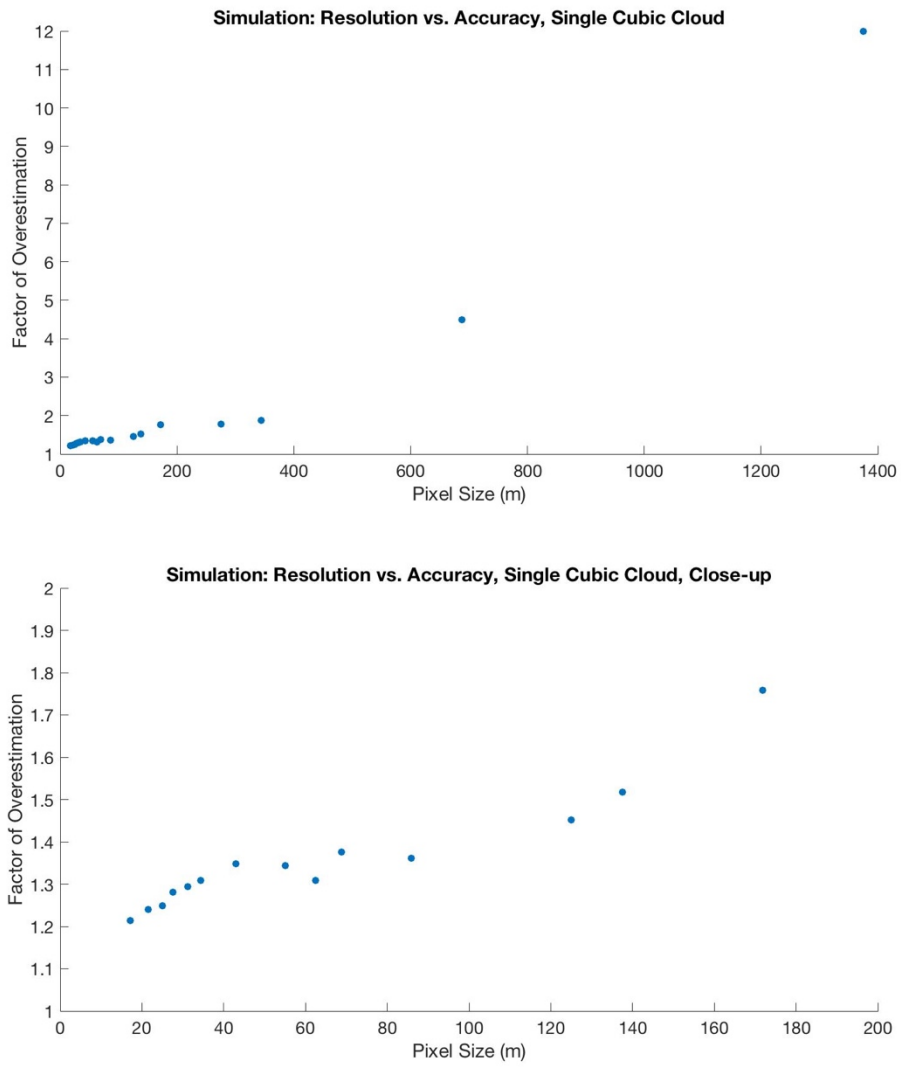

Figure 2.15. Upper: a graph showing the correlation between the synthetic satellite image pixel size (reconstruction voxel size) and the factor of overestimation. Bottom: the close-up on the 14 points with the smallest pixel size. Overall, a positive correlation is seen.

In comparison to Figure 2.13, Figure 2.15 shows a more consistently positive correlation. Although a smaller reconstruction voxel size would always lead to more accurate results than a larger voxel size, it is worthwhile to study the extent of the impact of the voxel size, due to the high computational demand of the reconstructions at small values. Whether the reconstruction with the voxel size matching each pixel size is as meaningful in comparison to the more

computationally demanding reconstruction with the smaller voxel size as previously shown can be examined by looking at the difference between the two sets of the factor of overestimation. The difference is calculated for the first 15 input pixel sizes shared by both simulation sets.

Table 2.3. Table showing the difference in the factor of overestimation between Table 2.1 and Table 2.2. At pixel size 27.5 m, the difference is zero since the reconstruction variables for both simulations sets are the same.

Pixel Size or Resultant Voxel Size (m)	Ratio of Initial Voxel Size to Pixel Size	Difference in Factor of Overestimation
1375	1	7.315200
687.5	2	1.868400
343.75	4	0.253128
275	5	0.256320
171.875	8	0.153605
137.5	10	0.126720
125	11	0.071260
85.9375	16	0.018672
68.75	20	0.003436
62.5	22	-0.003726
55	25	0.027456
42.96875	32	-0.016243
34.375	40	-0.041454
31.25	44	-0.031566
27.5	50	0

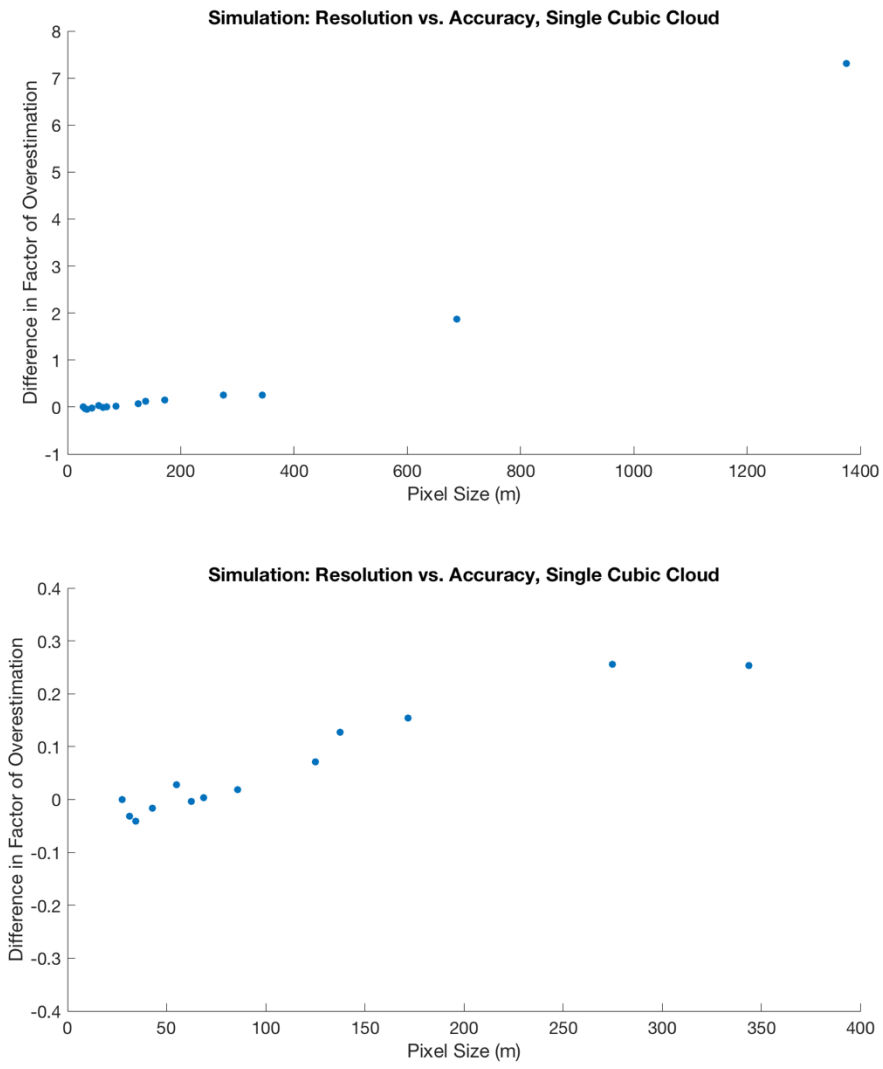

Figure 2.16. Upper: a graph showing the difference in the factor of overestimation between the reconstruction under voxel size matching pixel size and the reconstruction under voxel size 27.5 m, at different input pixel sizes. At the pixel size 343.75 m or below (or at the ratio of the cubic cloud size to the pixel size 4 or greater), the difference becomes close to 0. Bottom: the close-up on the 13 points with the smallest pixel size. Some of the negative values are due to the lasting effect of the mismatching resolution between the satellite image grid and the reconstruction domain grid.

The results shown in Table 2.3 and Figure 2.16 demonstrate that, for input pixel sizes that are small enough in comparison to the size of the initial cloud, the reconstruction with the voxel size matching the pixel size is good enough to produce results that are close to those of the reconstruction with the voxel size set to be much smaller than the pixel size. This is a useful

reference in determining the voxel size for the reconstruction of the real-world cloud distribution from MISR data.

2.3. Reconstruction from MISR: Overview

The reconstruction from MISR entails details that are unique in comparison to the simulations described in the previous section. For the inputs of MISR images, we used two different cloud masks. The first is the Radiometric Camera-by-Camera Cloud Mask (RCCM), generated by the MISR science team. Another is the custom cloud mask, independently derived in this project.

Since the reconstruction process is the rewinding of MISR's data retrieval process, it is necessary to consider how MISR stores its data. MISR geo-registers the retrieved data to two types of surface projection: ellipsoidal and terrain. In this project, only the MISR data on the ellipsoid projection are used. The ellipsoidal projection makes use of the World Geodetic System 1984 (WGS84) ellipsoid, where the data is registered to the surface of the ellipsoid. Hence, instead of the plane-ground surface as in the simulations, the curvature of the surface of the Earth should be considered during the reconstruction.

Once the cloud domain is defined with the proper ellipsoid and geographical parameters provided by the MISR science team, the ray casting is conducted. The cast rays are defined by combining geometric parameters for MISR image pixels provided by the MISR science team and the proper geometry resulting from the ellipsoid and the geographical parameters. The ray casting methods used in the MISR cloud volume reconstructions in this project are two, namely

the method of distance threshold (DTH), and the method of voxel boundary intersections (VBI) which was already introduced in the simulations in Section 2.2. These are explained further in Section 2.8.

It is also necessary to take into account the time difference between different view-angle images of the same cloud scene, since different view angles look at the same scene and retrieve radiance at different times, with DF observing the first and DA the last. The time difference between the most forward camera and the most backward camera is about 7 minutes, during which the cloud could have displaced greatly depending on its cloud type and the wind present around it. This gives rise to the necessity of wind correction, to adjust the cloud in different view-angle images to the same moment of time for which the reconstruction is performed. This remains a challenging issue in the accurate reconstruction of the cloud volume, and is further explained in Section 2.7.

2.4. Reconstruction from MISR: Reconstruction Domain

The first step in the reconstruction of a cloud volume is to determine its domain consisting of voxels. Since the reconstruction from MISR data concerns the real-world distribution of clouds over the globe, it is imperative to define a domain geometrically proper to the surface used for the geo-registration of MISR data. The ellipsoidal projection used for MISR data is defined by the reference World Geodetic System 1984 (WGS84) ellipsoid. The ellipsoid is defined with the equatorial radius of 6378137 m, the flattening factor of 298.257223563, and consequently the

polar radius of 6356752 m (NGA, 2014). All MISR data are stored on a two-dimensional grid that results from the projection of this ellipsoid through the space-oblique Mercator (SOM) projection. The SOM projection is a space-based map projection where the reference great ellipse nominally follows the ground track of the satellite. It "provides a mapping from latitude/longitude to a coordinate system that is approximately aligned with the MISR swath" (Jovanovic et al., 1999). While the mathematical transformation from the ellipsoid to the SOM map projection is complex, a simple diagram can help demonstrate the general idea of how it works, as shown in Figure 2.17. The mathematical details can be found in a map projection working manual (Snyder, 1987).

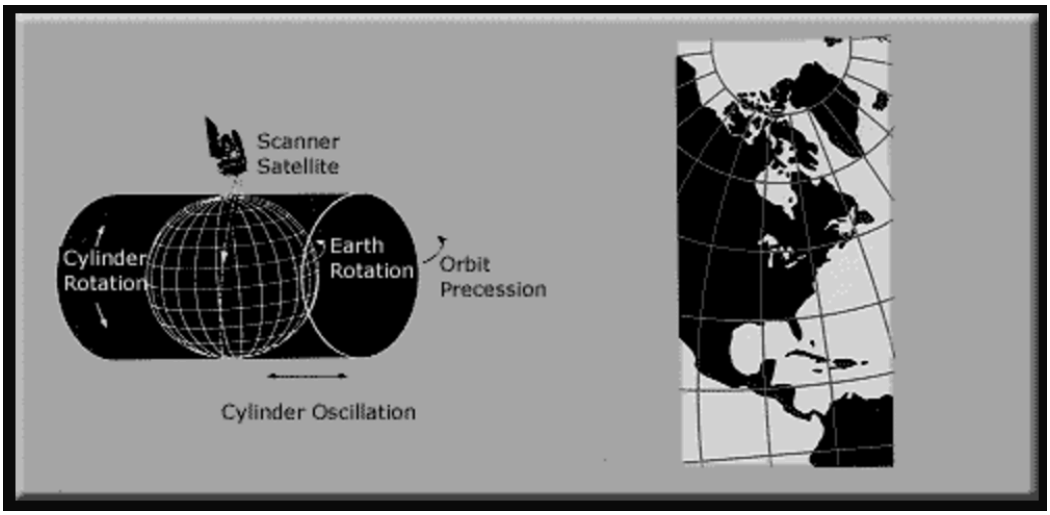

Figure 2.17. A diagram showing the SOM projection from the Earth ellipsoid. A reference great ellipse on the globe is selected such that it deviates the least and remains closest to the satellite's curved ground track. Then, the points on the globe are projected to the cylinder tangent to and surrounding the ellipsoid, such that there are as least distortions due to the map projection as possible near the reference great ellipse, within the relatively narrow band along the ground track. Picture from https://egsc.usgs.gov/isb//pubs/MapProjections/projections.html (accessed December 9, 2017).

The fact that the area near the great ellipse on the ellipsoid, to which the surrounding cylinder is tangent, experiences the least distortion makes SOM projection preferable for

satellite orbital map imaging such as MISR's, which consists of 233 unique orbital paths covering the entire globe, for each of which the individual SOM projection has been derived with its unique and unchanging geolocations in latitude and longitude. The axis along the direction of the reference great ellipse nominally following the ground track of the orbit is named SOM X, and the axis perpendicular to SOM X is named SOM Y, as shown in Figure 2.18.

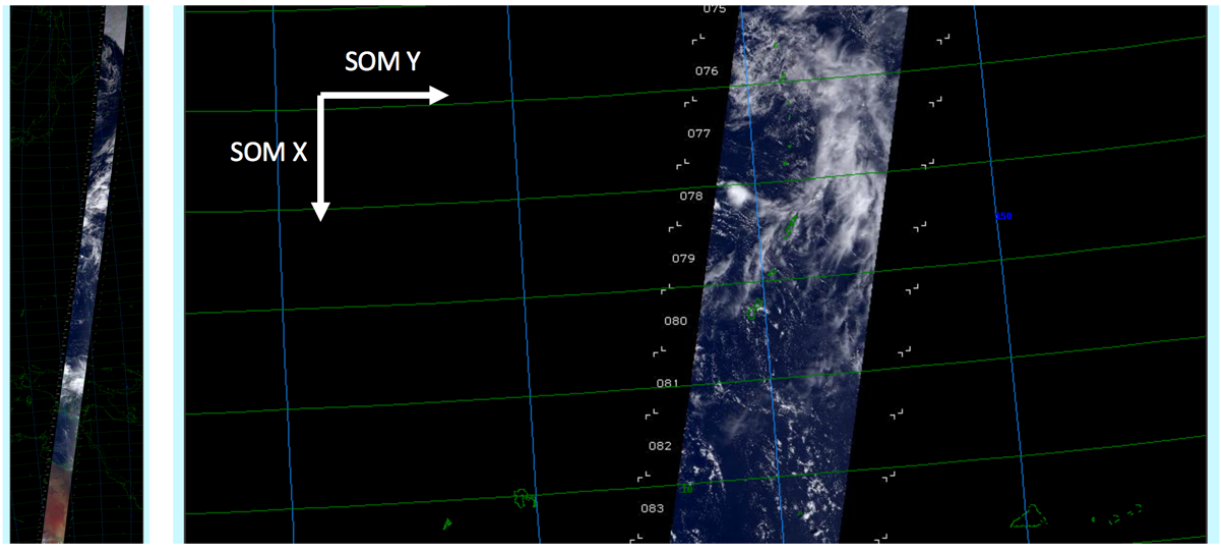

Figure 2.18. Example RGB images showing MISR Orbit 36649, Camera AN, on the SOM grid unique to its Path No. 100. Pictures from https://l0dup05.larc.nasa.gov/MISR_BROWSE/orbit (accessed December 9, 2017).

In this project, SOM X and SOM Y are used as the horizontal axes, and the altitude as the vertical axis, of the reconstructed cloud volume domain. Hence, it follows that each voxel forms a shape that is not a strictly rectangular cuboid but one slightly bent vertically upward at its horizontal center, whose size increases as the altitude increases. This is similar to how the 3-D grid cells are defined in climate models (https://www.climate.gov/maps-data/primer/climate-models, accessed December 9, 2017), as shown in Figures 2.19 and 2.20.

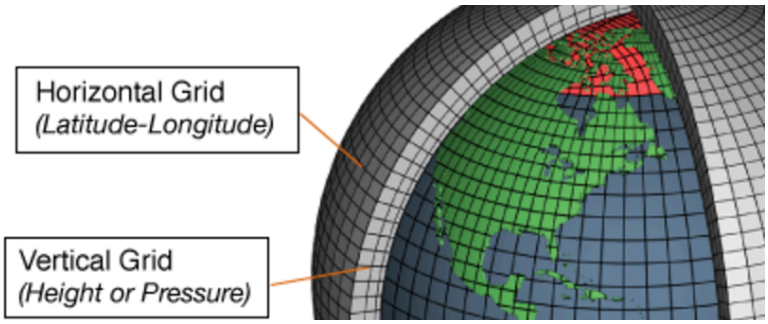

Figure 2.19. A diagram showing 3-D grid cells in climate models. The reconstruction domain would resemble the diagram, consisting of voxels formed by altitudinal protrusion of the geo-registered pixels each of which has its own latitude and longitude values. Picture from https://celebrating200years.noaa.gov/breakthroughs/climate_model/modeling_schematic.html (accessed December 9, 2017).

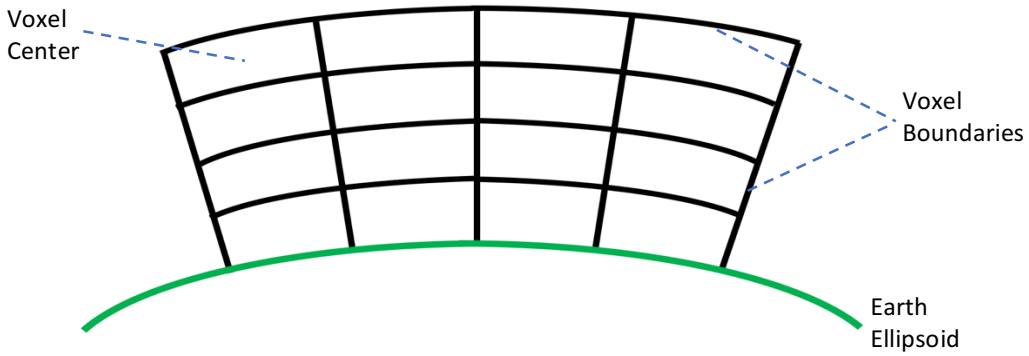

Figure 2.20. A diagram depicting the 2-D cross-section of a simplified reconstruction domain. Each voxel size slightly increases as the altitude increases.

For the reconstruction ray casting, which is further explained in Section 2.8, the voxel properties such as its central locations and boundaries need to be defined. All the calculations involving the WGS84 ellipsoid, the voxel centers, the voxel boundaries, and the pixel locations are done with respect to the three-dimensional Cartesian coordinates, with the center of the ellipsoid as the origin.

The voxel boundaries are determined in terms of geometric planes normal to the Earth ellipsoid and stretching along SOM X or SOM Y, and ellipsoidal segments with the semi-principal

axes equal to the Earth ellipsoid's semi-principal axes plus the corresponding altitude. The geometric plane is defined by the best-fit plane of the corner points of the geo-registered pixels with the same SOM X or SOM Y value. The latitude and longitude values of the pixel corner points are calculated from the interpolations of the reported geolocations with respect to SOM X and SOM Y grid values, which are further explained in Section 2.5. Then, the Cartesian coordinates of the corner points are calculated and used in the method of least squares to derive the best-fit planes.

The central locations of all voxels are defined in terms of the corresponding pixel's latitude, longitude, and the distance from the center of the ellipsoid (the origin). This distance minus the distance between the pixel's geolocation on the ellipsoidal surface and the origin can be considered as the voxel center's altitude, as the scale of the reconstruction domain is small in comparison to that of the ellipsoid, with the deviation between the two lines reaching around 100 m at the altitude of 30 km (see Appendices A.4 and B for more detail).

The ellipsoidal reconstruction needs to be employed in the reconstructions from real MISR data as opposed to the plane-ground assumption used in Section 2.2, as the two may show a significant difference in the reconstruction results. It was calculated, for the reconstruction from the RCCM, that the ellipsoidal reconstruction domain, in comparison to the plane-ground reconstruction domain, could have a voxel grid distortion reaching around 10 m and the block grid distortion reaching around 870 m at the altitude of 20 km. Here, the voxel grid distortion is defined as the difference between the horizontal voxel length at the aforementioned altitude and the RCCM pixel size of 1.1 km, and the block grid distortion is defined as the difference between the the horizontal length of the reconstruction domain over

the block at the same altitude and the RCCM block size (see Appendices A.4 and B for more detail).

2.5. Reconstruction from MISR: Input Data

This section details the input MISR data used in the cloud volume reconstruction. All the data used can be retrieved from https://search.earthdata.nasa.gov/ (accessed December 9, 2017), the website available for downloading science products for Earth Observing System Data and Information System (EOSDIS) by National Aeronautics and Space Administration (NASA). The MISR science products have been developed by various members of the MISR science team. The list of the products used are as follows:

- MISR Radiometric Camera-by-camera Cloud Mask (RCCM) V004
- MISR Level 1B2 Ellipsoid Data V003
- MISR Ancillary Geographic Product (AGP) V001
- MISR Geometric Parameters (GMP) V002
- MISR Level 2 TOA/Cloud Height and Motion Parameters (TC_CLOUD) V001

The RCCM is one of the two input MISR cloud masks used in the volume reconstruction. It has been calculated on a camera-by-camera basis, meaning that each view-angle cloud mask has been derived independently of one another. The algorithm and theoretical basis for the derivation of the RCCM can be found in the MISR Algorithm Theoretical Basis Document (ATBD)

for Level 1 Cloud Detection (Diner et al., 1999), with the update for over ocean given by Zhao & Di Girolamo (2004).

The RCCM provides a variable named “Cloud”, which consists of block images in 128x512 pixels in 5 different levels of classification: high-confidence cloud, low-confidence cloud, low-confidence clear, high-confidence clear, and no retrieval. In this project, the code has been written such that the different classification levels can be selected to mean cloudy for the binary cloud volume reconstruction. The RCCM pixels are assumed to have GIFOV and GSI equal to 1.1 km. Although, in reality, the RCCM’s GIFOV increases at oblique angles to as far as 1.53 km in the along-track direction, the effect of cloud overestimation by the oblique extension is negligible (Zhao & Di Girolamo, 2004). Figure 2.21 shows an example image of the RCCM.

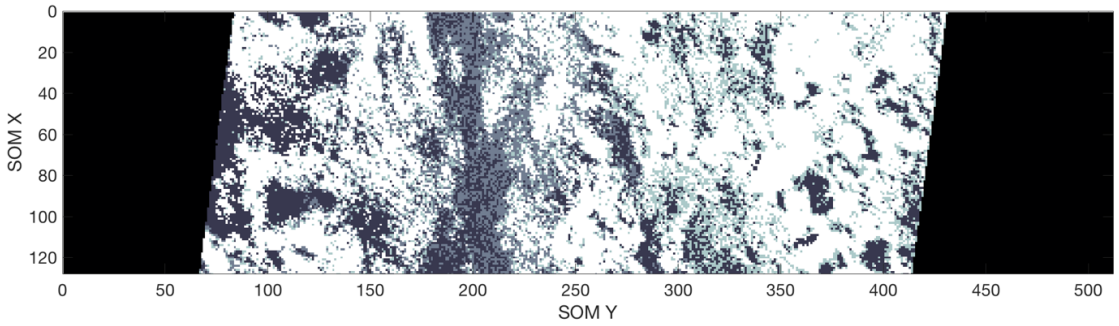

Figure 2.21. An example image of the RCCM, Orbit 36649, Block 83, view angle AN. White pixels indicate high-confidence cloud. Greenish pixels indicate low-confidence cloud, usually found around the edges of cloud. Light gray indicates low-confidence clear, and darker gray high-confidence clear. Black indicates either no retrieval or fill-value.

The L1B2 Ellipsoid data provides the values of the retrieved radiance in unsigned 16-bit integers, at the spectral channels of red, green, blue, and near infrared (NIR). The radiance variables consist of block images in 512x2048 pixels with the pixel size 275 m for all view angles,

except for all the non-AN (non-nadir) block images of green, blue, and NIR which have 128x512 pixels with the pixel size 1.1 km. Hence, the images with the lower pixel number were interpolated to match the higher pixel number. First, the bilinear interpolation was done to the image with 128x512 pixels. Then, the resolution-sharpening algorithm was applied as follows so that clouds and their structures in the images may be more detectable by the human eye.

1. Perform the mean-value decimation on the initial 512x2048-pixel red image to obtain a 128x512-pixel red image.
2. Perform the bilinear interpolation on the decimated 128x512-pixel red image to obtain an interpolated 512x2048-pixel red image.
3. For each pixel, calculate the radiance ratio, r, such that $r = \frac{R_{red}}{R_{red\_interp}}$, where R_{red} is the initial red radiance and R_{red_interp} is the radiance of the interpolated red image.
4. Sharpen the bilinearly interpolated non-AN green, blue, and NIR images by multiplying to them the radiance ratio r (see Appendices A.3 and B for more detail).

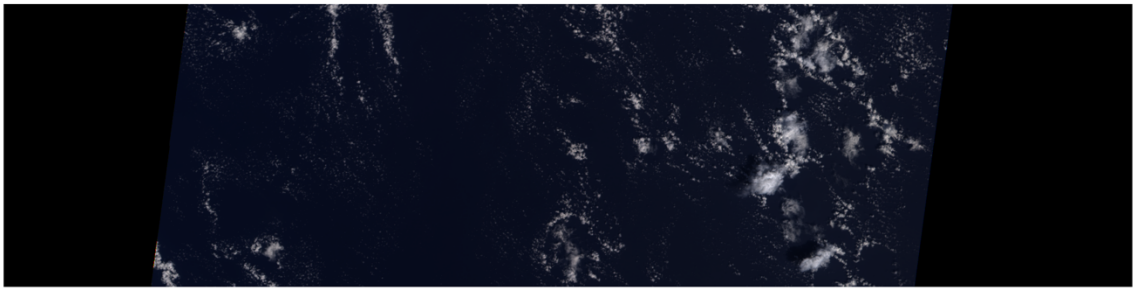

Figure 2.22. The MISR RGB image of the same scene as in Figure 2.21. The seeming overestimation of cloud in the RCCM image is due to the RCCM's clear-conservative characteristic, where a very small amount of cloud inside a pixel may contribute to the cloud detection of the pixel.

Figure 2.22 shows an example MISR RGB image. The RGB images were used in selecting scenes appropriate for the reconstruction, in the derivation of the corresponding custom cloud masks, and in the validation of the reconstruction results, the details of which are explained in later sections. The Ellipsoid data also provides the variable "PerBlockMetadataTime", which gives the reference time for each block at each view angle.

The Ancillary Geographic Product (AGP) provides the geographical locations for each pixel, in the variables named "GeoLatitude" and "GeoLongitude". The variables are at the pixel number of 128x512, same as in the RCCM. Hence, while the interpolation is not needed for the RCCM, it is for the custom cloud mask whose pixel number is 512x2048. Here, the polynomial interpolation was used by finding, for either the set of latitude values or the set of longitude values in each block, the best-fit equation of an elliptic paraboloid in the form $z = C_1x^2 + C_2y^2 + C_3xy + C_4x + C_5y + C_6$, where C_i is a constant for $i \in \{1,2,3,4,5,6\}$, with respect to the SOM X and SOM Y coordinates of the pixels.

The polynomial interpolation used here and throughout this project can be termed the method of least-squares 2nd degree polynomials. For the case above, given the datasets (x_1, y_1), (x_2, y_2), …, (x_n, y_n), where $n > 6$, x_i represent SOM X coordinates, and y_i represent SOM Y coordinates, and the dataset z_i which represent either the reported latitude or longitude values, the best-fit polynomial $f(x, y) = C_1x^2 + C_2y^2 + C_3xy + C_4x + C_5y + C_6$ has the least-squares error from z_i when $\sum_{i=1}^{n}[z_i - f(x_i, y_i)]^2 = \sum_{i=1}^{n}[z_i - (C_1x_i^2 + C_2y_i^2 + C_3x_iy_i + C_4x_i + C_5y_i + C_6)]^2$ is minimized. This means that, for each unknown coefficient C_i, the function yields the first derivative equal to zero.

$$\sum_{i=1}^{n} x_i^2[z_i - (C_1x_i^2 + C_2y_i^2 + C_3x_iy_i + C_4x_i + C_5y_i + C_6)] = 0$$

$$\sum_{i=1}^{n} y_i^2[z_i - (C_1x_i^2 + C_2y_i^2 + C_3x_iy_i + C_4x_i + C_5y_i + C_6)] = 0$$

$$\sum_{i=1}^{n} x_iy_i[z_i - (C_1x_i^2 + C_2y_i^2 + C_3x_iy_i + C_4x_i + C_5y_i + C_6)] = 0$$

$$\sum_{i=1}^{n} x_i[z_i - (C_1x_i^2 + C_2y_i^2 + C_3x_iy_i + C_4x_i + C_5y_i + C_6)] = 0$$

$$\sum_{i=1}^{n} y_i[z_i - (C_1x_i^2 + C_2y_i^2 + C_3x_iy_i + C_4x_i + C_5y_i + C_6)] = 0$$

$$\sum_{i=1}^{n} [z_i - (C_1x_i^2 + C_2y_i^2 + C_3x_iy_i + C_4x_i + C_5y_i + C_6)] = 0$$

Expanding the above equations, we get:

$$\sum_{i=1}^{n} x_i^2z_i = C_1\sum_{i=1}^{n} x_i^4 + C_2\sum_{i=1}^{n} x_i^2y_i^2 + C_3\sum_{i=1}^{n} x_i^3y_i + C_4\sum_{i=1}^{n} x_i^3 + C_5\sum_{i=1}^{n} x_i^2y_i + C_6\sum_{i=1}^{n} x_i^2$$

$$\sum_{i=1}^{n} y_i^2z_i = C_1\sum_{i=1}^{n} x_i^2y_i^2 + C_2\sum_{i=1}^{n} y_i^4 + C_3\sum_{i=1}^{n} x_iy_i^3 + C_4\sum_{i=1}^{n} x_iy_i^2 + C_5\sum_{i=1}^{n} y_i^3 + C_6\sum_{i=1}^{n} y_i^2$$

$$\sum_{i=1}^{n} x_iy_iz_i = C_1\sum_{i=1}^{n} x_i^3y_i + C_2\sum_{i=1}^{n} x_iy_i^3 + C_3\sum_{i=1}^{n} x_i^2y_i^2 + C_4\sum_{i=1}^{n} x_i^2y_i + C_5\sum_{i=1}^{n} x_iy_i^2 + C_6\sum_{i=1}^{n} x_iy_i$$

$$\sum_{i=1}^{n} x_iz_i = C_1\sum_{i=1}^{n} x_i^3 + C_2\sum_{i=1}^{n} x_iy_i^2 + C_3\sum_{i=1}^{n} x_i^2y_i + C_4\sum_{i=1}^{n} x_i^2 + C_5\sum_{i=1}^{n} x_iy_i + C_6\sum_{i=1}^{n} x_i$$

$$\sum_{i=1}^{n} y_iz_i = C_1\sum_{i=1}^{n} x_i^2y_i + C_2\sum_{i=1}^{n} y_i^3 + C_3\sum_{i=1}^{n} x_iy_i^2 + C_4\sum_{i=1}^{n} x_iy_i + C_5\sum_{i=1}^{n} y_i^2 + C_6\sum_{i=1}^{n} y_i$$

$$\sum_{i=1}^{n} z_i = C_1 \sum_{i=1}^{n} x_i^2 + C_2 \sum_{i=1}^{n} y_i^2 + C_3 \sum_{i=1}^{n} x_i y_i + C_4 \sum_{i=1}^{n} x_i + C_5 \sum_{i=1}^{n} y_i + C_6 \sum_{i=1}^{n} 1$$

Hence, the coefficients C_i were found by solving the above linear equations. The similar linear equations were derived and solved for all other polynomial interpolations in this project. The errors incurred due to the polynomial interpolations were found to be all negligible (see Appendices A and B for how errors were calculated).

The Geometric Parameters (GMP) provide the camera viewing zenith and azimuth values for each pixel, which were used to define the direction vectors for the cast rays during the cloud volume reconstruction. The viewing angles give the direction from the pixel's geolocation to the satellite, and are defined with respect to the local north (x axis), the local east (y axis), and the direction normal to the ellipsoid and into the ground (z axis). Figure 2.23 displays the configurations of the camera viewing angles.

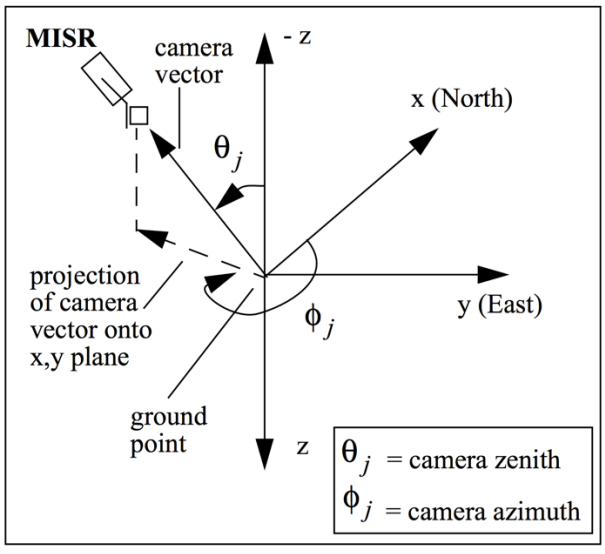

Figure 2.23. A diagram showing the geometry of the camera viewing angles. The zenith is measured between the satellite direction and the –z axis. The azimuth is measured clockwise looking from above, from the local north to the projection of the satellite direction onto the plane tangent to the ellipsoidal point corresponding to the pixel's geolocations. (Bull et al., 2005)

The camera viewing zenith and azimuth are provided for each block and each view angle (Df, Cf, …, Da) at the pixel number of 8x32, with the pixel size equal to 17.6 km. For both the RCCM and the custom cloud mask, the viewing angles were interpolated to match the resolutions. The interpolation was conducted as follows: First, for each pixel with camera zenith θ and camera azimuth ϕ, the local x-y coordinates of a point, located in the direction of the viewing zenith and azimuth at the distance of 1 from the pixel's geolocation as the local origin, were derived with the equations $x_{local} = \sin(\theta)\cos(\phi)$ and $y_{local} = \sin(\theta)\sin(\phi)$. Then, for each block, the polynomial interpolation with the elliptic paraboloid was conducted, to find the best-fit equation for the x_{local} values and for the y_{local} values, with respect to the latitude and longitude values of the pixels. Then, the interpolated values of x_{local} and of y_{local} were converted back to the zenith and azimuth values, through the same equations above and the conditions that $0° \leq \theta < 90°$ and that $0° \leq \phi < 360°$.

The Level 2 TOA/Cloud Height and Motion Parameters (TC_CLOUD) contain the variables "CloudMotionNorthward" and "CloudMotionEastward", which provide the speed of the cloud motion at the top of the pixel's cloud in the direction of the north or the east, at the pixel number of 8x32 for each block, and "CloudTopHeight_WithoutWindCorrection" (CTH_WWC), which gives the apparent cloud top height, and "CloudTopHeight" (CTH), which takes cloud displacement due to wind into account in its derivation, for each cloudy pixel at the pixel number of 128x512 per block. All the variables are reported at the reference time of the AN camera. The details of the derivations of the cloud motion and cloud top height variables can be found in MISR Level 2 Cloud Product Algorithm Theoretical Basis (Mueller et al., 2013). The cloud motion variables can be used to represent the wind field of the scene during the wind

correction, which is explained in Section 2.7. The two cloud top height variables were combined such that, given CTH which provides information for less number of pixels than CTH_WWC, all its no-retrieval pixels have been replaced with the pixels in CTH_WWC. Then, the combined cloud top height was applied to the reconstructed cloud volume during the ray casting, the details of which are explained in Section 2.8.

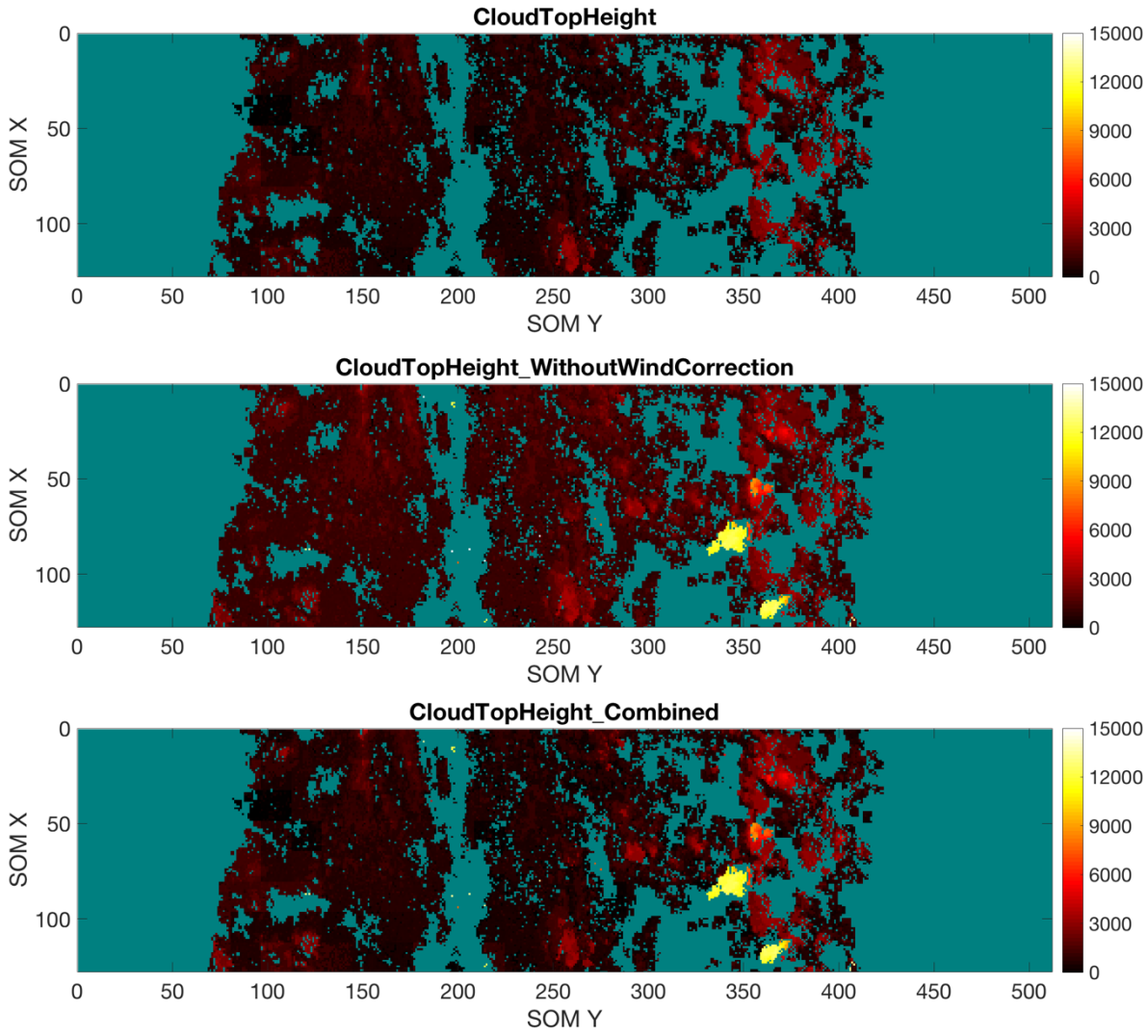

Figure 2.24. An example image of "CloudTopHeight", "CloudTopHeight_WithoutWindCorrection", and the two combined, Orbit 36649, Block 83. The height is expressed in meters in the spectrum of red-yellow-white colors. Brighter indicates taller clouds. The blue-green indicates no retrieval.

2.6 Reconstruction from MISR: Custom Cloud Mask

The custom cloud masks have been developed from the MISR RGB ellipsoid data for a few select scenes, so as to reconstruct the cloud volumes at the better 3-D resolutions, i.e. smaller voxel size, than the RCCM. This is possible because MISR RGB radiance data are provided at the pixel resolution of 275 m while the RCCM are at the pixel resolution of 1.1 km. Two different methods were used in the pixel classifications: red channel threshold and whiteness deviation threshold. All the input scenes chosen for reconstruction in this project had ocean, or water, in the background, where the RCCM is known to perform very well in comparison to other background types such as land with vegetation or land with desert (Diner et al., 1999).

Taking advantage of the fact that the clouds in oceanic scenes often scatter more solar radiation than the background (except at times in sun glint), we used the red channel radiance data, which are provided at the finer resolution of 275 m for all view angles, by putting threshold for cloudiness. The red channel threshold is determined by finding a value between 0 and 1, which is multiplied to the difference between the highest and the lowest red radiance values within the block, and then added to the minimum value to get the radiance threshold value. Pixels with values above the radiance threshold value are then classified as cloudy. In other words, for every pixel with the red channel radiance value, $R_{r,i}$, where 'r' represents 'red' and 'i' represents the individual pixel, the pixel is determined cloudy if $R_{r,i} \geq R_{r,min} + T_{RC}\left(R_{r,max} - R_{r,min}\right)$, where T_{RC} is the input value with $0 < T_{RC} < 1$, $R_{r,min}$ is the block's lowest radiance value, and $R_{r,max}$ the highest. Essentially, this is not different from simply choosing a radiance threshold value for each block, as in the paper by Zhao & Di Girolamo (2007).

Another method, termed the whiteness deviation threshold method, was created to take advantage of the fact that the clouds are "whiter" in color than the background. For each pixel, it first calculates the mean radiance value among the red, green, and blue channels. Then, it calculates the difference between each channel's radiance value and the mean value, and puts the threshold on the ratio of the largest difference value among the three to the mean value. Below certain threshold, the pixel is considered white enough be classified as cloudy. In other words, for the pixel with the red radiance value $R_{r,i}$, the green radiance value $R_{g,i}$, and the blue radiance value $R_{b,i}$, it is determined cloudy if $\frac{\max\left(\left|R_{r,i}-\frac{\left(R_{r,i}+R_{g,i}+R_{b,i}\right)}{3}\right|,\left|R_{g,i}-\frac{\left(R_{r,i}+R_{g,i}+R_{b,i}\right)}{3}\right|,\left|R_{b,i}-\frac{\left(R_{r,i}+R_{g,i}+R_{b,i}\right)}{3}\right|\right)}{\frac{\left(R_{r,i}+R_{g,i}+R_{b,i}\right)}{3}} \leq T_{WD}$, where T_{WD} is the whiteness deviation threshold input with $0 < T_{WD} < 1$.

In both methods, the threshold values were chosen independently, through human-eye tests of trial and error, for each view angle. However, the values in many cases ended up being the same for different view angles. In the end, the cloud mask derived from the red channel threshold and the one derived from whiteness deviation threshold were combined such that if a pixel is classified as cloud in either test, then it is finally classified as cloud. Figures 2.25 to 2.27 show example custom cloud masks.

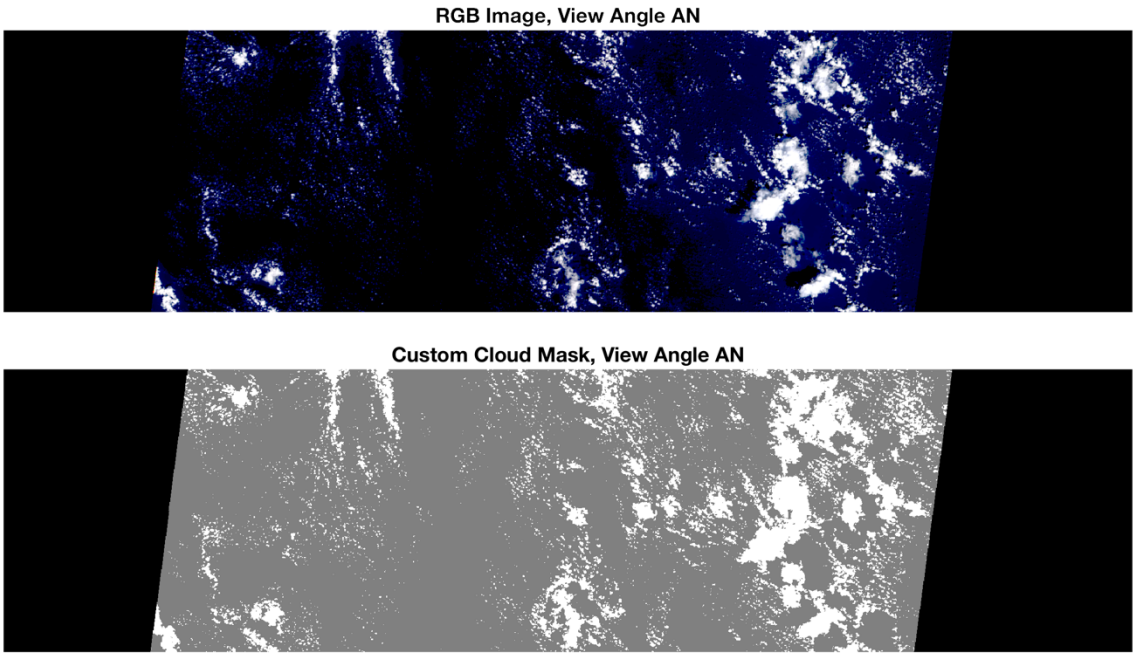

Figure 2.25. Comparison between the RGB image and the custom cloud mask, for the same block as in Figure 2.22. The RGB image has been modified to enhance the cloudy pixels. $T_{RC} = 0.07$ and $T_{WD} = 0.24$. For the cuscom cloud mask, the white pixels indicate cloudy, the gray pixels clear, and the black pixels no retrieval.

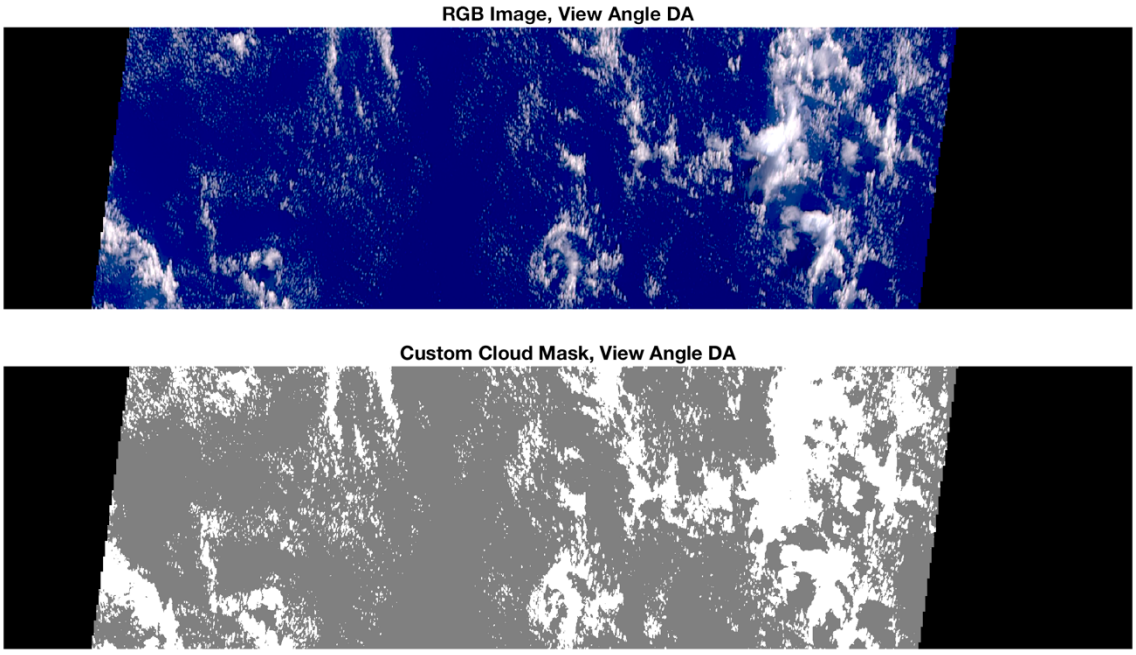

Figure 2.26. Comparison between the RGB image and the custom cloud mask, for Orbit 36649, Block 83, and view angle DA. $T_{RC} = 0.07$ and $T_{WD} = 0.24$.

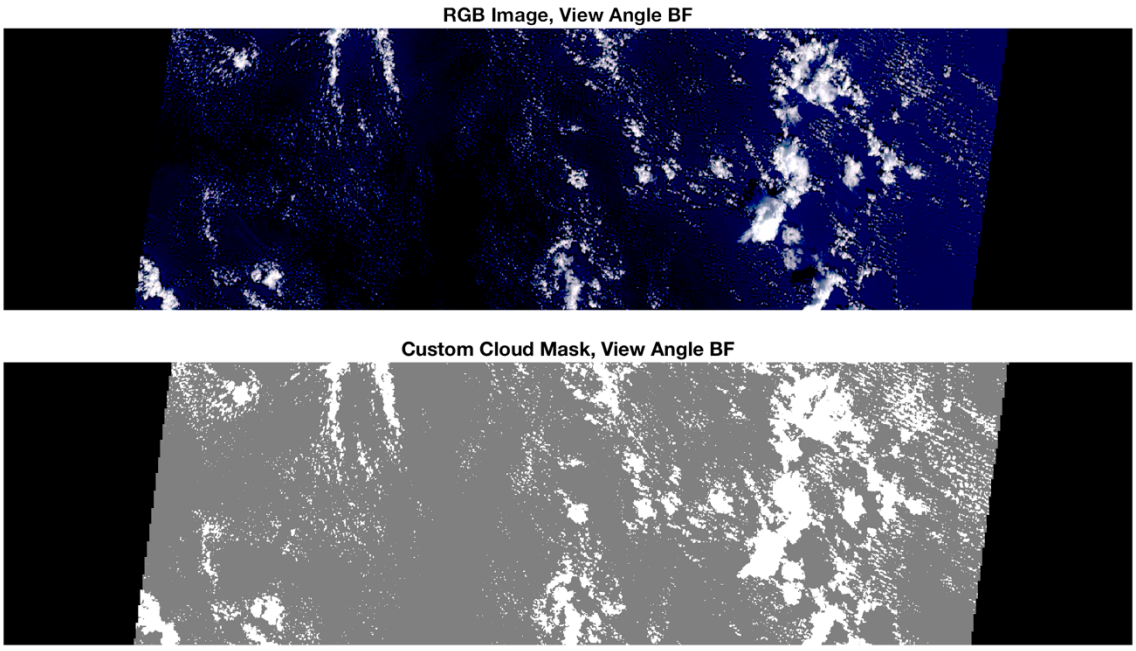

Figure 2.27. Comparison between the RGB image and the custom cloud mask, for Orbit 36649, Block 83, and view angle BF. $T_{RC} = 0.07$ and $T_{WD} = 0.24$.

Since the threshold values in both methods were chosen by how accurate the consequent cloud mask looks to the human eye in comparison to the RGB image, no other validation was performed to analyze the errors and uncertainties of the final custom cloud masks. More in-depth discussions on this point can be found in the papers by Zhao & Di Girolamo (2006, 2007), Di Girolamo & Davies (1997), and Wielicki & Parker (1992).

2.7. Reconstruction from MISR: Wind Correction

The reconstruction requires that all view-angle images involved are looking at the same scene at the same time. However, the approximately 7-minute difference between the DF scene and the DA scene leads to possibly very significant cloud motion and displacement between the

different view-angle images. Consequently, there arises the need for wind correction, in which the cloud displacement during the time interval between the image's time and the reference time of the reconstruction is taken into account.

The MISR Level 2 TOA/Cloud Height and Motion Parameters (TC_CLOUD) contain the parameters for wind in the directions of the local north and the local east for each pixel, and the cloud top heights derived from a stereo-matching algorithm (Mueller et al., 2013). Since the TC_CLOUD variables are all reported at the reference time of AN (the nadir view angle), and because the maximum time difference between view angles is minimized when AN is the reference time as opposed to others (less than 4 minutes), all wind corrections and therefore reconstructions in this project were performed with reference to the time of AN of each block.

The wind correction poses a big challenge. The reported wind values (cloud motion parameters) only concern the supposed cloud top of each pixel at the time of AN, so it is difficult to infer the overall wind field throughout the scene at different altitude levels. This means that there is no information regarding the wind at the times of other view angles, where the pixels of the same geolocations are looking through different portions of the atmosphere and different parts of the observed cloud. Hence, the reported wind at AN cannot simply be superimposed as the wind field on the other view-angle images.

With the above constraint in mind, a method named cloud thickening has been devised in this project. First, the greatest wind value is found from among the reported wind values in the block. Then, regardless of the direction of the wind, its quantity (speed) is used to "thicken" in all directions every cloudy pixel in the block. The level of thickness is determined by the time difference between the view angle and the AN, multiplied by the chosen maximum wind speed.

Hence, more cloud thickening is applied to more oblique view angle. The thickness is used to calculate the thickness addition number, which is the number of pixels (or the grid number) by which the values of all pixels within the distance from each cloudy pixel are replaced by the reference pixel's value. In other words, if P_{i_0,j_0} is the cloudy pixel, then for every other pixel in the block, $P_{i,j}$, $P_{i,j} = P_{i_0,j_0}$ if its index numbers, i and j, satisfy $(i - i_0)^2 + (j - j_0)^2 \leq (N_{TA} + 0.5)^2$, where $N_{TA} = round_{up}\left(\frac{|V| \cdot \Delta T}{R_P}\right)$ is the thickness addition number, V the reported wind with the block's highest speed, ΔT the time difference between the view angle and the AN, and R_P the pixel resolution.

This method operates on the assumption that the greatest wind reported is the greatest wind in the entire scene, along the horizontal and vertical dimensions, and throughout the time interval between different view angles. In the case of the RCCM, the cloud thickening is applied in the order of low-confidence clear, low-confidence cloud, and high-confidence cloud.

The basic idea behind this method is that all pixels in non-nadir view angle images that are potentially cloudy at the time of AN are made to be cloudy. This method works in principle, since the general principle of the reconstruction, by its nature, tolerates the thickening of cloudy pixels. It assumes that the cloud should have been seen by all view angles, and takes as cloudy only the parts of the reconstruction domain that overlap in all view angles, so the thickened cloudy pixels can be simply considered as the candidates for the cloud's location at the time of AN. Figures 2.28 and 2.29 show examples of cloud-thickened an RCCM and a custom cloud mask.

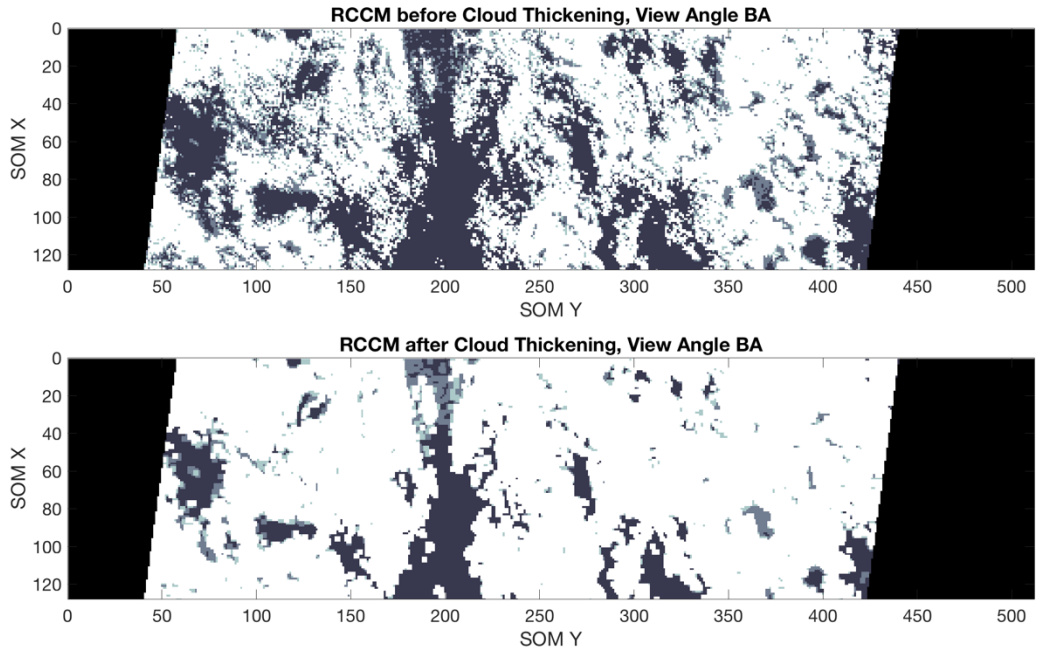

Figure 2.28. Comparison between the RCCM before and after cloud thickening, Orbit 36649, Block 83, and view angle BA.

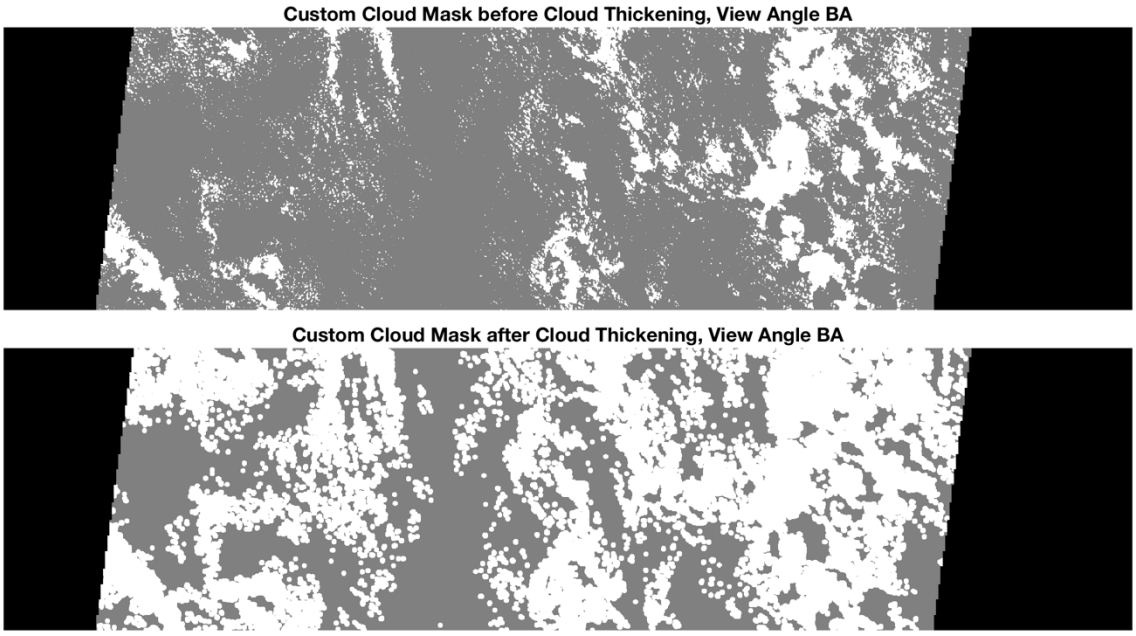

Figure 2.29. Comparison between the custom cloud mask before and after cloud thickening, Orbit 36649, Block 83, and view angle BA.

The cloud-thickening method still contributes to the uncertainty of the reconstruction outcomes, as the gross overestimation of the cloud is inevitable. Therefore, the results shown in Chapter 3 display the reconstruction outcomes both with and without the wind correction.

2.8. Reconstruction from MISR: Ray Casting

The cloud volume reconstruction in this project involves casting rays from the reported geolocations of each cloudy pixel through the pre-determined cloud domain, according to the reported viewing zenith and azimuth values. What follows then is the need for the methods for the ray casting. Two ray casting methods were devised and used: the distance threshold (DTH) and the voxel boundary intersections (VBI).

The DTH method works as follows. Throughout the pre-determined cloud volume on the ellipsoid, represented by the black dotted boxes on the green curve in Figure 2.30, the rays are cast only from cloudy pixels, represented by white line segments over the green curve. Each ray is defined as a 3-D straight line, with the reported GeoLatitude and GeoLongitude values of the pixel as the starting point, and the reported viewing zenith and azimuth angles as the direction vector. If the distance between the central point of a voxel and the cast ray is within a threshold value, the voxel is determined cloudy. In other words, if $L(t) = (x_0, y_0, z_0) + t(u, v, w)$ is the vector equation of the cast ray where (x_0, y_0, z_0) is the 3-D Cartesian coordinates of the pixel's geolocation, (u, v, w) the ray vector, and (x_1, y_1, z_1) the Cartesian coordinates of the voxel center, than the voxel is determined cloudy if $d^2 \leq d_T^2$, where d_T^2 is the distance threshold

squared, and d^2 is the distance squared between the ray and the voxel center calculated as $d^2 = (x_0 + tu - x_1)^2 + (y_0 + tv - y_1)^2 + (z_0 + tw - z_1)^2$, where $t = \frac{(x_1 - x_0)u + (y_1 - y_0)v + (z_1 - z_0)w}{u^2 + v^2 + w^2}$.

The process is repeated at all view angles, and only the voxels that have been determined cloudy by all nine angles are eventually determined cloudy. The distance threshold is determined such that it encompasses the distance between the voxel center and the outermost corner of the largest voxel in the reconstruction domain. It turned out to be approximately 800 m for the RCCM at the reconstruction voxel size of 1100x1100x275, and 250 m for the custom cloud mask at the reconstruction voxel size of 275x275x275 m.

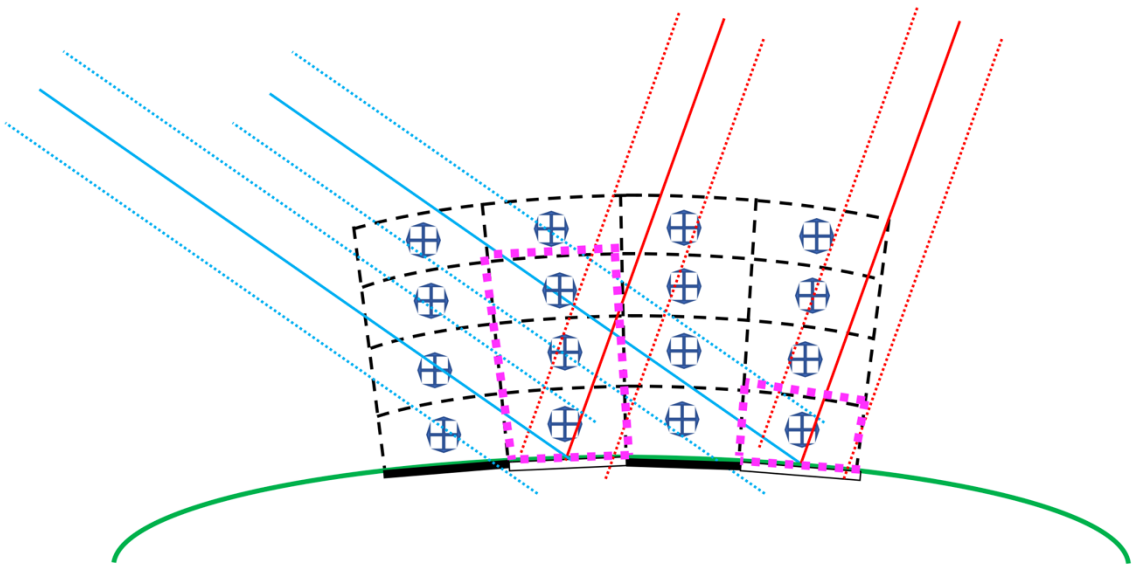

Figure 2.30. A 2-D cross-section diagram depicting the DTH ray casting method. The crosshairs indicate the voxel centers, the red and blue solid lines the cast rays, and the dotted lines the distance threshold. The purple dotted boxes indicate the voxels that are eventually determined cloudy by all view angles (two in this diagram).

The VBI method works as follows. Given the pre-determined cloud domain on the ellipsoid, the voxel boundaries are defined in either a plane of the form $Ax + By + Cz = D$ or

an ellipsoid of the form $\frac{x^2+y^2}{(R_{equator}+E)^2} + \frac{z^2}{(R_{pole}+F)^2} = 1$, where A, B, C, D, E, and F are constants, $R_{equator}$ the equatorial radius of WGS84, and R_{pole} the polar radius (see Section 2.4). Then, the rays are cast from cloudy pixels, and the intersections between the voxel boundaries and the cast rays are found. Then the location of each intersection point is checked with regard to its surrounding voxel boundaries, to find where it lies in relation to the adjacent voxels. If any voxel has an intersection point in its boundary, then it is determined cloudy. The number of cast rays per pixel in one dimension (SOM X or SOM Y axis) is determined by $N_{CR} = round_{down}\left(S_h \cdot \frac{\tan(90°-Z_{max})}{S_v}\right) + 2$, where N_{CR} is the number of cast rays, S_h the horizontal voxel resolution, S_v the vertical voxel resolution, and Z_{max} the maximum viewing zenith value in the block. The addition of 2 at the end is to ensure that there are at least two cast rays per pixel in one dimension and therefore four in total, one at each corner of the pixel. Again, this process is repeated for all view angles, and only the voxels that have been determined cloudy by all nine angles are eventually determined cloudy. Figure 2.31 shows a schematic diagram of the VBI method.

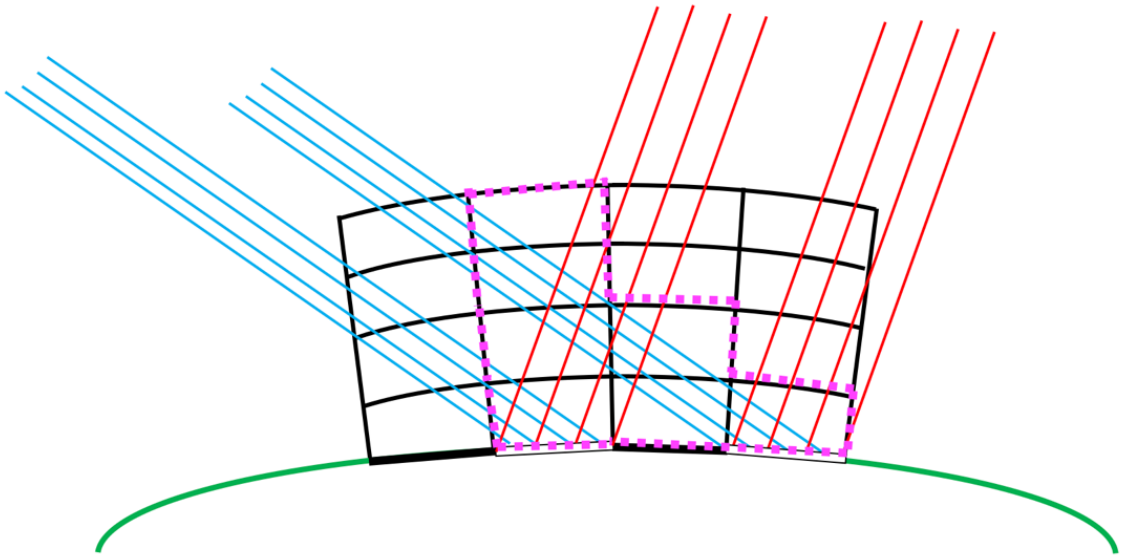

Figure 2.31. A 2-D cross-section diagram depicting the VBI ray casting method. Note the intersecting points between the cast rays in red and blue and the voxel boundaries in black lines or curves. The purple dotted boxes indicate the voxels that are eventually determined cloudy by all view angles (two in this diagram).

The eventual determination of voxel's cloudiness based on all nine view angles in both methods means that the ray casting operates on the principle that, if there is a cloud in the scene, then it must have been observed by all view angle cameras.

After all nine view angles are considered and the eventual cloud volume is produced, the cloud top height is applied to reduce the overestimation at the top of the reconstructed cloud. This is done by casting rays from the AN cloud mask, and checking either their distances from the voxel centers or their boundary intersections only for the voxels as high as or below the cloud top height corresponding to the pixel from which the rays are cast. Then, only the voxels that remain cloudy under this constraint are eventually determined cloudy, to yield the final reconstructed volume.

Both the VBI and the DTH methods yield very similar results, but VBI tends to show greater overestimation, which will be shown in Chapter 3. This is due to the fact that the VBI

method casts more than one ray per pixel and also from the corner of the pixel's rectangular GIFOV, while the DTH cast only one ray per pixel from the center of the GIFOV. The DTH method was developed after the VBI method's code had turned out to take too much runtime. While the VBI method strictly concerns the voxel boundaries surrounding its shape of bent cuboid, the DTH method directly concerns the distance between the pixel's line of sight and the voxel. Hence, the DTH method can be considered to be more intuitive in a physical and computer-vision sense.

Figure 2.32 shows the example reconstructed ray-track cloud volumes, the cloud volume with all view angles, and the same volume with the cloud top height applied.

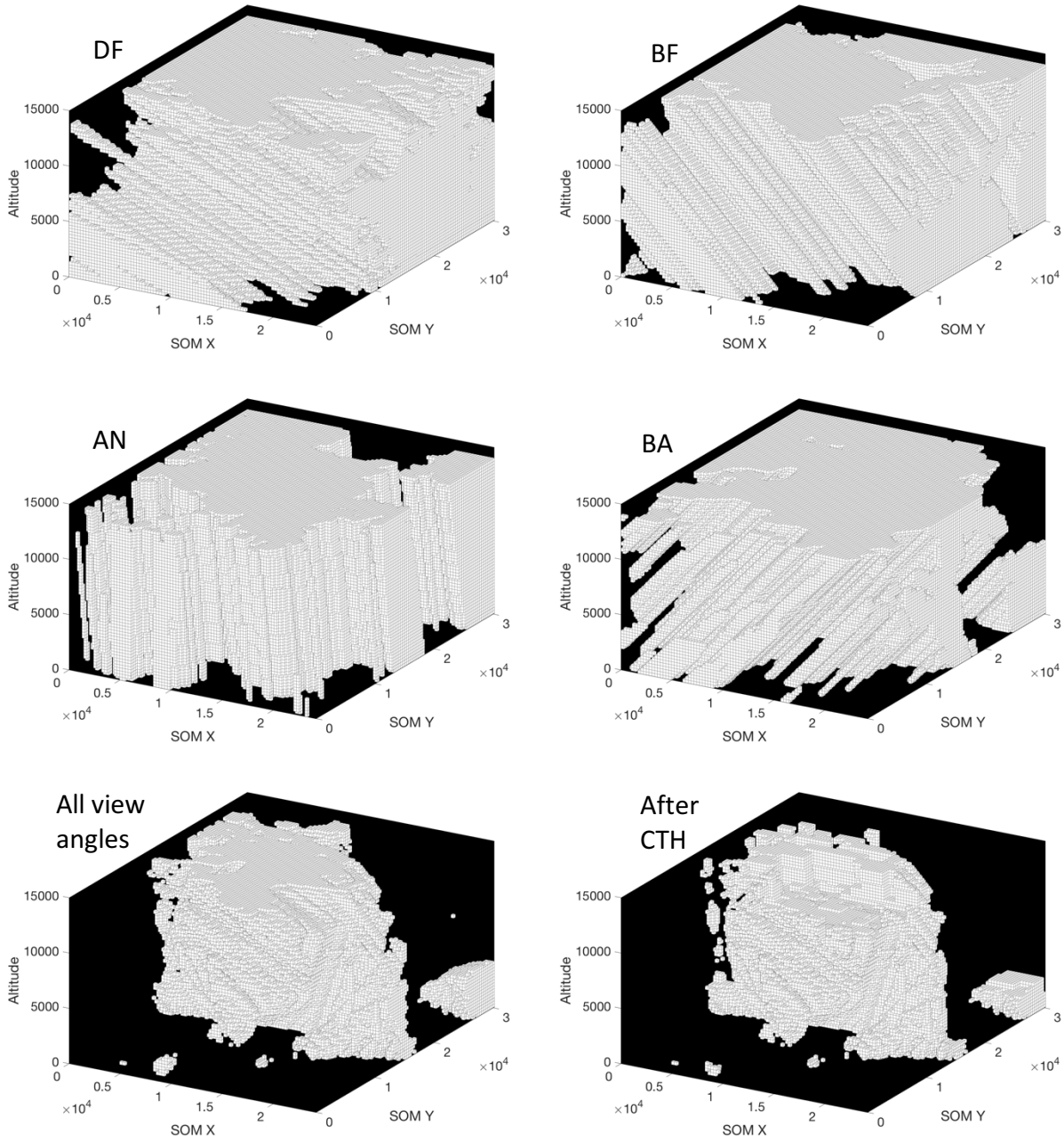

Figure 2.32. The intermediate reconstructed cloud volumes at the corresponding view angles, the volume after all nine view angles are considered, and the volume after the cloud top height is applied, for a selected region in Orbit 36649, Block 83, constructed under the DTH ray casting method, from the custom cloud masks, without wind correction. Each intermediate cloud volume exhibits the pattern of the direction of its cast rays.

Chapter 3. Results

3.1. Overview

The results presented in this chapter come from scenes that are carefully hand-picked and show a good vertical development of clouds favorable for the multi-angle volume reconstruction from MISR data. For each scene chosen, a total of eight types of results are shown as follows.

- Input: RCCM. Wind correction: on. Ray casting method: DTH
- Input: RCCM. Wind correction: on. Ray casting method: VBI
- Input: RCCM. Wind correction: off. Ray casting method: DTH
- Input: RCCM. Wind correction: off. Ray casting method: VBI
- Input: custom cloud mask. Wind correction: on. Ray casting method: DTH
- Input: custom cloud mask. Wind correction: on. Ray casting method: VBI
- Input: custom cloud mask. Wind correction: off. Ray casting method: DTH
- Input: custom cloud mask. Wind correction: off. Ray casting method: VBI

All the reconstruction results from the RCCM inputs have the voxel size 1100x1100x275 m, and all the results from the custom cloud masks have the voxel size 275x275x275 m. In the reconstructions from the RCCM images, the level of high-confidence cloud was set to be cloudy

and all other levels to be clear, i.e. rays are cast only from pixels classified as high-confidence cloud. All the cloud volumes are 3-D plotted with rectangular cuboid voxels, but in reality each voxel represents the slightly bent cuboid described in Section 2.4. The maximum possible height in the reconstructed volume was set to be 1 km above the reported cloud top height, to allow for more room for the reconstruction at the top of the cloud.

3.2. Orbit 36649 Block 83

This section displays the reconstruction results for the selected local region (shown in red boxes in Figure 3.1) in Block 83 of Orbit 36649. It is over the Pacific Ocean north of Papua New Guinea and Guam, observed on November 8, 2006 UTC. Figures 3.2 and 3.3 show the ray casting domain around the selected reconstruction region, whose dimensions were determined to include the pixels whose cast rays travel through the reconstruction domain of the selected region (see Appendices A.3 and B for more detail). In all 2-D images, SOM X axis extends downward, and SOM Y axis extends rightward. Figures 3.4 to 3.7 show the reconstruction results in both DTH and VBI methods, with and without the wind correction (cloud thickening), from the RCCM and the custom cloud masks. Table 3.1 shows the numerical results of the reconstructions.

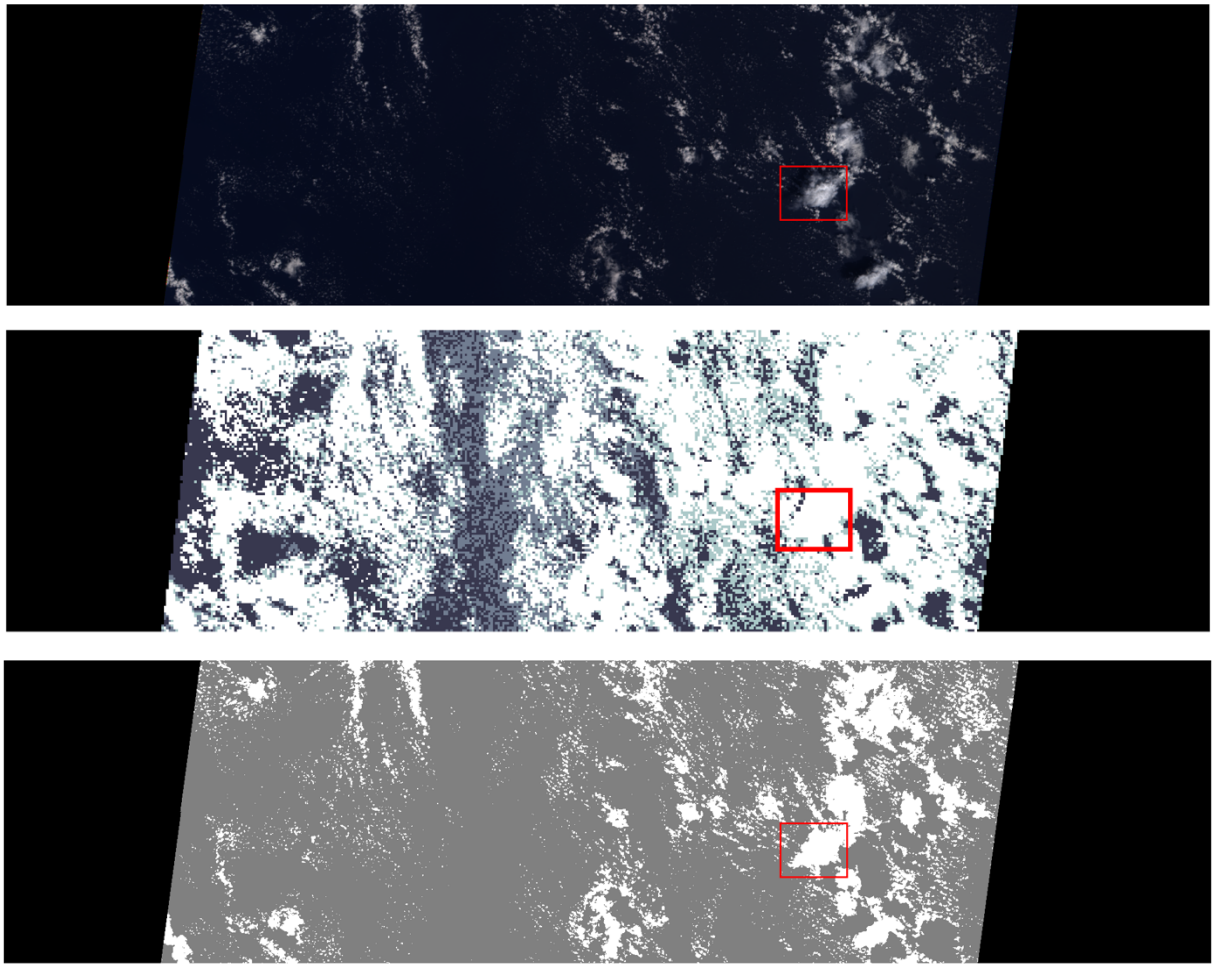

Figure 3.1. The RGB image, the RCCM, and the custom cloud mask of the entire block, for view angle AN. The region selected for the reconstruction is indicated in the red boxes.

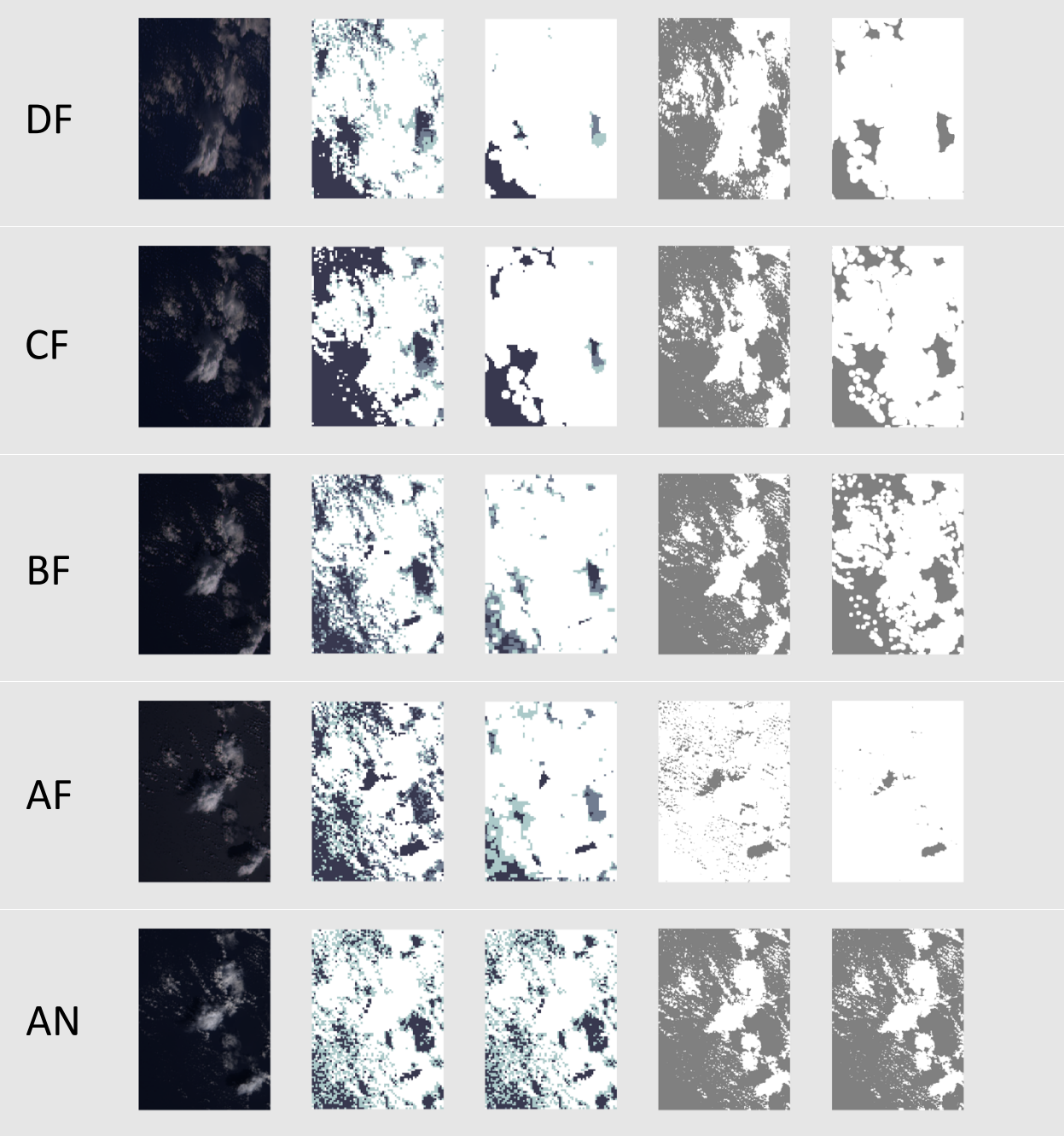

Figure 3.2. From left to right: the RGB image, the RCCM, the RCCM after the wind correction (cloud thickening), the custom cloud mask, and the custom cloud mask after the wind correction, of the selected region and its surroundings. From top to bottom: view angle DF, CF, BF, AF, and AN. In the AA custom cloud masks, the excessive cloudy pixels are due to the sun glint that causes many non-cloudy pixels to have brightness close to cloudy pixels. For AN, since the reference time for wind correction is the time of AN, the images are the same between wind correction on and off. For the custom cloud masks, $T_{RC} = 0.07$ and $T_{WD} = 0.24$ for all view angles (see Section 2.6).

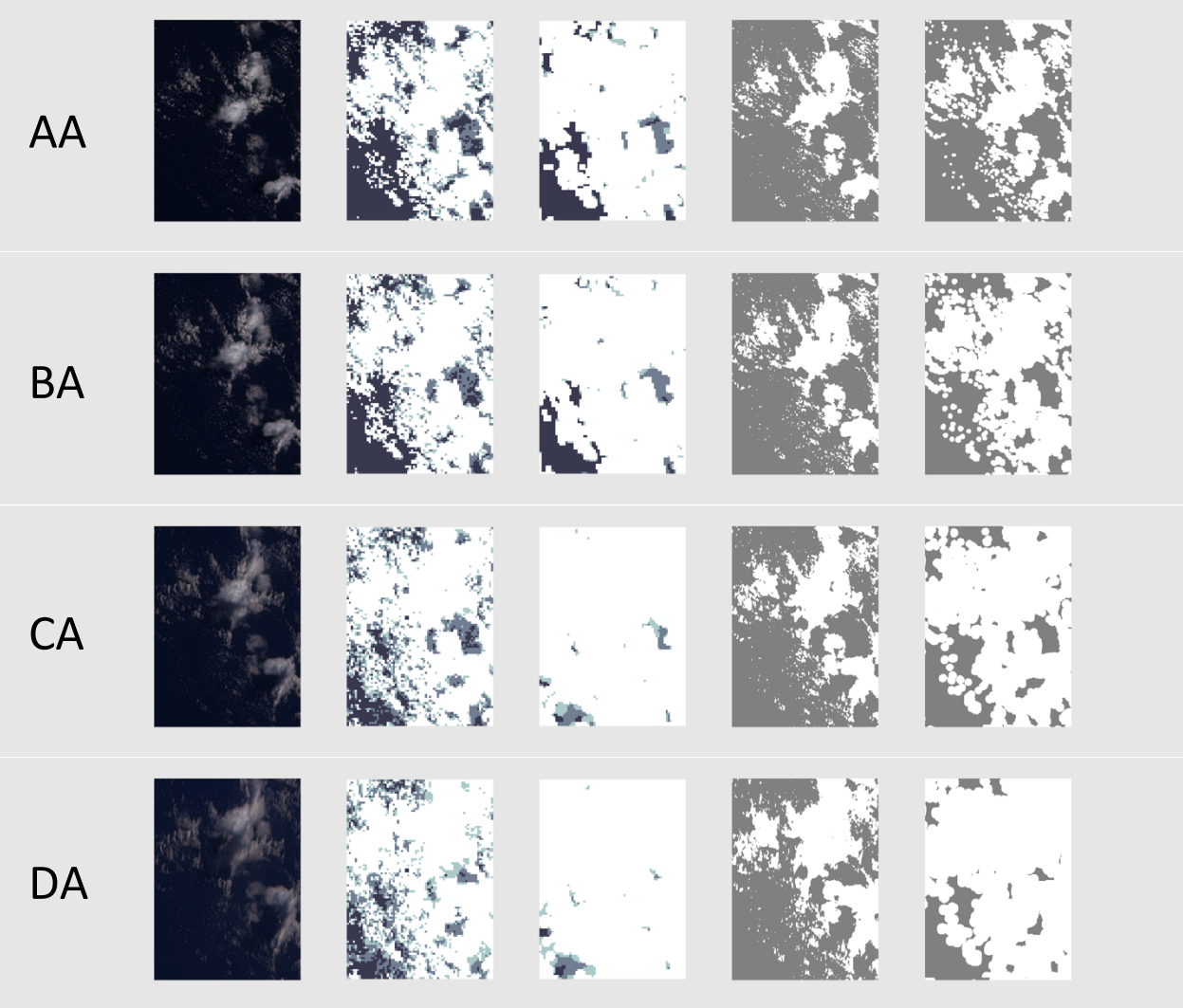

Figure 3.3. Same as Figure 3.2, but for view angles AA, BA, CA, and DA, from top to bottom.

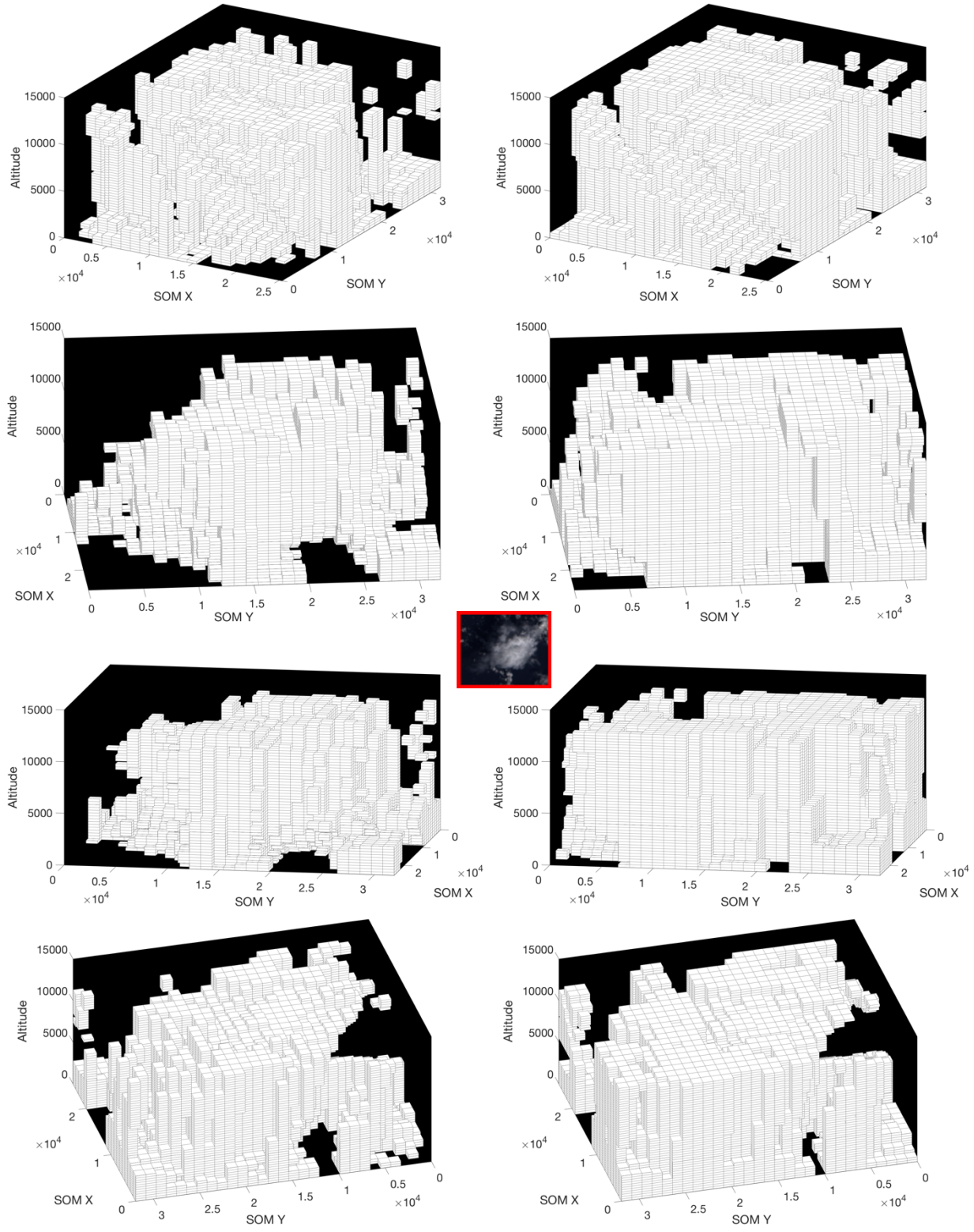

Figure 3.4. The reconstruction results from the RCCM inputs, with wind correction, under the DTH (left column) and the VBI (right column) ray casting methods, at various views (same view for each row). The units are all in m. The red box at the center is the overhead (nadir) RGB image of the reconstruction region.

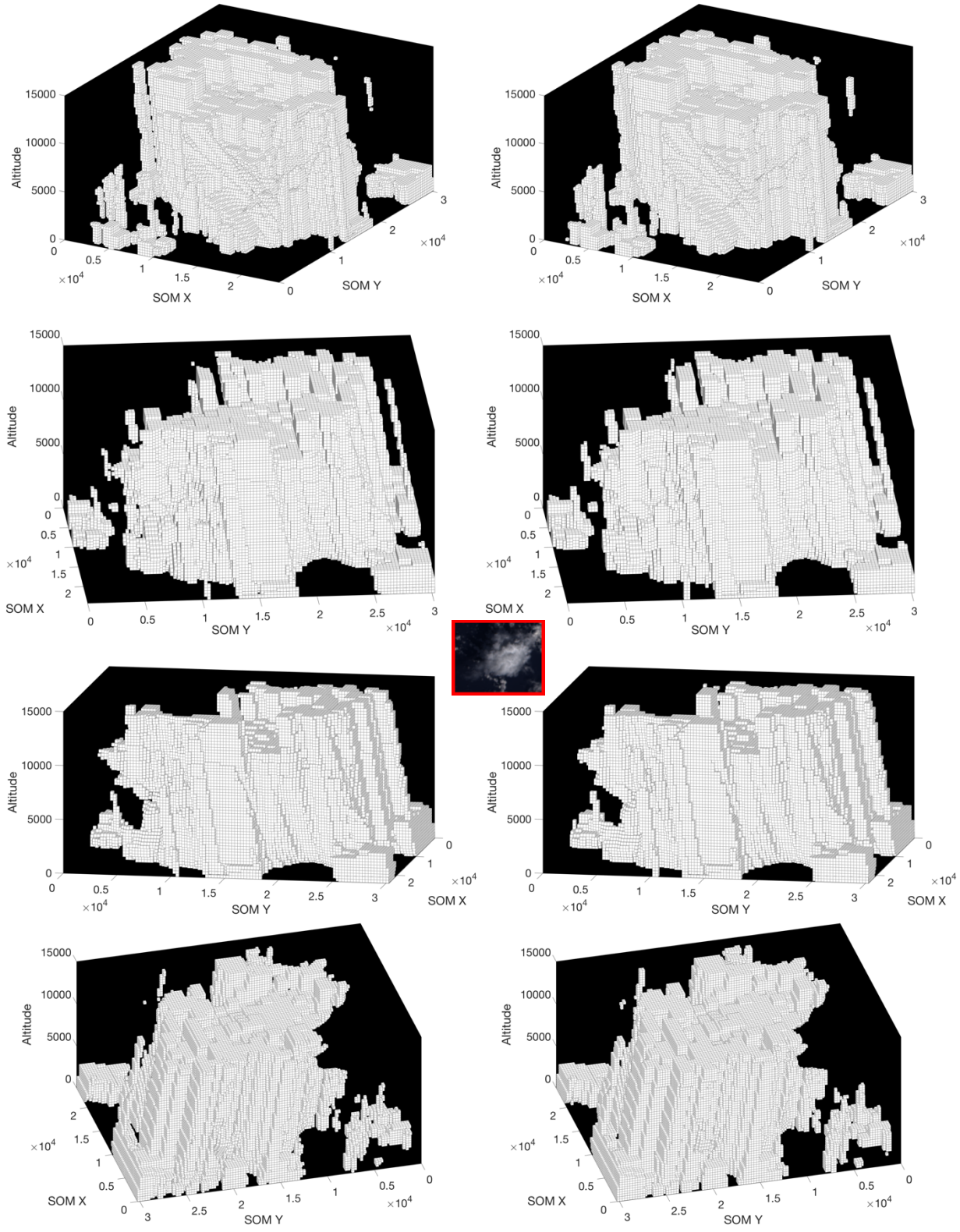

Figure 3.5. Same as Figure 3.4, but from the custom cloud mask inputs with wind correction.

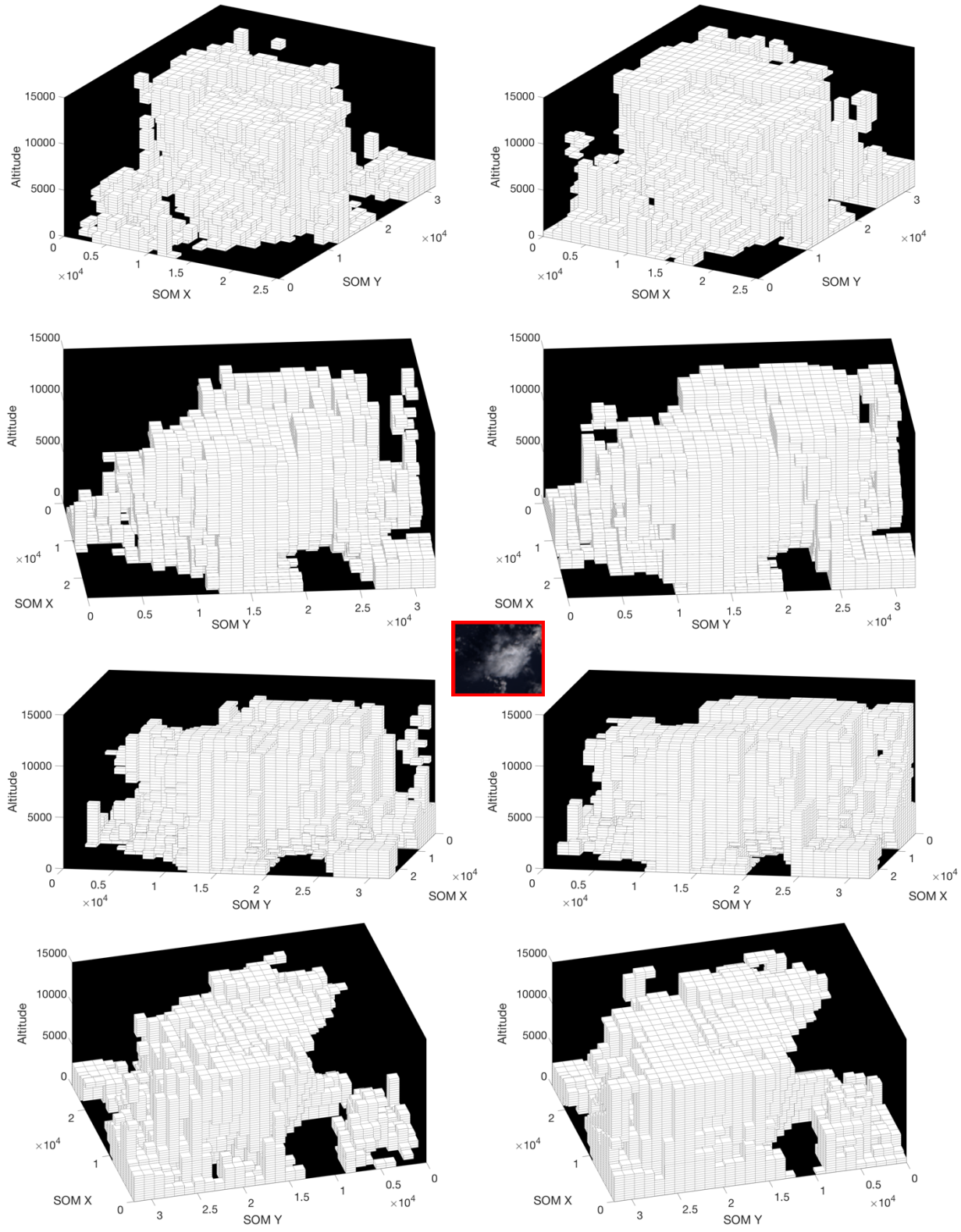

Figure 3.6. Same as Figure 3.4, but from the RCCM inputs without wind correction.

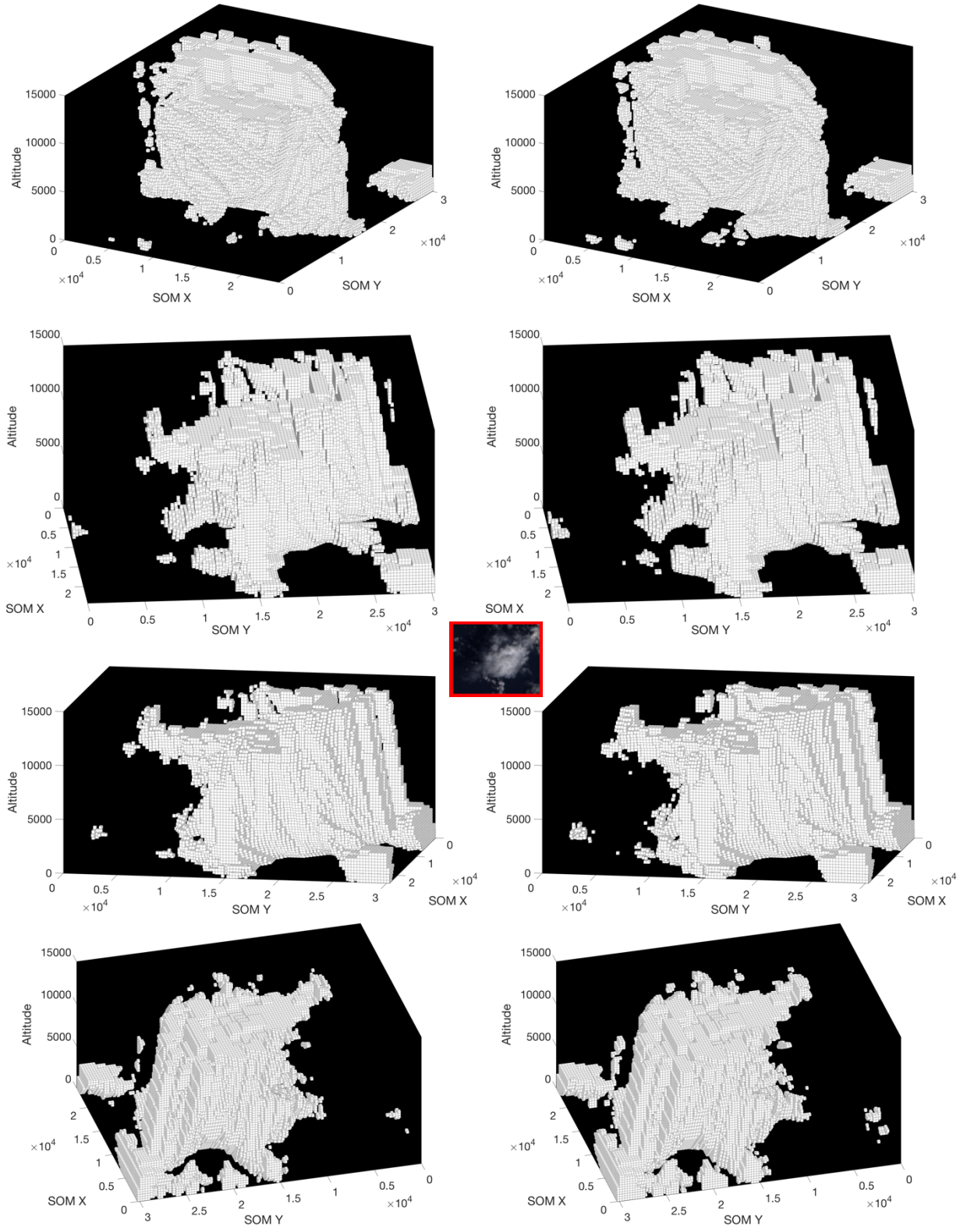

Figure 3.7. Same as Figure 3.4, but from the custom cloud mask inputs without wind correction.

Table 3.1. Comparison in reconstructed cloud volume between the eight different cases specified in Section 3.1. To simplify the volume calculations, each voxel is assumed to be a rectangular cuboid. The entries are in cubic meters.

Cloud Mask	**RCCM**		**Custom Cloud Mask**	
Ray Casting Method	**DTH**	**VBI**	**DTH**	**VBI**
Wind Correction	5.2641×10^{12}	6.6620×10^{12}	3.5648×10^{12}	3.8390×10^{12}
No Wind Correction	3.9734×10^{12}	5.2578×10^{12}	2.2146×10^{12}	2.4604×10^{12}

Several tendencies are seen in Table 3.1. The VBI results tend to overestimate the cloud volume relative to the DTH results. This is because while only one ray is cast per pixel from its center during the DTH ray casting, multiple rays are cast from the GIFOV of the pixel during the VBI ray casting. The RCCM results tend to overestimate more than the custom cloud mask results, and this could be explained as the resolution effect within the cloud masks, where the greater ratio between the pixel resolution and the cloud size leads to greater overestimation of the cloud. The results with wind correction (cloud thickening) tend to overestimate more than the results without wind correction, as anticipated in Section 2.7. These tendencies are observed in other reconstruction results as well, which are shown in the following sections.

3.3. Orbit 19726 Block 86

This section displays the reconstruction results for the selected local region (shown in red boxes in Figure 3.8) in Block 86 of Orbit 19726. It is over the Pacific Ocean significantly north of New Zealand near the Equator, observed on September 2, 2003 UTC. This is the same scene as in the paper by Seiz & Davies (2006). Figures 3.9 and 3.10 show the ray casting domain around the

selected reconstruction region, whose dimensions were determined to include the pixels whose cast rays travel through the reconstruction domain of the selected region. In all 2-D images, SOM X axis extends downward, and SOM Y axis extends rightward. Figures 3.11 to 3.14 show the reconstruction results in both DTH and VBI methods, with and without the wind correction (cloud thickening), from the RCCM and the custom cloud masks. Table 3.2 shows the numerical results of the reconstructions.

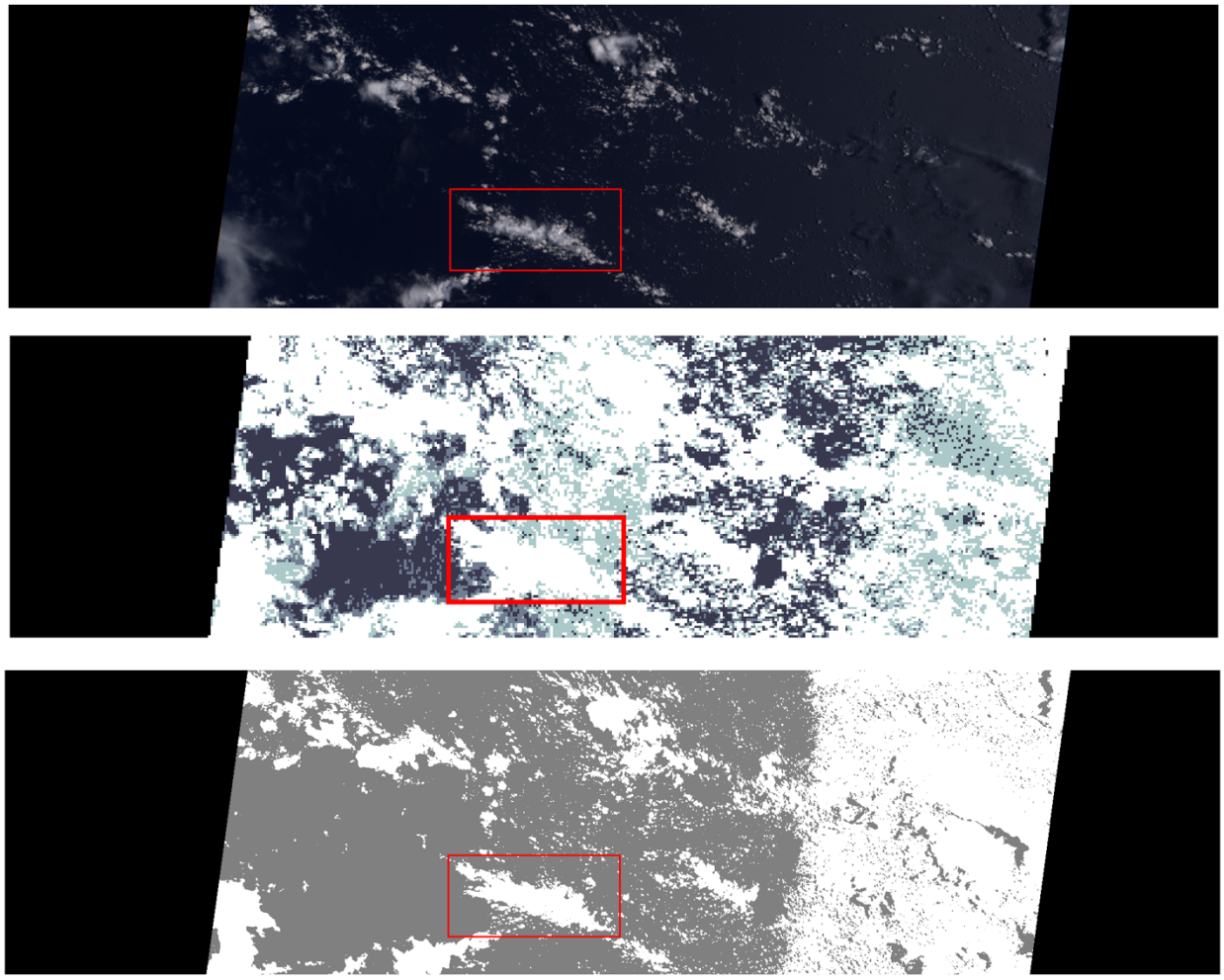

Figure 3.8. The RGB image, the RCCM, and the custom cloud mask of the entire block, for view angle AN. The region selected for the reconstruction is indicated in the red boxes. The effect of sun glint is vivid in the custom cloud mask.

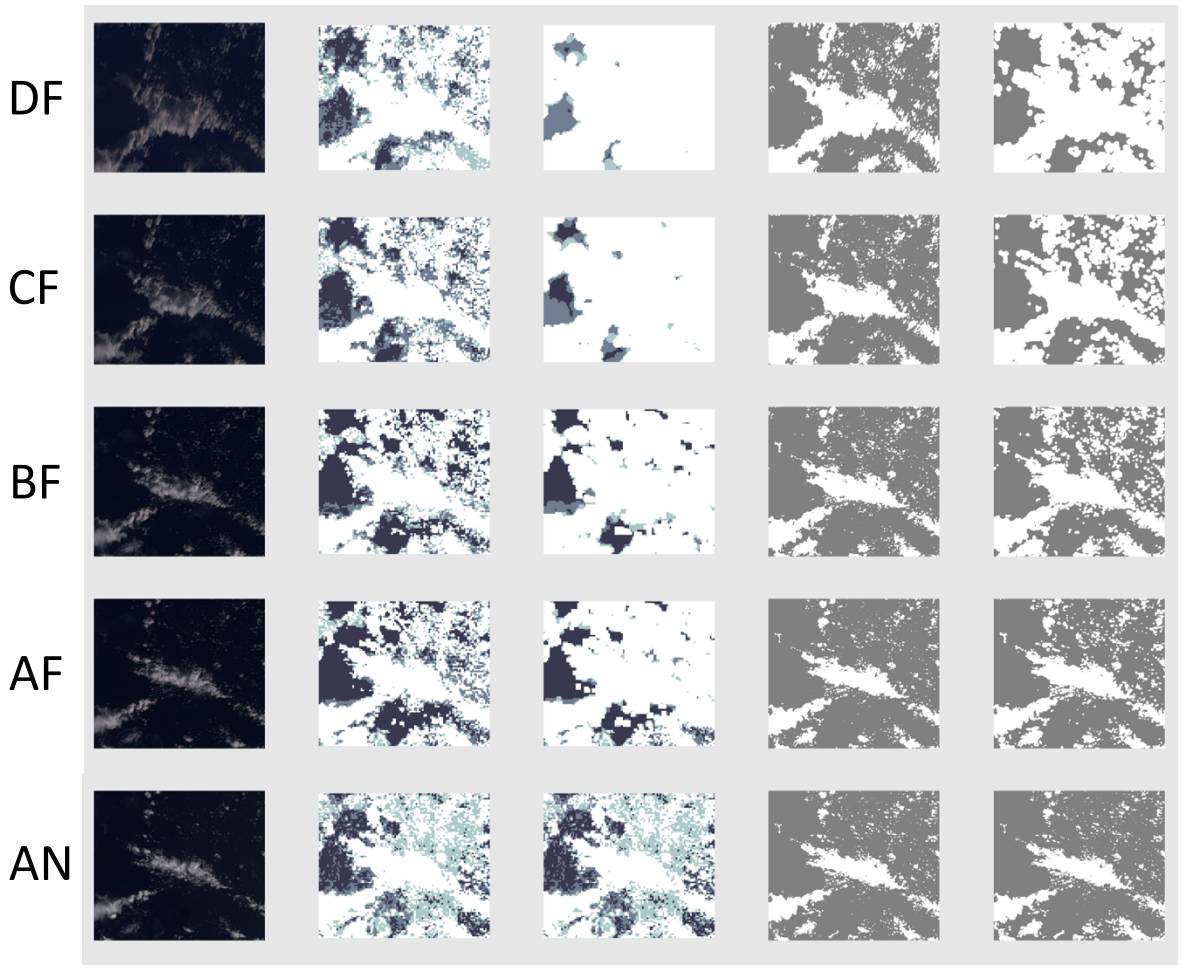

Figure 3.9. From left to right: the RGB image, the RCCM, the RCCM after the wind correction (cloud thickening), the custom cloud mask, and the custom cloud mask after the wind correction, of the selected region. From top to bottom: view angle DF, CF, BF, AF, and AN. For the custom cloud masks, $T_{RC} = 0.07$ and $T_{WD} = 0.24$ for all view angles.

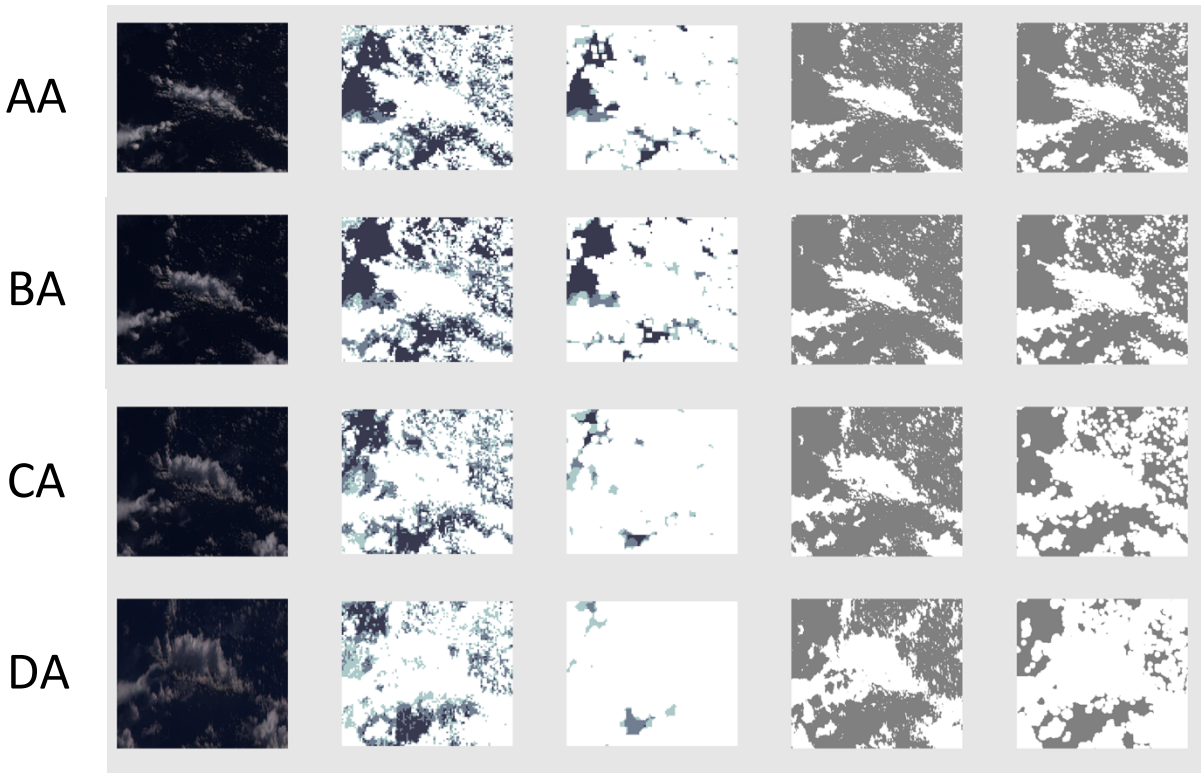

Figure 3.10. Same as Figure 3.9, but for view angles AA, BA, CA, and DA, from top to bottom.

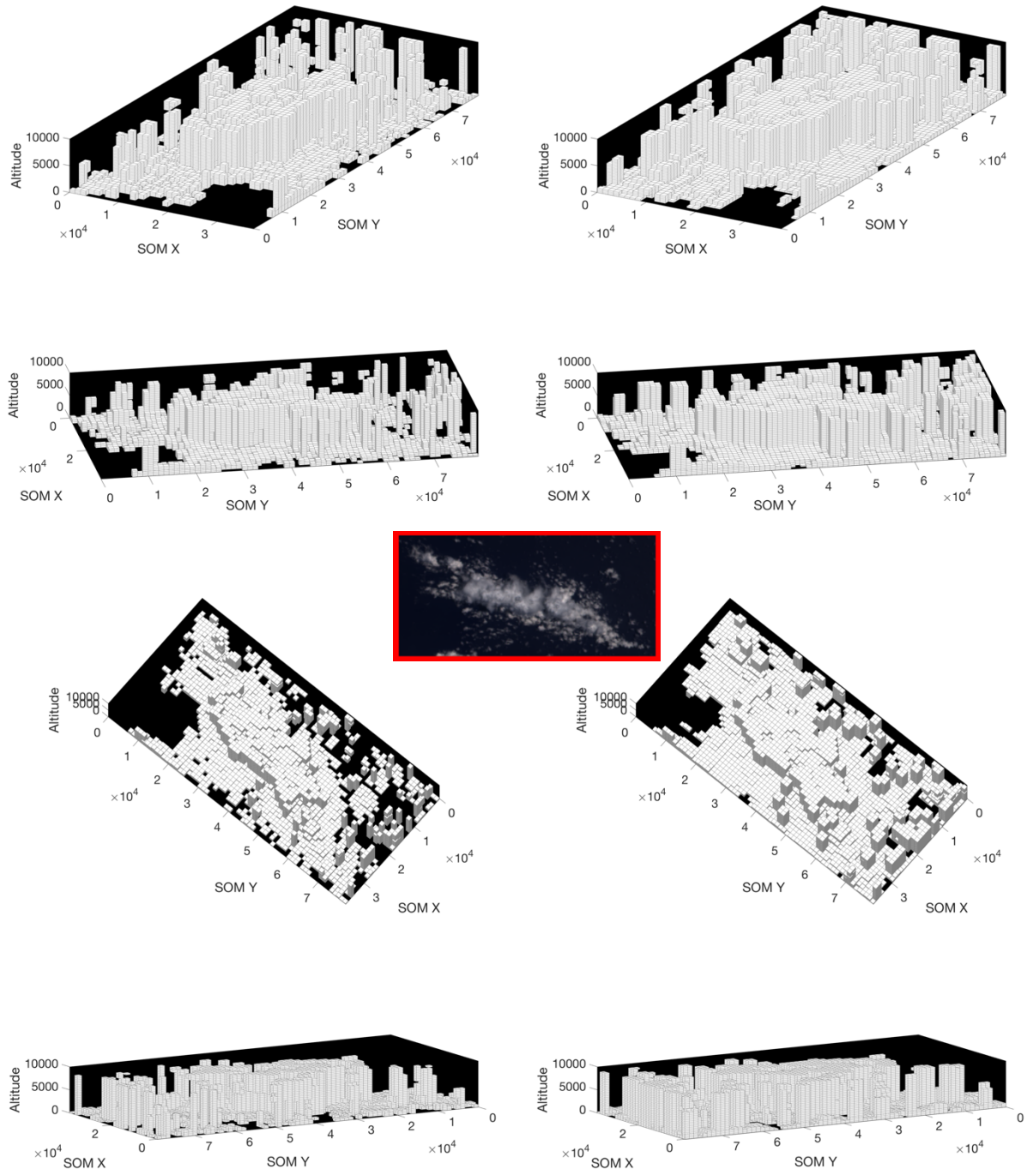

Figure 3.11. The reconstruction results from the RCCM inputs, with wind correction, under the DTH (left column) and the VBI (right column) ray casting methods, at various views (same view for each row). The units are all in m. The red box at the center is the overhead (nadir) RGB image of the reconstruction region.

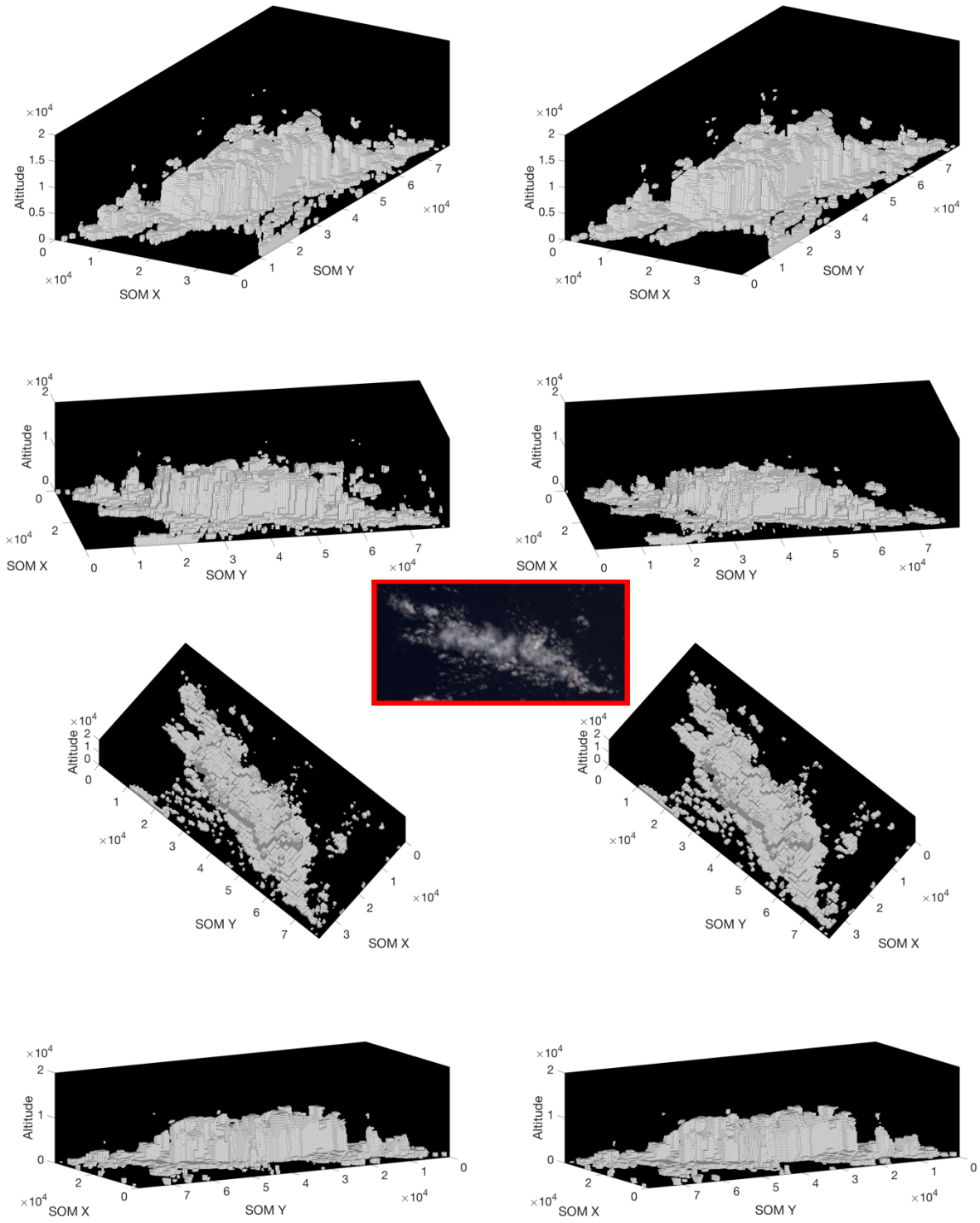

Figure 3.12. Same as Figure 3.11, but from the custom cloud mask inputs with wind correction.

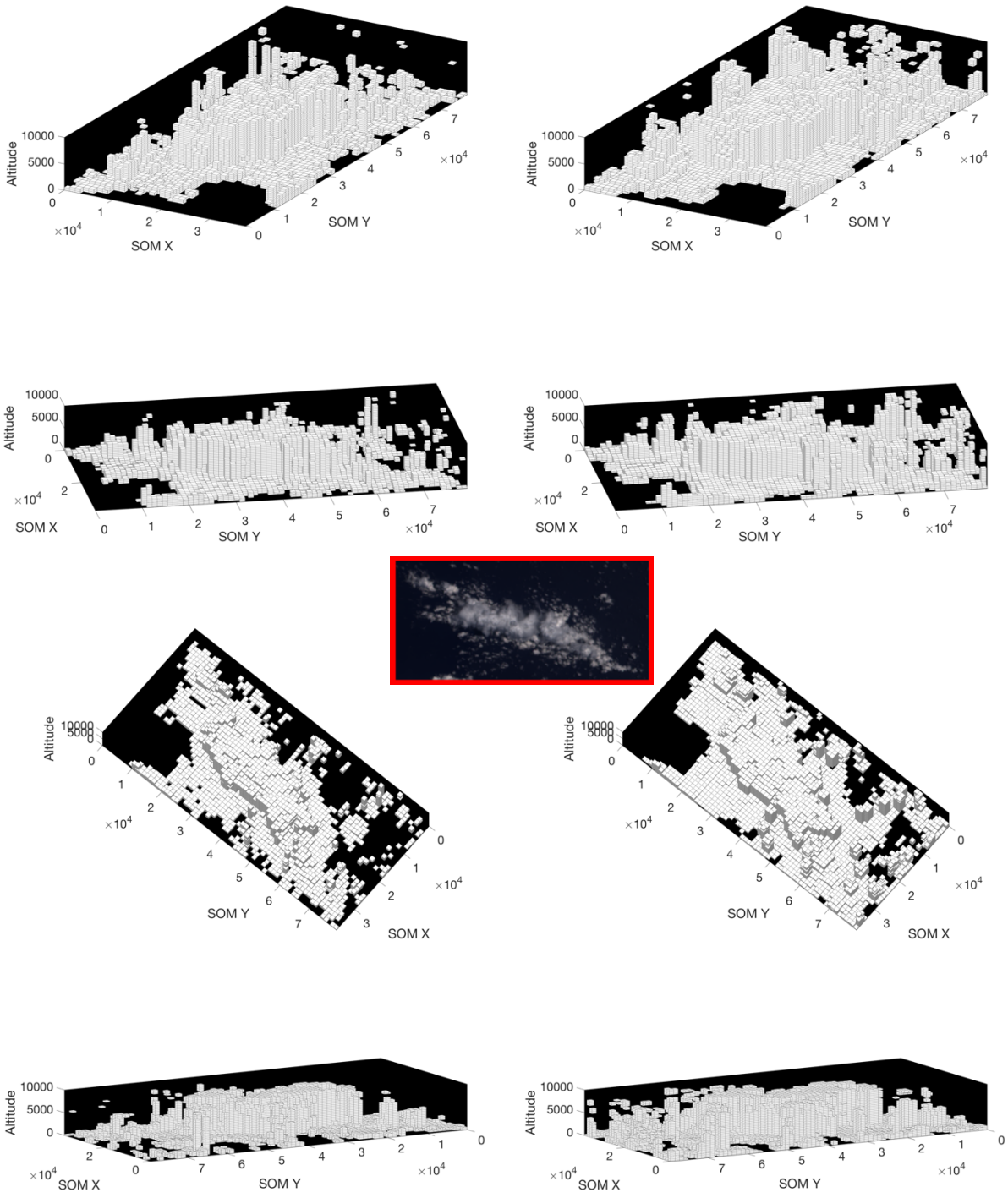

Figure 3.13. Same as Figure 3.11, but from the RCCM inputs without wind correction.

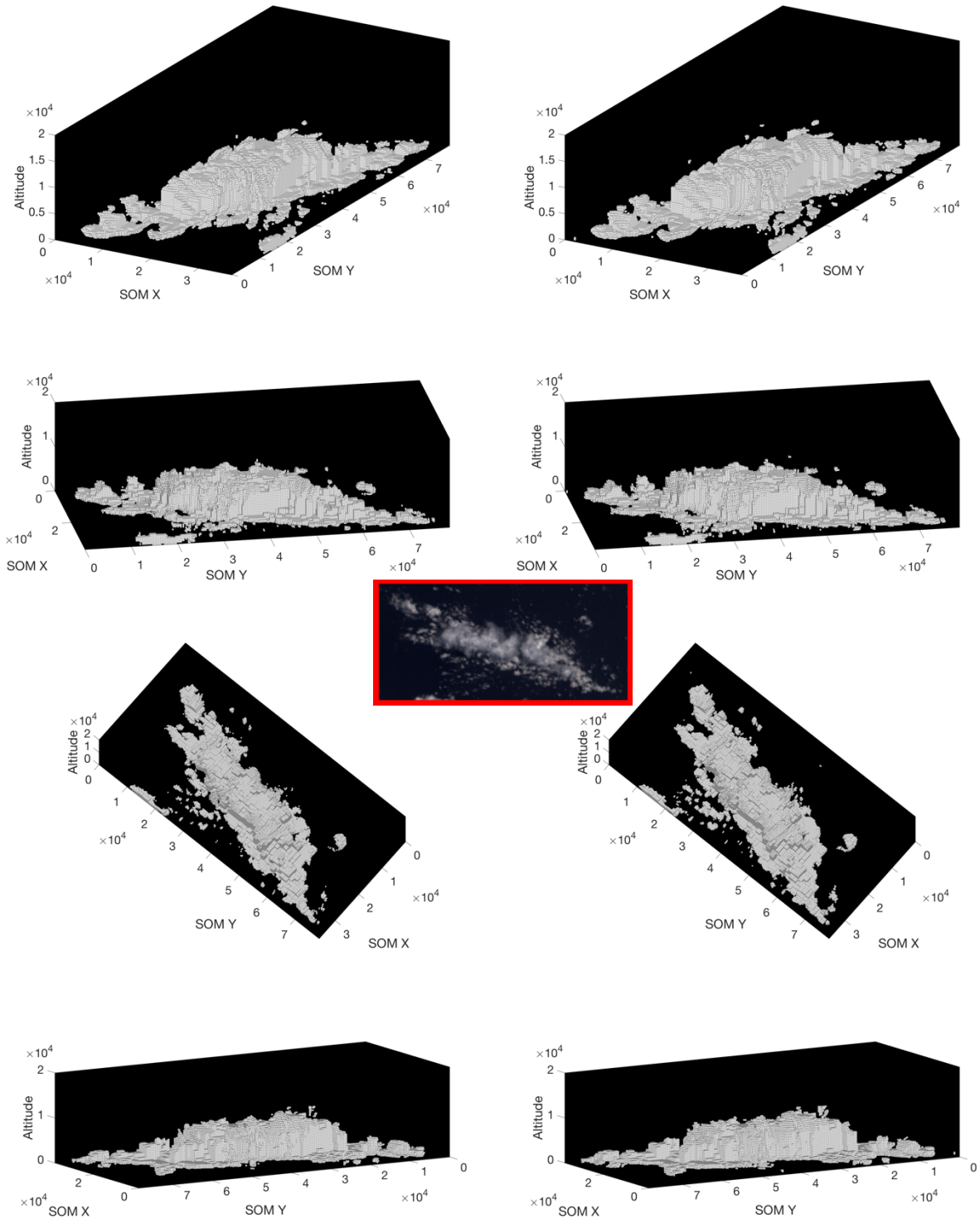

Figure 3.14. Same as Figure 3.11, but from the custom cloud mask inputs without wind correction.

Table 3.2. Comparison in reconstructed cloud volume between the eight different cases specified in Section 3.1. To simplify the volume calculations, each voxel is assumed to be a rectangular cuboid. The entries are in cubic meters.

Cloud Mask	RCCM		Custom Cloud Mask	
Ray Casting Method	DTH	VBI	DTH	VBI
Wind Correction	5.9462×10^{12}	8.8245×10^{12}	3.8291×10^{12}	4.1684×10^{12}
No Wind Correction	4.9806×10^{12}	7.0793×10^{12}	3.1194×10^{12}	3.4121×10^{12}

The same tendencies as in Table 3.1 are observed in Table 3.2. The VBI results tend to overestimate the cloud volume relative to the DTH results. The RCCM results tend to overestimate more than the custom cloud mask results. The results with wind correction (cloud thickening) tend to overestimate more than the results without wind correction. In comparison to the result shown by Seiz & Davies (2006), the reconstruction appears thicker in general, as shown in Figures 3.15.

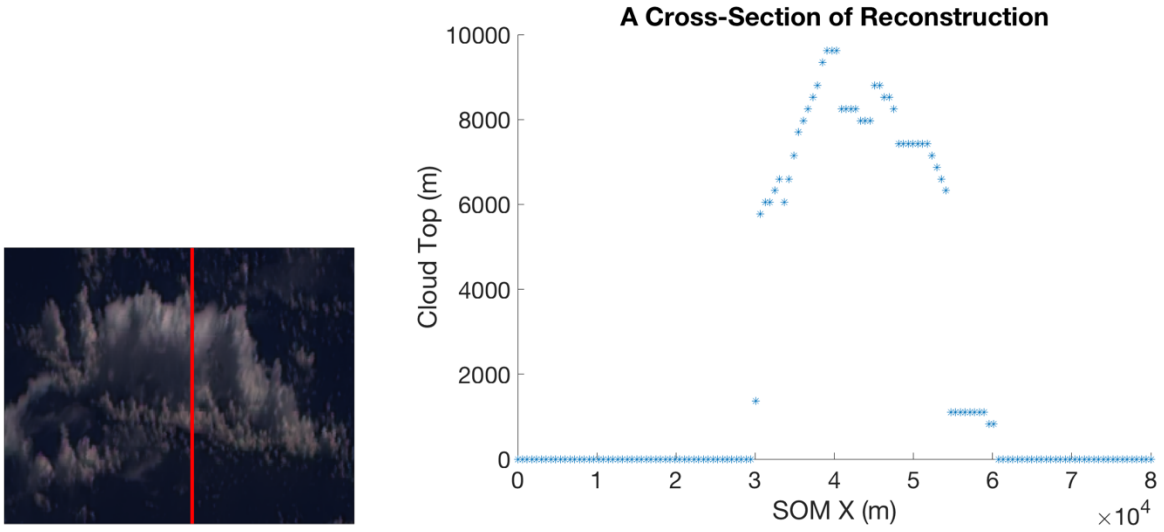

Figure 3.15. A cross-section (shown as the red line in the RGB image of view angle DA) of the reconstructed cloud volume from the custom cloud mask, through the DTH method, without wind correction (as in Figure 3.14). The plot on the right is in the same scale as the plot in Figure 1.15.

3.4. Orbit 01181 Block 91

This section displays the reconstruction results for the selected local region (shown in red boxes in Figure 3.16) in Block 91 of Orbit 01181. It is over the Atlantic Ocean south of West Africa, observed on March 8, 2000 UTC. Figures 3.17 and 3.18 show the ray casting domain around the selected reconstruction region, whose dimensions were determined to include the pixels whose cast rays travel through the reconstruction domain of the selected region. In all 2-D images, SOM X axis extends downward, and SOM Y axis extends rightward. Figures 3.19 to 3.22 show the reconstruction results in both DTH and VBI methods, with and without the wind correction (cloud thickening), from the RCCM and the custom cloud masks. Table 3.3 shows the numerical results of the reconstructions.

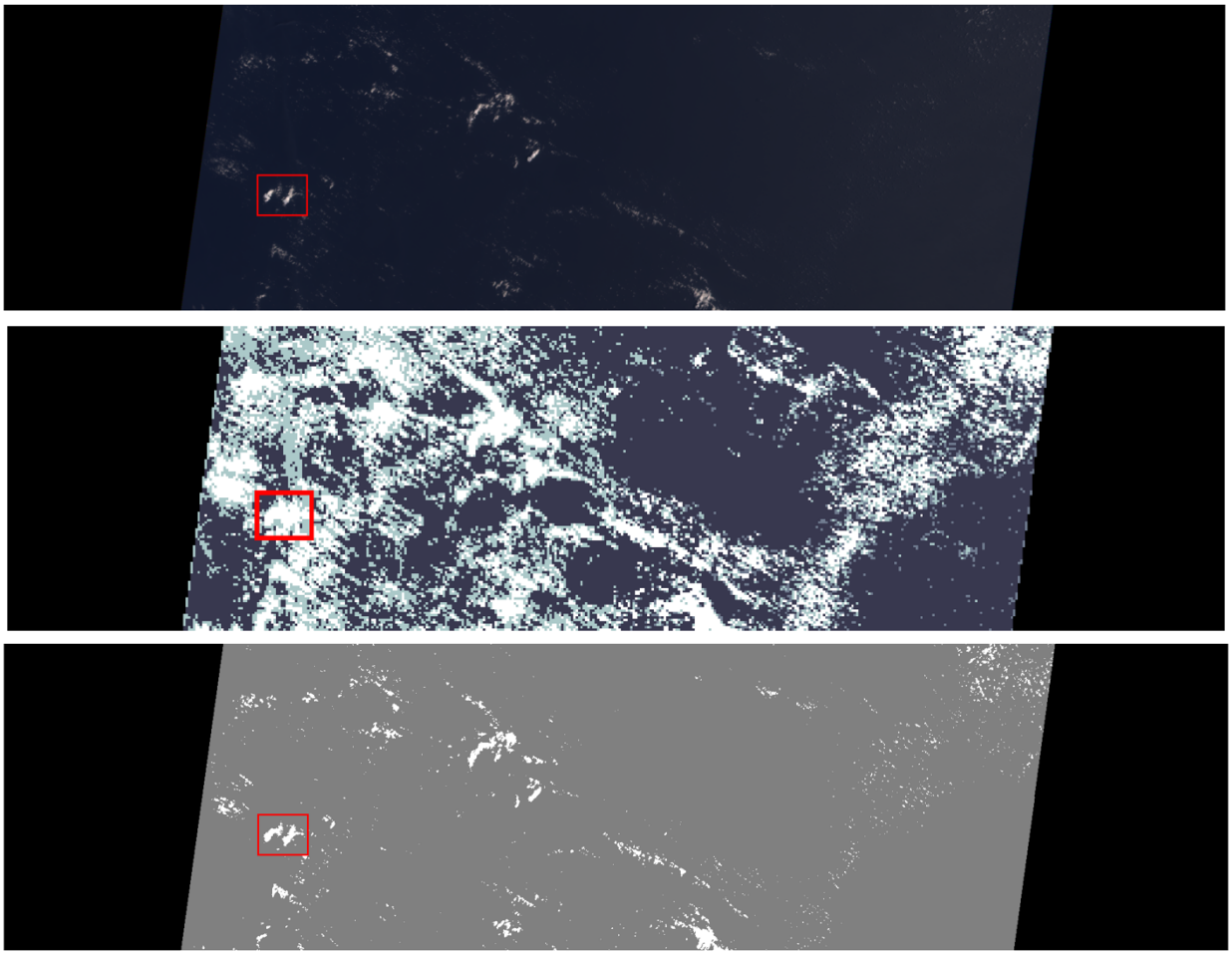

Figure 3.16. The RGB image, the RCCM, and the custom cloud mask of the entire block, for view angle AN. The region selected for the reconstruction is indicated in the red boxes.

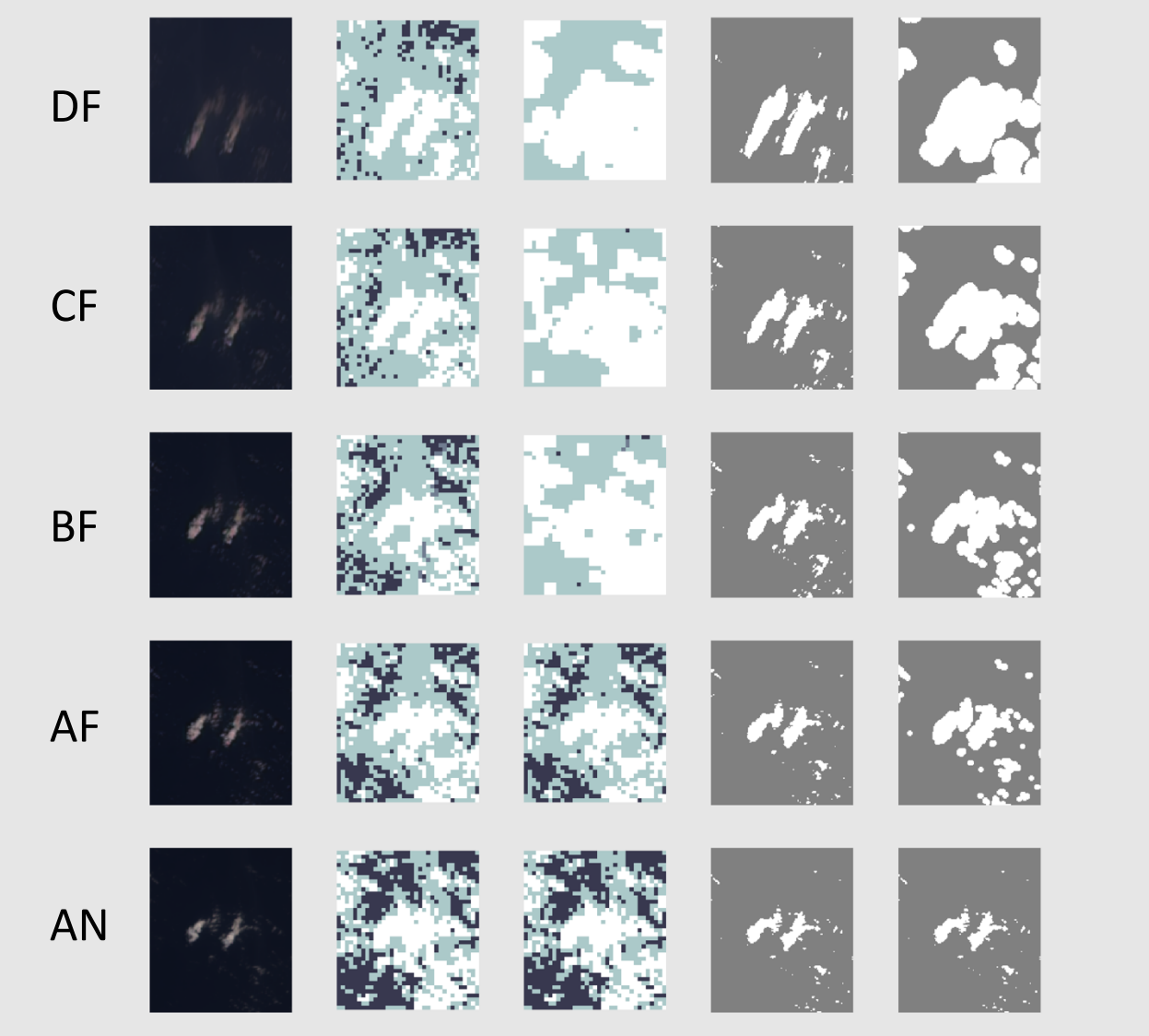

Figure 3.17. From left to right: the RGB image, the RCCM, the RCCM after the wind correction (cloud thickening), the custom cloud mask, and the custom cloud mask after the wind correction, of the selected region. From top to bottom: view angle DF, CF, BF, AF, and AN. For the custom cloud masks, $T_{RC} = 0.08$ and $T_{WD} = 0.16$ for all view angles.

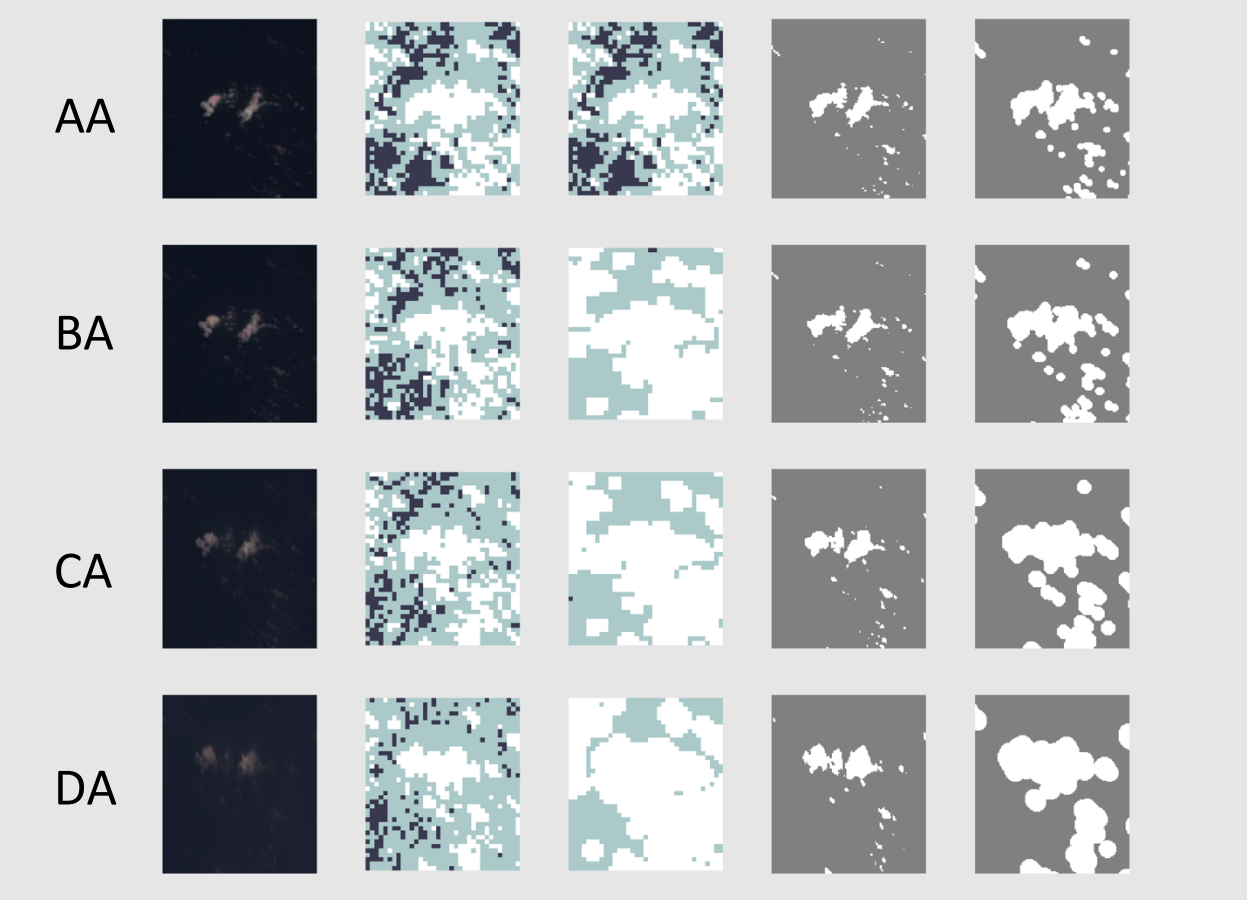

Figure 3.18. Same as Figure 3.17, but for view angles AA, BA, CA, and DA, from top to bottom.

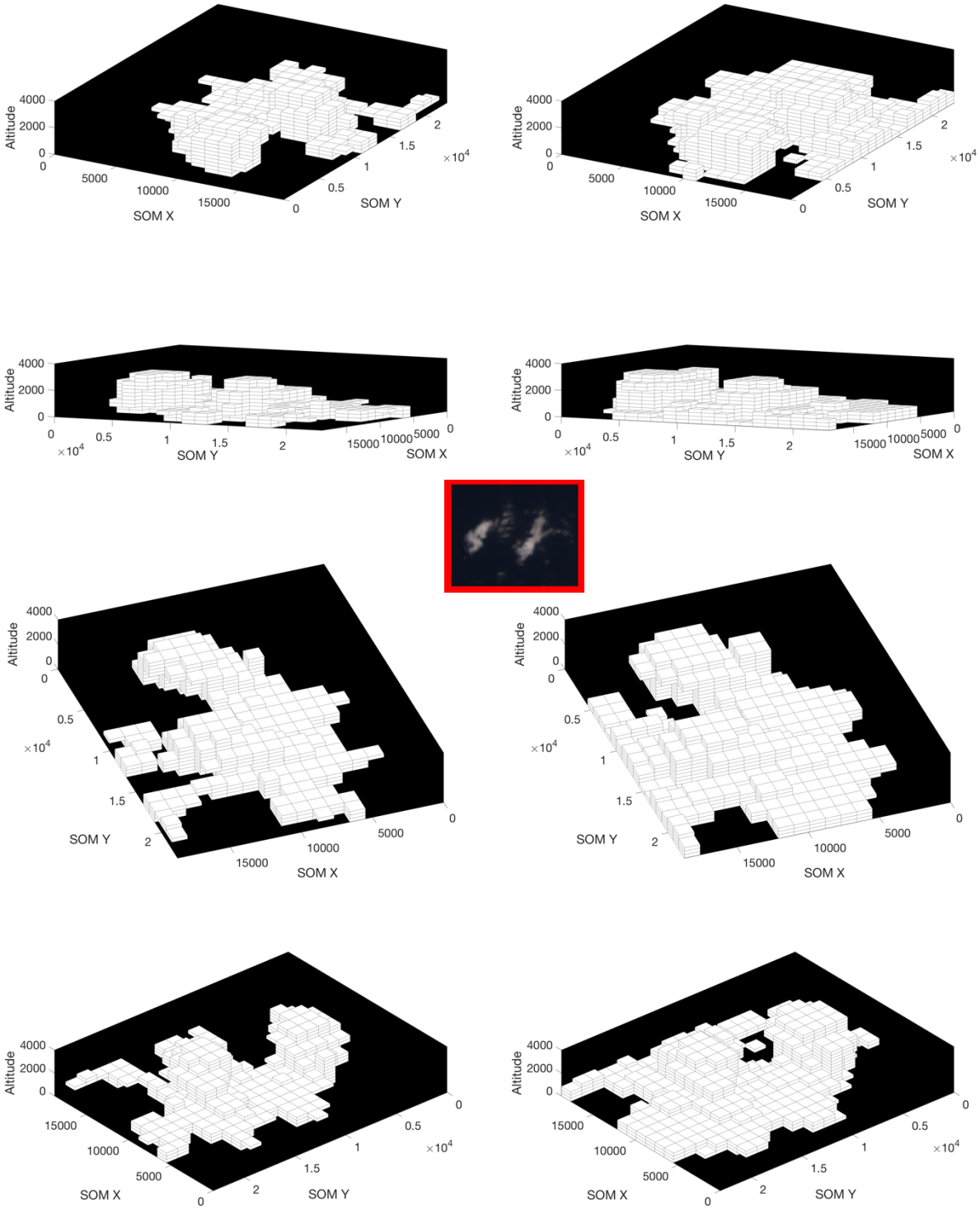

Figure 3.19. The reconstruction results from the RCCM inputs, with wind correction, under the DTH (left column) and the VBI (right column) ray casting methods, at various views (same view for each row). The units are all in m. The red box at the center is the overhead (nadir) RGB image of the reconstruction region.

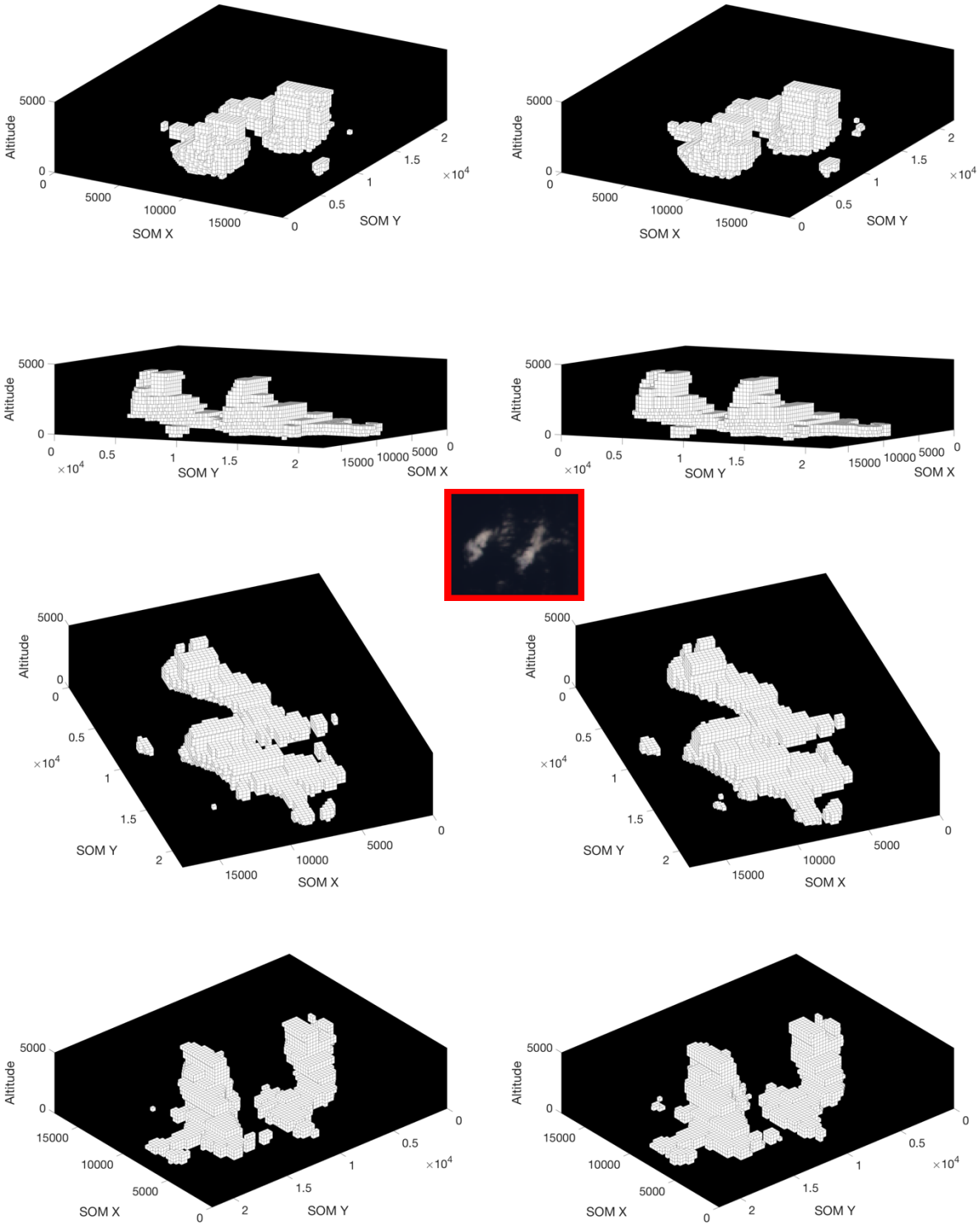

Figure 3.20. Same as Figure 3.19, but from the custom cloud mask inputs with wind correction.

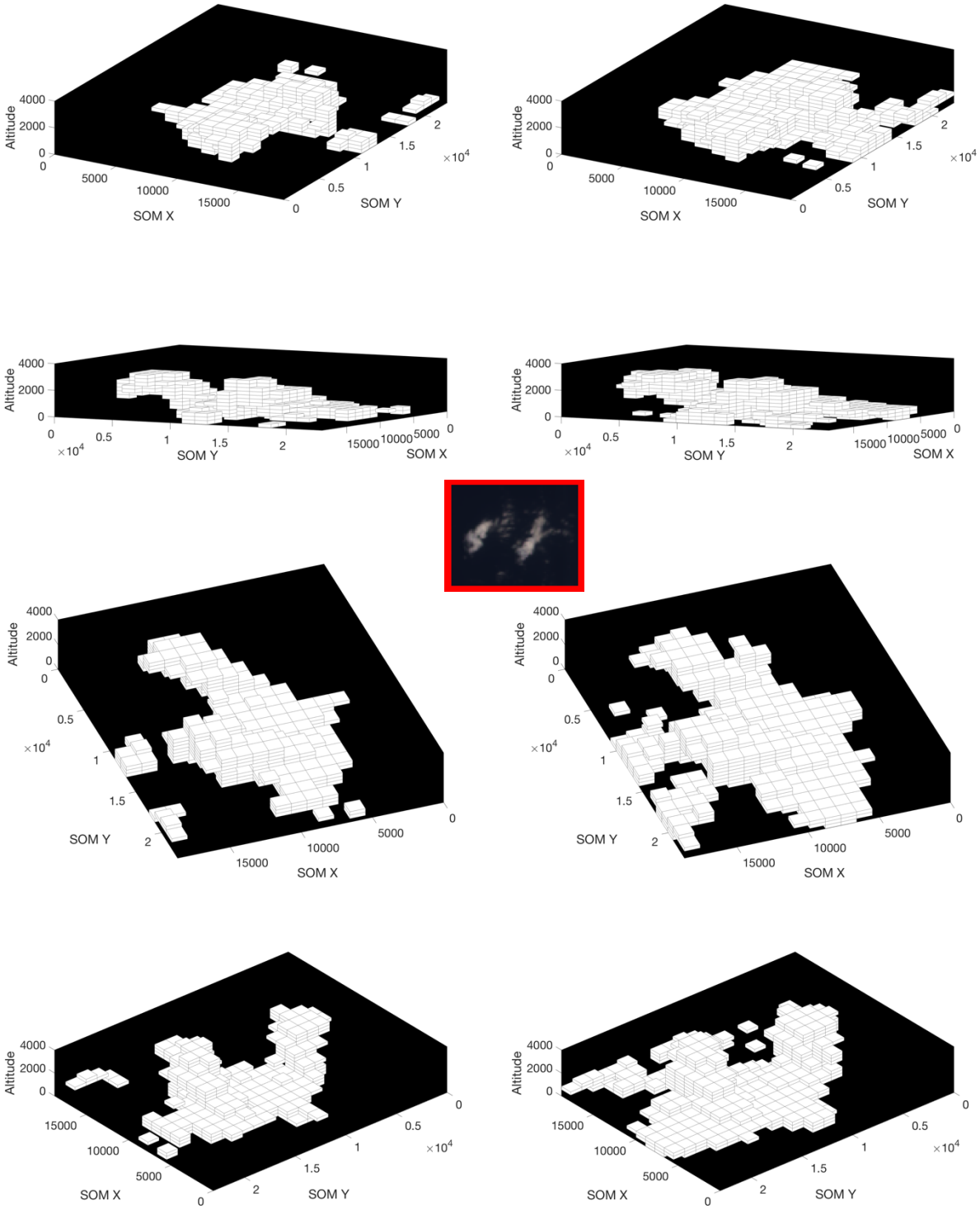

Figure 3.21. Same as Figure 3.19, but from the RCCM inputs without wind correction.

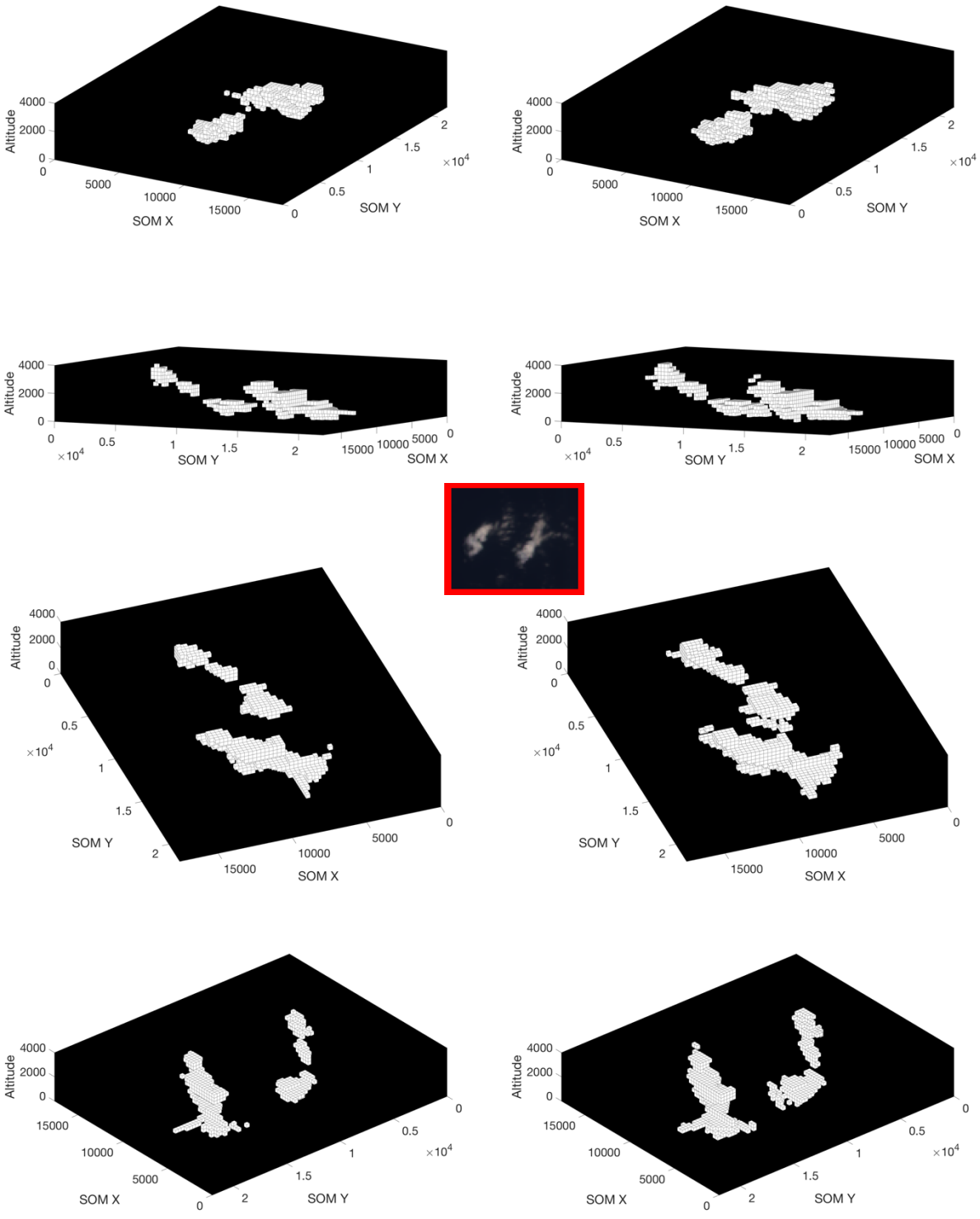

Figure 3.22. Same as Figure 3.19, but from the custom cloud mask inputs without wind correction.

Table 3.3. Comparison in reconstructed cloud volume between the eight different cases specified in Section 3.1. To simplify the volume calculations, each voxel is assumed to be a rectangular cuboid. The entries are in cubic meters.

Cloud Mask	**RCCM**		**Custom Cloud Mask**	
Ray Casting Method	**DTH**	**VBI**	**DTH**	**VBI**
Wind Correction	2.1662×10^{11}	3.3641×10^{11}	1.0213×10^{11}	1.1833×10^{11}
No Wind Correction	1.3809×10^{11}	2.1096×10^{11}	1.4849×10^{10}	2.1837×10^{10}

The same tendencies as in Table 3.1 and Table 3.2 are observed in Table 3.3. The VBI results tend to overestimate the cloud volume relative to the DTH results. The RCCM results tend to overestimate more than the custom cloud mask results. The results with wind correction (cloud thickening) tend to overestimate more than the results without wind correction.

Chapter 4. Discussion and Conclusion

4.1. Validation

The validation of the results remains a significant challenge. First, unlike the reconstruction simulations with synthetic data where the truth is already known, in the reconstructions from MISR's observation data the truth is unknown. The exact 3-D distribution of clouds in the selected locations and times in the real world are unknown. Although there are other sorts of observation data such as ground-based radar observations and other space-based satellite instruments data, the same problem persists, because those data contain their own uncertainties which lead to the lack of well agreed-upon truth for the cloud in their products, including their cloud masks. This is largely due to the fact that there is a lack of quantitative definition of what cloud is. As Di Girolamo & Davies once put, "the definition of cloud is based on instrument and algorithm performance", and this "contributes to a large variance in estimated cloud fraction by different instruments and algorithms" (Di Girolamo & Davies, 1997).

Besides, the current American Meteorological Society (AMS) glossary defines cloud as "a visible aggregate of minute water droplets and/or ice particles in the atmosphere above the earth's surface" (http://glossary.ametsoc.org/wiki/Cloud, accessed December 9, 2017). Notice how it says "visible", the word that is largely associated with the human eye. Hence, the most reliable method of validation for cloud may be the eyeball test through mental reconstructions.

This method poses several problems, however, such as that the human mental reconstruction is not quantitatively precise, and lacks the automated process of checking multiple scenes in a short amount of time.

Many of the studies mentioned in Chapter 1 employed simulating the atmospheric radiative transfer from LES cloud fields and retrieving synthetic radiance or radar data, with which they evaluated their reconstruction algorithms by comparing the reconstruction outputs and the original cloud fields. A similar validation method could have been employed in this project as well, if the correct simulation methods were developed for MISR radiance retrievals and the creations of the RCCM and relevant cloud mask products. Still, the approach used in Section 2.2 on the simplified clouds provide some understanding of what bias to expect in the reconstruction under the assumption of perfect cloud detection.

4.2. Implications of Current Results

Several possible implications of the reconstruction results are as follows. First, provided that they go through sufficient and proper validations and become refined with further adjustments, the results could be used to study the cloud distribution of a select geographical location for a climatological period of time, thanks to MISR's long-lasting operation of 17 years and likely more. Such studies could lead to understanding the role of cloud in the radiation budget of the local geography.

Second, the overall clear difference in the precision of the reconstructed volumes between the RCCM and the custom cloud masks suggest that there is a need to move towards a 275 m cloud mask for MISR.

Third, once the reconstruction program is extensively used to generate and accumulate results for many different real-world cloud scenes, the collection of such data could be used to test the realism of the geometry of clouds produced in LES simulated models and cloud resolving models.

Lastly, the results could be useful in providing the initial guess for future tomographic research involving MISR, such as the paper by Levis et al. (2015). The tomography is a newly emerging field in 3-D reconstruction of the microphysical properties of atmospheric constituents from observational data, and, when applied to cloud, could be useful in improving the understanding of the role of cloud in weather and climate.

4.3. Limitations

There are a few limitations that need to be noted with regard to the MISR cloud volume reconstruction results. First, due to the reconstruction method's nature of overestimating the cloud, especially those that horizontally stretch out, the application is limited to vertically well-developed cumulus cloud regions that have been manually selected. This means that the operationalization of the reconstruction program for all available MISR scenes is unlikely, unless

a technique such as a properly trained machine learning algorithm is developed for recognizing applicable scenes.

Next, within the methodology of this reconstruction, there have been made some assumptions that could introduce new errors and uncertainties, such as the those in the altitudinal axis (Section 2.4) and in cloud thickening for wind correction (Section 2.7), The MISR science products involved in the reconstructions also contain their own ranges of errors and uncertainties. All these could have contributed to results that are further from the reality of the actual cloud geometry.

4.4. Summary

The goal of this project was to reconstruct the cloud volumes from select MISR data. After simulations were performed with a handful of synthetic cloud volumes for the validation and the analysis of the expected outcomes of the reconstruction method, a series of algorithms including the ray casting were explored to achieve cloud volume reconstructions from cloud masks generated from MISR data, namely the RCCM and the custom cloud masks. Although the reconstruction program has been run on many different MISR scenes, three have been chosen to be presented in this thesis, namely Orbit 36649 Block 83, Orbit 19726 Block 86, and Orbit 01181 Block 91. The results were agreeable to the human eye, although further research with regard to proper, quantitative methods of validation are still in need.

4.5. Future Work

Possible future works include applying data other than MISR to improve the details of the reconstructed volumes. One is to make use of re-analyses data, as proposed in Section 2.1, to use the reported lifting condensation level as the cloud top height to reduce the overestimation at the bottom of the cloud. Another is to make use of an instrument that has a better resolution and is on board the same satellite platform as MISR, namely the Advanced Spaceborne Thermal Emission and Reflection Radiometer (ASTER). ASTER looks at the same scene as MISR at all times but at the instrument resolution of 15 m with two view angles. ASTER's high resolution data could be used to refine the reconstructed volumes and generate better results.

References

Alexandrov, M. D., B. Cairns, C. Emde, A. S. Ackerman, M. Ottaviani, and A. P. Wasilewski, 2016: Derivation of cumulus cloud dimensions and shape from the airborne measurements by the Research Scanning Polarimeter. *Remote Sensing of Environment*, **177**, 144-152.

Barker, H. W., M. P. Jerg, T. Wehr, S. Kato, D. P. Donovan, and R. J. Hogan, 2011: A 3D cloud-construction algorithm for the EarthCARE satellite mission. *Q. J. R. Meteorol. Soc.*, **137**, 1042-1058. doi:10.1002/qj.824

Boucher, O., D. Randall, P. Artaxo, C. Bretherton, G. Feingold, P. Forster, V.-M. Kerminen, Y. Kondo, H. Liao, U. Lohmann, P. Rasch, S.K. Satheesh, S. Sherwood, B. Stevens, and X.Y. Zhang, 2013: Clouds and Aerosols. In: *Climate Change 2013: The Physical Science Basis. Contribution of Working Group I to the Fifth Assessment Report of the Intergovernmental Panel on Climate Change* [Stocker, T.F., D. Qin, G.-K. Plattner, M. Tignor, S.K. Allen, J. Boschung, A. Nauels, Y. Xia, V. Bex and P.M. Midgley (eds.)]. Cambridge University Press, Cambridge, United Kingdom and New York, NY, USA.

Bull, M., J. Matthews, D. McDonald, A. Menzies, C. Moroney, K. Mueller, S. Paradise, and M. Smyth, 2011: Data Product Specifications – Incorporating the Science Data Processing Interface Control Document Revision S. Jet Propulsion Laboratory, California Institute of Technology. Retrieved July 10, 2017, from https://eosweb.larc.nasa.gov/project/misr/dps

Bull, M., J. Matthews, C. Moroney, and M. Smyth, 2005: Data Product Specifications – Incorporating the Science Data Processing Interface Control Document Revision N. Jet Propulsion Laboratory, California Institute of Technology. Retrieved July 1, 2017, from https://eosweb.larc.nasa.gov/project/misr/dps

Clothiaux, E. E., H. W. Barker, and A.V. Korolev, 2005: Observing Clouds and Their Optical Properties. In A. Marshak and A. Davis (Eds.), *3D Radiative Transfer in Cloudy Atmospheres* (pp. 93-150). Springer, Heidelberg, Germany.

Cornet, C., and R. Davies, 2008: Use of MISR measurements to study the radiative transfer of an isolated convective cloud: Implications for cloud optical thickness retrieval. *J. Geophys. Res.*, **113**, D04202. doi:10.1029/2007JD008921.

Davies, R., 1976: The three-dimensional transfer of solar radiation in clouds. *Ph.D. dissertation, Madison, Wis. : University of Wisconsin*. 220 pp.

Di Girolamo, L., and R. Davies, 1997: Cloud fraction errors caused by finite resolution measurements. *Journal of Geophysical Research,* **102**, D2, 1739-1756.

Diner, D. J., 1999: Experiment Overview. Jet Propulsion Laboratory, California Institute of Technology. Retrieved July 10, 2017, from https://eospso.gsfc.nasa.gov/atbd-category/45

Diner, D. J., J. C. Beckert, T. H. Reilly, C. J. Bruegge, J. E. Conel, R. A. Kahn, J. V. Martonchik, T. P. Ackerman, R. Davies, S. A. W. Gerstl, H. R. Gordon, J. Muller, R. B. Myneni, P. J. Sellers, B. Pinty, and M. M. Verstraete, 1998: Multi-angle Imaging SpectroRadiometer (MISR) Instrument Description and Experiment Overview. *IEEE Transactions on Geoscience and Remote Sensing*, Vol. 36, No. 4.

Diner, D. J., L. Di Girolamo, and E. E. Clothiaux, 1999: Level 1 Cloud Detection Algorithm Theoretical Basis. Jet Propulsion Laboratory, California Institute of Technology. Retrieved June 28, 2017, from https://eospso.gsfc.nasa.gov/atbd-category/45

Ellingson, R. G., and E. E. Takara, 2005: Longwave Radiative Transfer in Inhomogeneous Cloud Layers. In A. Marshak and A. Davis (Eds.), *3D Radiative Transfer in Cloudy Atmospheres* (pp. 487-519). Springer, Heidelberg, Germany.

Ewald, F., C. Winkler, and T. Zinner, 2015: Reconstruction of cloud geometry using a scanning cloud radar. *Atmos. Meas. Tech.*, **8**, 2491-2508, doi:10.5194/amt-8-2491-2015

Fielding, M. D., J. C. Chiu, R. J. Hogan, and G. Feingold, 2014: A novel ensemble method for retrieving properties of warm cloud in 3-D using ground-based scanning radar and zenith radiances. *J. Geophys. Res. Atmos.*, **119**, 10912–10930. doi:10.1002/2014JD021742.

Harshvardhan, 1982: The Effect of Brokenness on Cloud-Climate Sensitivity. *J. Atmos. Sci.*, **39**, 1853-1861.

Hartmann, D.L., A.M.G. Klein Tank, M. Rusticucci, L.V. Alexander, S. Brönnimann, Y. Charabi, F.J. Dentener, E.J. Dlugokencky, D.R. Easterling, A. Kaplan, B.J. Soden, P.W. Thorne, M. Wild, and P.M. Zhai, 2013: Observations: Atmosphere and Surface. In: *Climate Change 2013: The Physical Science Basis. Contribution of Working Group I to the Fifth Assessment Report of the Intergovernmental Panel on Climate Change* [Stocker, T.F., D. Qin, G.-K. Plattner, M. Tignor, S.K. Allen, J. Boschung, A. Nauels, Y. Xia, V. Bex and P.M. Midgley (eds.)]. Cambridge University Press, Cambridge, United Kingdom and New York, NY, USA.

Hinkelman, L. M., K. F. Evans, E. E. Clothiaux, T. P. Ackerman, and P. W. Stackhouse Jr., 2007: The effect of cumulus cloud field anisotropy on domain-averaged solar fluxes and atmospheric heating rates. *J. Atmos. Sci.*, **64**, 3499-3520.

Jovanovic, V. M., S. A. Lewicki, M. M. Smyth, J. Zong, and R. P. Korechoff, 1999: Level 1 Georectification and Registration Algorithm Theoretical Basis. Jet Propulsion Laboratory, California Institute of Technology. Retrieved June 14, 2017, from https://eospso.gsfc.nasa.gov/atbd-category/45

Jovanovic, V., K. Miller, B. Rheingans, and C. Moroney, 2012: MISR Science Data Product Guide. Jet Propulsion Laboratory, California Institute of Technology. Retrieved July 10, 2017, from https://eosweb.larc.nasa.gov/project/misr/dps

Kassianov, E., T. Ackerman, R. Marchand, and M. Ovtchinnikov, 2003: Satellite multiangle cumulus geometry retrieval: Case study. *J. Geophys. Res.*, **108,** D3, 4117. doi:10.1029/2002JD002350, 2003.

Levis, A., Y. Y. Schechner, A. Aides, and A. B. Davis, 2015: Airborne Three-Dimensional Cloud Tomography. *In Proc. IEEE ICCV*, 3379-3387.

Lewicki, S. A., and J. Zong, 1999: Level 1 Ancillary Geographic Product Algorithm Theoretical Basis. Jet Propulsion Laboratory, California Institute of Technology. Retrieved July 10, 2017, from https://eospso.gsfc.nasa.gov/atbd-category/45

Loeb, N. G., B. A. Wielicki, D. R. Doelling, G. L. Smith, D. F. Keyes, S. Kato, N. Manalo-Smith, and T. Wong, 2009: Toward Optimal Closure of the Earth's Top-of-Atmosphere Radiation Budget. *J. Climate,* **22**, 748-766.

Marshak, A., and A. Davis, 2005: 3D Radiative Transfer in Cloudy Atmospheres. Physics of Earth and Space Environments Series, Springer, Heidelberg, Germany.

Marshak, A., S. Platnick, T. Várnai, G. Wen, and R. F. Cahalan, 2006: Impact of 3D radiative effects on satellite retrievals of cloud droplet sizes. *J. Geophys. Res.* **111**, DO9207. doi:10.1029/2005JD006686.

Moroney, C., R. Davies, and J. Muller, 2002: Operational Retrieval of Cloud-Top Heights Using MISR Data. *IEEE Transactions on Geoscience and Remote Sensing,* Vol. 40, No. 7.

Mueller, K., C. Moroney, V. Jovanovic, M. J. Garay, J. Muller, L. Di Girolamo, and R. Davies, 2013: MISR Level 2 Cloud Product Algorithm Theoretical Basis. Jet Propulsion Laboratory, California Institute of Technology. Retrieved July 3, 2017, from https://eospso.gsfc.nasa.gov/atbd-category/45

Muller, J., A. Mandanayake, C. Moroney, R. Davies, D. J. Diner, and S. Paradise, 2002: MISR Stereoscopic Image Matchers: Techniques and Results. *IEEE Transactions on Geoscience and Remote Sensing,* Vol. 40, No. 7.

National Geospatial-Intelligence Agency (NGA), 2014: Department of Defense World Geodetic System 1984, Its Definition and Relationships with Local Geodetic Systems. Retrieved June 25, 2017 from http://earth-info.nga.mil/GandG/publications/index.html

Seiz, G., and R. Davies, 2006: Reconstruction of cloud geometry from multi-view satellite images. *Remote Sens. Environ.*, **100**, 143-149.

Snyder, J. P., 1987: Map Projections – A Working Manual. *United States Geological Survey Professional Paper 1395*, U. S. Government Printing Office, Washington, DC.

Welch, R. M., and B. A. Wielicki, 1989: Reflected Fluxes for Broken Clouds over a Lambertian Surface. *J. Atmos. Sci.,* **46**, 1384-1395.

Wielicki, B. A., and L. Parker, 1992: On the determination of cloud cover from satellite sensors: The effect of sensor resolution. *J. Geophys. Res.*, **97**, 12799-12823.

Wiscombe W. J., 2005: Scales, Tools and Reminiscences. In A. Marshak and A. Davis (Eds.), *3D Radiative Transfer in Cloudy Atmospheres* (pp. 3-92). Springer, Heidelberg, Germany.

Zhang, Z., A. S. Ackerman, G. Feingold, S. Platnick, R. Pincus, and H. Xue, 2012: Effects of cloud horizontal inhomogeneity and drizzle on remote sensing of cloud droplet effective radius: Case studies based on large-eddy simulations. *J. Geophys. Res.,* **117**, D19208. doi:10.1029/2012JD017655.

Zhao, G., and L. Di Girolamo, 2004: A Cloud Fraction versus View Angle Technique for Automatic In-Scene Evaluation of the MISR Cloud Mask. *Journal of Applied Meteorology*, **43**, 860-869.

Zhao, G., and L. Di Girolamo, 2006: Cloud fraction errors for trade wind cumuli from EOS-Terra instruments. *Geophys. Res. Lett.,* **33**, L20802, doi:10.1029/2006GL027088.

Zhao, G., and L. Di Girolamo, 2007: Statistics on the macrophysical properties of trade wind cumuli over the tropical western Atlantic. *J. Geophys. Res.*, **112**, D10204, doi:10.1029/2006JD007371

Zinner, T., B. Mayer, and M. Schröder, 2006: Determination of three-dimensional cloud structures from high-resolution radiance data. *J. Geophys. Res.,* **111**, D08204. doi:10.1029/2005JD006062.

Appendix A. Explanation for MATLAB Codes

This appendix explains the MATLAB codes used throughout this thesis project. All codes were written to run on MATLAB Version R2016b. For the actual codes, refer to Appendix B.

A.1. MISR Simulation Codes

This section explains the MATLAB codes used for MISR simulations described in Section 2.2.

- **MISRsimulation.m** is the ground script for all functions and commands performed for MISR simulations. It includes user-defined functions written to perform a variety of necessary calculations, and the command lines for plotting several figures shown in Section 2.2.
- **MISRsimulation_imgform.m** is the function code for the image formation in the MISR simulations.

  It takes as inputs a 3-D array of synthetic cloud, a three-entry array of initial cloud voxel size, a 1-D array of view angles, a scalar representing designated satellite height, a 3x(view angle array size) zero matrix representing the Cartesian coordinates of the focus point of each view angle camera, and a two-entry array of designated pixel size for the output synthetic satellite images.

  It returns a 3-D array of a set of synthetic cloud masks for every view angle, and a three-entry array representing the pixel numbers of the output cloud masks.

- **MISRsimulation_reconPlane.m** and **MISRsimulation_reconPlane2.m** are the function codes for the reconstruction of 3-D cloud volumes from the outputs of the image formation in the MISR simulations.

  Both take as inputs the synthetic cloud masks from image formation, the array of view angles and the scalar of satellite height, a scalar of designated maximum possible cloud top height, the array of camera focus, and a two-entry array of pixel size of the input cloud masks. In addition, MISRsimulation_reconPlane takes a three-entry array of designated voxel numbers (in SOM_X, SOM_Y, and the altitudinal axis) of the output cloud volume, while MISRsimulation_reconPlane2 takes a three-entry array of designated voxel size of the output cloud volume.

  Both return a 3-D array of output reconstructed cloud volume, and a 4-D array containing a reconstructed ray-track volume for each view angle. In addition, MISRsimulation_reconPlane returns a three-entry array of voxel size of the output cloud volume, calculated from the input voxel numbers, the input pixel size, and the pixel numbers of the input cloud masks.

- **MISRsimulation_compareOrgRecon.m** is the function code that calculates the volumetric difference between the original cloud and the reconstructed cloud. It takes as inputs the original synthetic cloud volume and the original voxel size, and the reconstructed cloud volume and its voxel size. It returns a scalar of the overestimation factor.

A.2. MISR RCCM Reconstruction Codes

This section explains the MATLAB codes used in the MISR cloud volume reconstruction from the RCCM for Orbit 36649 Block 83, discussed in Chapters 2 and 3.

- **MISR_Reconstruction_P100_O036649_RCCM.m** is the ground script for all functions and commands performed for MISR cloud volume reconstructions from RCCM images. It includes user-defined functions written to perform a variety of necessary calculations, and the command lines for plotting several figures shown in Chapter 3.
- **MISRreadRCCMcloud.m** is the function code for reading in the RCCM "Cloud" variables from the HDF files. It takes as input an array of characters containing the relevant HDF file address (for one view angle), and returns a 3-D array of 2-D RCCM for all blocks, and a 2-D array of an RCCM strip for the entire orbit.
- **MISRinterpolateVA.m** is the function code for interpolating the MISR viewing zenith and azimuth variables to match the dimensions of the RCCM variables.

  It takes as inputs a (180x8x32) array of viewing zenith from MISR Geometric Parameters, a (180x8x32) array of viewing azimuth, and a (2x180x128x512) array of GeoLatitude and GeoLongitude for each pixel for all blocks.

  It returns a binary (1x180) array indicating which block is valid for interpolation, a (2x180x6) array containing polynomial interpolation coefficients for "local_x" and "local_y" for all blocks, and two (180x128x512) arrays containing interpolated zenith and azimuth values. It also prints two different types of error analyses for the interpolation results for each block valid for interpolation.

- **MISRCloudThickening_forRCCM.m** is the function code for wind correction (cloud thickening) of the orbit's RCCM.

  It takes as inputs a (2x180x8x32) array of "wind" consisting of reported northward cloud motion and eastward cloud motion, a (9x180x128x512) array of RCCM Cloud, and a 3-D array of characters for every block's reference time for all nine view angles.

  It returns a 1-D array of block numbers reasonable for reconstruction (determined by the threshold value arbitrarily chosen within the code), a 1-D array of cloud boundary thickness addition number (explained in the code) with respect to the present block's AN time, and three (9x180x128x512) arrays with each representing the cloud-thickened RCCM with respect to either the previous, present or next block's AN time.

- **MISRreconEllip_forRCCMcrop_DTH.m** is the function code for reconstructing a cloud volume for a cropped local region within the selected RCCM block using the distance threshold (DTH) method.

  It takes as inputs a scalar for the selected block number, a scalar for the pixel division factor, a scalar for the altitudinal voxel length, a four-entry array of the indices for the cropped region within the block, a scalar for the confidence level, three (9x180x128x512) arrays of RCCM cloud-thickened with respect to the AN times of next, present, and previous blocks, a (2x180x128x512) array of GeoLatitudes and GeoLongitudes, a (2x9x180x128x512) array of the interpolated viewing zenith and azimuth, and a (180x128x512) array of cloud top height.

It returns a 3-D array of output cloud volume with cloud top height applied, the same-size array without the cloud top height applied, and a 4-D array of ray-track cloud volumes for all nine view angles.

- **MISRreconEllip_forRCCMcrop_VBI.m** is the function code for reconstructing a cloud volume for a cropped local region within the selected RCCM block using the voxel boundary intersections (VBI) method.

  It takes as inputs a scalar for the selected block number, a scalar for the pixel division factor, a scalar for the altitudinal voxel length, a four-entry array of the indices for the cropped region within the block, a scalar for the confidence level, three (9x180x128x512) arrays of RCCM cloud-thickened with respect to the next, present, and previous blocks, a (2x180x128x512) array of GeoLatitudes and GeoLongitudes, a (2x9x180x128x512) array of the interpolated viewing zenith and azimuth, and a (180x128x512) array of cloud top height.

  It returns a 3-D array of output cloud volume with cloud top height applied, the same-size array without the cloud top height applied, and a 4-D array of ray-track cloud volumes for every view angle.

- **MISRplotRCCM.m** is the function code for plotting an RCCM image. It takes as input a 2-D array with entries of RCCM Cloud confidence levels, and plots a figure showing the input RCCM image in a chosen set of colors.

A.3. MISR Custom Cloud Mask Reconstruction Codes

This section explains the MATLAB codes used in the MISR cloud volume reconstruction from the custom cloud masks for Orbit 36649 Block 83, discussed in Chapters 2 and 3.

- **MISR_Reconstruction_P100_O036649_CustomCloudMaskCrop.m** is the ground script for all functions and commands performed for MISR cloud volume reconstruction from the custom cloud masks for Orbit 36649 Block 83. It includes user-defined functions written to perform a variety of necessary calculations, and the command lines for plotting several figures shown in Chapter 3.
- **MISRinterpolateLatLong_forCCM_BlockPPN.m** is the function code for interpolating the MISR GeoLocation variables to match the dimensions of the custom cloud masks.

  It takes as inputs a scalar for the chosen block number, and a (2x180x128x512) array of GeoLatitude and GeoLongitude for each pixel for all blocks.

  It returns a (2x3x6) array containing the polynomial interpolation coefficients for the GeoLatitude and GeoLongitude for the chosen block, its previous, and its next, and a (2x3x512x2048) array containing the interpolated GeoLatitude and GeoLongitude values. It also prints the error analyses results for the interpolations.
- **MISRinterpolateRGBNIR_BlockPPN.m** is the function code for interpolating the MISR Non-AN green, blue, and Near IR variables to match the dimensions of the red radiance variables and custom cloud masks. The bilinear interpolation is used.

  It takes as inputs a scalar for the chosen block number, a 179-entry array of offsets for blocks at (128x512) pixel numbers, a (180x512x2048) array of red radiance, and three (180x128x512) arrays of green, blue, and Near IR radiance.

It returns four (3x512x2048) arrays of interpolated red, green, blue, and Near IR radiance for the chosen block, its previous, and its next.

- **MISRinterpolateVA_forCCM_BlockPPN.m** is the function code for interpolating the MISR viewing zenith and azimuth variables to match the dimensions of the custom cloud mask variables.

  It takes as inputs a scalar for the chosen block number, a (180x8x32) array of viewing zenith from MISR Geometric Parameters, a (180x8x32) array of viewing azimuth, a (2x180x128x512) array of GeoLatitude and GeoLongitude from MISR Ancillary Geographic Product, and a (2x3x512x2048) array of interpolated GeoLatitudes and GeoLongitudes for the previous, present, and the next blocks.

  It returns two (3x512x2048) arrays containing interpolated zenith and azimuth values. It also prints two different types of error analyses for the interpolation results for each of the three blocks.

  This function code is overall similar to the function code MISRinterpolateVA.m in Section A.2, except that it is interpolating the specific input block, its previous, and its next.

- **MISRcreateCCM.m** is the function code for creating the custom cloud masks (CCM) from the RGB images.

  It takes as inputs a scalar for the chosen block number, a 179-entry array of block offsets at (512x2048) pixel numbers, a (9x3x512x2048) array of red radiance for all view angles and for the previous, present (chosen), and next blocks, and three

(9x3x512x2048) arrays of interpolated blue, green, and Near IR radiance for all view angles and for the three blocks previously listed.

It returns a (9x3x512x2048) array of custom cloud masks, a (9x3x512x2048) array of cloud mask form Whiteness Deviation Threshold (WTH) Method, a (9x3x512x2048) array of cloud mask form Red Channel Threshold (RCT) Method, a nine-entry array of WTH values used, and a nine-entry array of RCT values used.

This function provides two modes of CCM creation. The first is the visual test, whereby the input threshold values are instantaneously applied and the consequent cloud masks are shown for the user to visually compare with the RGB images, until the inputs are adjusted to the right values. The second is the simple inputting of arrays, whereby arrays of threshold values can be manually entered to derive the final output cloud masks.

- **MISRcropInputImgAndCloudThickening.m** is the function code for cropping a local region for reconstruction and performing cloud thickening on the selected block's custom cloud masks.

  It takes as inputs a scalar for the chosen block number, a 179-entry array of block offsets at (512x2048) pixel numbers, a 3-D array of characters for every block's reference time for all nine view angles, a (2x3x512x2048) array of northward and eastward cloud motions for the previous, present, and next (PPN) blocks, a (2x9x3x512x2048) array of interpolated viewing zenith and azimuth for PPN blocks, four (9x3x512x2048) arrays of interpolated red, green, blue, and near IR radiance variables for PPN blocks, and a (9x3x512x2048) array of the custom cloud masks.

It returns a four-entry array of the cropped region's indices within the chosen block, a 4-D array of RGB radiance for the cropped region at all nine view angles, a 3-D array of the cropped custom cloud mask, a 3-D array of the cropped cloud-thickened custom cloud mask, the same-size arrays as the last three but of the ray casting domain of the cropped region, and a (9x3x512x2048) array of the cloud-thickened custom cloud masks.

This function offers two methods for cropping a local region. The first is the visual selection of a box over the AN custom cloud mask, and the second is the manual input of an array of cropped region's indices within the block.

- **MISRreconEllip_forCCMcrop_DTH.m** is the function code for reconstructing a cloud volume for a cropped local region within the selected block from the custom cloud masks using the distance threshold (DTH) method.

  It takes as inputs a scalar for the selected block number, a scalar for the pixel division factor, a scalar for the altitudinal voxel length, a four-entry array of the indices for the cropped region within the block, a 3-D array of cloud-thickened custom cloud masks of the ray casting domain for all view angles, a 179-entry array of block offsets at (512x2048) pixel numbers, a (2x9x3x512x2048) array of interpolated viewing zenith and azimuth for the chosen block, its previous, and its next, a (2x3x512x2048) array containing the interpolated GeoLatitude and GeoLongitude values for the three blocks, and a (180x512x2048) array of cloud top height for all blocks.

It returns a 3-D array of output cloud volume with cloud top height applied, the same-size array without the cloud top height applied, and a 4-D array of ray-track cloud volumes for all nine view angles.

- **MISRreconEllip_forCCMcrop_VBI.m** is the function code for reconstructing a cloud volume for a cropped local region within the selected block from the custom cloud masks using the voxel boundary intersections (VBI) method.

  It takes as inputs a scalar for the selected block number, a scalar for the pixel division factor, a scalar for the altitudinal voxel length, a four-entry array of the indices for the cropped region within the block, a scalar for the confidence level, a 3-D array of cloud-thickened custom cloud masks of the ray casting domain for all view angles, a 179-entry array of block offsets at (512x2048) pixel numbers, a (2x9x3x512x2048) array of interpolated viewing zenith and azimuth for the chosen block, its previous, and its next, a (2x3x512x2048) array containing the interpolated GeoLatitude and GeoLongitude values for the three blocks, and a (180x512x2048) array of cloud top height for all blocks.

  It returns a 3-D array of output cloud volume with cloud top height applied, the same-size array without the cloud top height applied, and a 4-D array of ray-track cloud volumes for all nine view angles.

- **MISRplotRGB.m** is the function code for plotting a MISR RGB image. It takes as inputs a scalar of the view angle number (1 to 9), a scalar of the chosen block number or index, and three same-size 4-D arrays of red, green, and blue radiance data for all nine view angles, and plots a figure showing the input RGB image.

A.4. Commonly Used Codes

This section explains the MATLAB codes commonly used in the MISR cloud volume reconstructions described in Chapters 2 and 3.

- **MISR_ MISRsimulation_viscloud.m** and **MISRvis3Dcloud.m** is the function code for plotting (visualizing) a 3-D cloud volume with its corresponding voxel size. It takes as inputs a 3-D array of cloud volume, a three-entry array of voxel size, and an array of characters of designated plot title. It returns a MATLAB figure with the 3-D plots of cloud volumes whose voxel sides are plotted with MATLAB built-in function “patch”.
- **MISRreconEllip_PrepareCastingRayVA.m** is the function code for creating variables for the ray starting points and the ray vectors during the reconstruction.

  It takes as inputs a scalar of WGS84 ellipsoid equatorial radius, a scalar of the polar radius, a two-entry array of the block image pixel numbers, two 3-D arrays of GeoLatitude and GeoLongitude values same for all nine view angles, and two 3-D arrays of viewing zenith and azimuth for all view angles.

  It returns three 3-D arrays of Cartesian x-, y-, and z-coordinates of the pixels same for all view angles, and three 3-D arrays of Cartesian x-, y-, and z-vectors of the viewing angles for the pixels at all view angles.
- **MISRreconEllip_DTH_RetrieveValidPts.m** is the function code for retrieving from the variables of the ray starting points and the ray vectors the valid pixels for reconstruction ray casting.

  It takes as inputs a 3-D array of the variable corresponding to the binary cloud masks for all nine view angles, three 3-D arrays of Cartesian x-, y-, and z-coordinates of

the pixels same for all view angles, and three 3-D arrays of Cartesian x-, y-, and z-vectors of the viewing angles for the pixels at all view angles.

It returns three nine-entry cell arrays each of whose entries contains 1-D array of Cartesian x-, y-, or z-coordinates of only the pixels valid for reconstruction ray casting, and three nine-entry cell arrays each of whose entries contains 1-D array of Cartesian x-, y-, or z-vectors of the viewing angles for only the pixels valid for reconstruction ray casting.

- **MISRreconEllip_DTH_RetrieveValidPts_forColumn.m** is the function code for retrieving from the variables of the ray starting points and the ray vectors the valid pixels for reconstruction ray casting. This function retrieves the valid pixels for the vertical column above the input SOM X and SOM Y indices in a loop.

  It takes as inputs a scalar for SOM X index, a scalar from SOM Y index, two scalars for the extension pixel numbers in SOM X and SOM Y from the cropped region to the ray casting domain, a 3-D array of the variable corresponding to the binary cloud masks for all nine view angles, three 3-D arrays of Cartesian x-, y-, and z-coordinates of the pixels same for all view angles, and three 3-D arrays of Cartesian x-, y-, and z-vectors of the viewing angles for the pixels at all view angles.

  It returns three nine-entry cell arrays each of whose entries contains 1-D array of Cartesian x-, y-, or z-coordinates of only the pixels valid for reconstruction ray casting around the input column, and three nine-entry cell arrays each of whose entries contains 1-D array of Cartesian x-, y-, or z-vectors of the viewing angles for only the pixels valid for reconstruction ray casting around the input column.

- **MISRreconEllip_FindBestFit.m** is the function code for calculating the coefficients for the best fit equation used in the polynomial interpolation of the input GeoLatitude or GeoLongitude variable.

  It takes as inputs a 2-D array of either GeoLatitude or GeoLongitude values, two 2-D arrays of SOM X and SOM Y grid values corresponding to the input GeoLocation variable, and a two-entry array of the block image pixel numbers.

  It returns a six-entry array of the constants for the best fit equation in the polynomial interpolation.

- **MISRreconEllip_ExtendCastingRayStartPts.m** is the function code for expanding the variables for the ray starting points to match the dimensions of the ray casting variables, and then for converting them to Cartesian coordinates.

  It takes as inputs a scalar of WGS84 ellipsoid equatorial radius, a scalar of the polar radius, a three-entry array of the reconstruction cloud volume's voxel numbers, a scalar of the number of rays in one dimension per pixel, a two-entry array of the block image pixel numbers, and two 2-D arrays of interpolated GeoLatitude and GeoLongitude values for the ray starting points.

  It returns three 2-D arrays of Cartesian coordinates of the extended ray starting points.

- **MISRreconEllip_ ExtendCastingRayVA.m** is the function code for expanding the variables for the ray vectors to match the dimenions of the ray casting variables.

It takes as inputs a two-entry array of the block image pixel numbers, a scalar of the pixel division factor, a scalar of the number of cast rays in one dimension per pixel, and three 3-D arrays of the viewing angle vectors in Cartesian coordinates.

It returns three 3-D arrays of the viewing angle vectors with extended dimensions.

- **MISRreconEllip_ ExtendValidRayCastingPositions.m** is the function code for expanding the variable for valid ray casting positions to match the dimensions of the ray casting variables.

  It takes as inputs a two-entry array of the block image pixel numbers, a three-entry array of the reconstructed cloud volume voxel numbers, a scalar of the pixel division factor, a scalar of the number of cast rays in one dimension per pixel, and a 3-D array of the variable corresponding to the binary cloud masks for all nine view angles.

  It returns a 3-D array of the variable corresponding to the binary cloud masks for all nine view angles, with extended dimensions.

- **MISRreconEllip_ FindIntersections_1234.m** is the function code for finding the intersection points between the voxel boundary planes and the cast rays. This function specifically concerns finding the intersections at view angles DF to DA. For functions concerning other view angles, see the comments in the code.

  It takes as inputs a three-entry array of reconstruction cloud volume voxel number, a 3-D array of the binary cloud masks with extended dimensions, three 2-D arrays of the Cartesian coordinates of the ray starting points with extended dimensions, three 3-D arrays of the ray vectors in Cartesian coordinates with extended dimensions,

and three 2-D arrays of coefficients for the equations of the voxel boundary planes perpendicular to SOM X and SOM Y axes and the altitudinal ellipsoids.

It returns three 2-D cell arrays for the designated four view angles each of whose entries contains a 1-D array of the x-, y-, or z-coordinates of the intersection points with voxel boundary planes perpendicular to SOM X axis, three 2-D cell arrays same as previously described but with voxel boundary planes perpendicular to SOM Y axis, and three 2-D cell arrays same as previous described but with altitudinal ellipsoids.

- **MISRreconEllip_ FindIntersections_CTH.m** is the function code for finding the intersection points between the voxel boundary planes and the cast rays at the view angle AN with the cloud top height applied.

  It takes as inputs a 2-D array of cloud top height, a scalar of the altitudinal voxel length, a two-entry array of input cloud top height's pixel number, a scalar of the pixel division factor, a scalar of the number of rays in one dimension per pixel, a three-entry array of reconstruction cloud volume's voxel number, a 3-D array of the binary cloud masks with extended dimensions, three 2-D arrays of the Cartesian coordinates of the ray starting points with extended dimensions, three 3-D arrays of the ray vectors in Cartesian coordinates with extended dimensions, and three 2-D arrays of coefficients for the equations of the voxel boundary planes perpendicular to SOM X and SOM Y axes and the altitudinal ellipsoids.

  It returns three 1-D cell arrays each of whose entries contains a 1-D array of the x-, y-, or z-coordinates of the intersection points with voxel boundary planes perpendicular to SOM X axis, three 1-D cell arrays same as previously described but with

voxel boundary planes perpendicular to SOM Y axis, and three 1-D cell arrays same as previous described but with altitudinal ellipsoids.

- **AssumptionVerification.m** is the script code for calculating the errors incurred due to some assumptions made in the project. It investigates two assumptions explained in Section 2.4. The first is the assumption of using the line extending from the origin to the pixel on the ellipsoidal surface and beyond as the altitudinal axis for the voxels above the pixel. The second is the difference between the ellipsoidal reconstruction and the plane-ground assumption.
- **MISRThesisImages.m** is the script code for displaying and saving a variety of images shown in Chapters 2 and 3. For details, see the comments in the code.

Appendix B. MATLAB Codes

This appendix provides access to the MATLAB codes explained in Appendix A.

- ByungsukLee_MS_ATMS_Thesis_MATLAB_CodeFiles.zip